Mechanical and Microstructural Changes in Heavy Ion Irradiated Metals

David Hewson Plantz

December 1990

UWFDM-1260

Ph.D. thesis.

Mechanical and Microstructural Changes in Heavy Ion Irradiated Metals

David Hewson Plantz

Fusion Technology Institute
University of Wisconsin
1500 Engineering Drive
Madison, WI 53706

http://fti.neep.wisc.edu

December 1990

UWFDM-1260

Ph.D. thesis.

MECHANICAL AND MICROSTRUCTURAL CHANGES IN HEAVY ION IRRADIATED METALS

BY

DAVID HEWSON PLANTZ

A thesis submitted in partial fullfillment
of the requirement for the degree of

DOCTOR OF PHILOSOPHY

(Materials Science)

at the

UNIVERSITY OF WISCONSIN-MADISON

1990

TABLE OF CONTENTS

LIST OF FIGURES

LIST OF TABLES

CHAPTER I

INTRODUCTION

The interaction of neutrons produced in proposed fusion reactors with structural materials (radiation damage) has been called "the second most serious obstacle to the commercialization of fusion reactors."[1] Since the discovery of voids in irradiated reactor structural materials by Cawthorne and Fulton [2], a massive research effort has been maintained to study void swelling in irradiated materials. However, neutron irradiation can also affect various material properties (creep, ductility, strength, phase stability, etc.) independently of void formation and/or swelling.

Irradiation effects are studied using fast fission neutrons or high-energy electrons or ions. Currently no source of neutrons with fusion reactor energy (14 MeV) and intensity (~10^{-6} dpa/sec) exists. Fast fission neutrons provide the closest means of comparison to the fusion reactor environment. However, this simulation method has serious drawbacks. Induced radioactivity in irradiated materials is enhanced greatly by thermal neutrons present in these reactors. This results in the need for special handling (e.g. hot cells). The low damage rates in these reactors (~10^{-6} dpa/sec) means that extremely long irradiation times (months or years) are needed to reach significant damage levels.

Electrons and ions can produce damage rates up to 10^{-1} dpa/sec without causing any induced radioactivity. Electron irradiation suffers from surface effects (i.e. not true bulk experiments) and lack of cascade formation (only isolated point defects) as found in neutron irradiations. Ion irradiation can produce cascades similar to neutrons, but the damage region is limited to a few microns from the irradiated surface. Both surface and injected interstitial effects must be guarded against. Neutrons produce gases (He and H) via transmutations. These gases must be either pre- or co-implanted in ion irradiations, which means that an exact simulation fo neutron irradiation is not possible. However, with or without gases, ion irradiation is an excellent tool for the study of many of the irradiation effects associated with the fusion environment.

When this study began, copper and its alloys (particularly high-strength, high-conductivity alloys) had received renewed interest in their application in fusion reactors [3]. Copper alloys have been considered for a wide variety of uses (e.g. high magnetic field insert coils in both tandem mirror and tokamak reactors [4], unshielded magnet coils and first walls in high heat flux compact reactors [5-9] and as divertors and limiters in other fusion devices [10-12]) that result in exposures from a few dpa to hundreds of dpa over a temperature range of <100°C to >500°C.

The current emphasis is on using materials that meet the Nuclear Regulatory Committee's regulation 10CFR61 [13] Class C specifications for radioactive waste disposal [14]. The Class C limit for copper is about 2400 appm [14,15]. Even with its waste disposal problems, the combination of good strength, and high thermal and electrical conductivity for a number of copper alloys make them attractive candidates for use as divertors and limiters [12], and magnet coils [6].

Irradiation effects in copper have been studied for over 30 years. The vast majority of these studies have been done at low doses (≤1 dpa) and have been concerned with voids, solute transport and defect clusters [16]. This lack of high fluence data is particularly severe for copper alloys and there is a great need for irradiation effects data for doses up to 100 dpa over the temperature range 50-500°C [3]. Except for low temperature (<100°C) radiation hardening studies [16] there is little known about the effect of irradiation on the mechanical properties of copper alloys [3].

The objective of this study is to directly measure changes in the mechanical properties of heavy-ion irradiated metals (especially Cu-1.8% Ni-0.3% Be) and compare them to changes in microstructure. Until recently, the confined depth of damage (<1 to 3 μm deep) in ion irradiation has limited the usefulness of this type of study to determine bulk (as opposed to surface effects) mechanical property changes under irradiation. This work builds upon a previous study at the University of Wisconsin, in which mechanical property changes resulting from irradiation with 14 MeV Cu ions in two copper alloys (Amzirc and MZC) were assessed by comparing the irradiated microstructure to the microstructure of the alloys following an aging study in which both microhardness and yield strength had been determined [17]. However, this is a very indirect method of determining radiation induced changes, with no guarantee of the comparison being correct. The development in the last 10 years of the Nanoindenter, a Mechanical Properties Microprobe (MPM), now enables one to measure mechanical properties directly from submicron structures [18-20]. The MPM was used in this study to directly measure these mechanical property changes in two Ni-Cu alloys and two high-strength, high conductivity copper alloys. These changes were compared to observed microstructural changes.

The first part of this study is to demonstrate that the MPM measures the properties of the irradiated zone exclusively and that these measurements represent bulk properties. Heavy-ion irradiation of well annealed Ni-10% Cu and Ni-50% Cu at the University of Wisconsin produced samples in which dislocation loops exclusively were formed in the irradiated zone while the rest of the sample remained defect free.[21] These samples are used to "calibrate" the MPM by comparing predicted yield strength changes as a results of these loops to changes measured by the MPM. The main emphasis of this work is the study of the effect of 14 MeV Cu ion irradiation on the mechanical and microstructural properties of Cu-1.8% Ni-0.3% Be. This alloy (manufactured by Brush Wellman, Inc. and supplied by Inesco) has an unirradiated yield strength of >700 MPa and electrical conductivity of >50% IACS (International Annealed Copper Standard) [22]. Samples of Cu-Al20 (Cu-0.2% Al as Al_2O_3) were also irradiated. This alloy (manufactured by SCM Metal Products and supplied by Los Alamos National Lab) has an unirradiated yield strength >500 MPa and electrical conductivity ~80% IACS [23]. Fig. 1.1 shows a comparison of

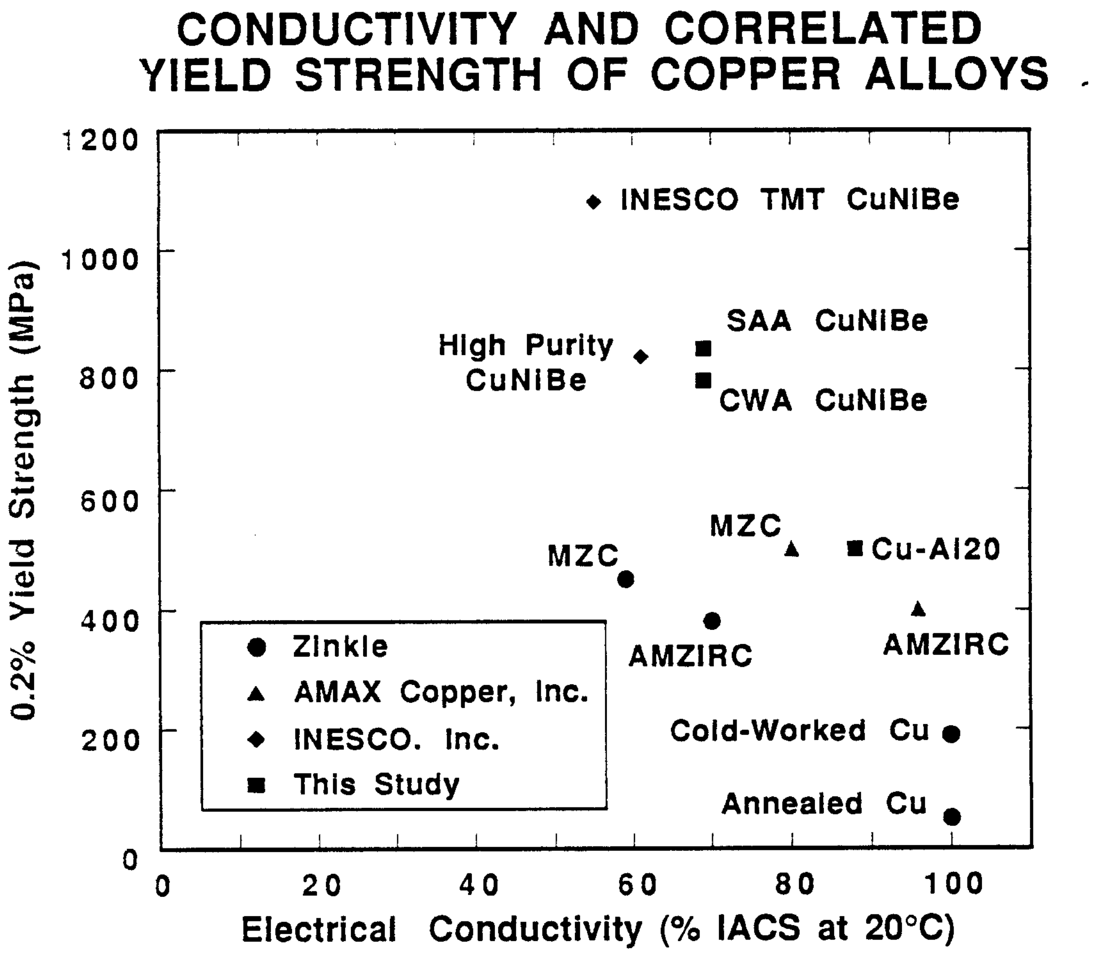

Fig. 1.1. Comparison of correlated conductivity and yield strength for several copper alloys with the alloys used in this study.

the unirradiated yield strengths and electrical conductivities of the two copper alloys used in this study, the two copper alloys used in a pervious study [17] and pure copper.

CHAPTER I

REFERENCES

1. G.L. Kulcinski, Contemp. Phys. 20 (1979) 417-447.
2. C. Cawthorne and E.J. Fulton, Nature 216 (1967) 575.
3. **Copper and Copper Alloys for Fusion Reactor Applications**, F.W. Wiffen and R.E. Gold (Eds.), DOE-OFE Workshop Proceedings (ORNL, CONF-830466) June 1984.
4. L.J. Perkins, J. Nucl. Mater. 122/123 (1984) 1371.
5. D. Cohn, unpublished, referenced in Ref. 17.
6. F.W. Wiffen, J. Nucl. Mater. 133/134 (1985) 32.
7. R.A. Krakowski, J. Nucl. Mater. 122/123 (1984) 37.
8. R.L. Hagenson et al., "Compact Reversed-Field Pinch Reactors:Preliminary Engineering Considerations," LA-10200-MS (Aug. 1984).
9. I.N. Sviatoslavsky, "Minimars Blanket Considerations," presented at ORNL Fusion Engineering Design Center (Jan. 1985).
10. "STARFIRE - A Commercial Tokamak Fusion Power Plant Study," (Sept. 1980) Argonne National Laboratory.
11. W.M. Stacey Jr. et al., Critical Issues, Vol. I, USA FED-INT0R/82-1 Phase 2A Report.
12. R.F. Mattas, Fusion Tech. 15 (1989) 637.
13. Code of Federal Regulation, 10CFR61, Federal Register, 47 (248) (1982) 57446.
14. R.W. Conn, et.al., Nucl. Tech./Fusion 5 (1984) 291.
15. F.M. Mann, Fusion Tech. 6 (1984) 273.

16. S.J. Zinkle and R.W. Knoll, "A Literature Review of Radiation Damage Data for Copper and Copper Alloys," UWFDM-578 (June 1984).

17. S.J. Zinkle, Ph.D. Thesis, Nuclear Engineering Dept., University of Wisconsin-Madison (1985).

18. J.B. Pethica, R. Hutchings and W.C. Oliver, Phil. Mag. A, 48 (1983) 593.

19. W.C. Oliver, R. Hutchings and J.B. Pethica, **Microindentation Techniques in Materials Science and Engineering,** ASTM STP 889, P.J. Alan and B.R. Lawn (Eds.), ASTM, Philadelphia (1985) 90.

20. M.F. Doerner and W.D. Nix, J Mater. Res., 1 (1986) 601.

21. L.-M Wang, Ph.D. Thesis, Materials Science Program, University of Wisconsin-Madison (1988).

22. S.N. Rosenwasser, in **Copper and Copper Alloys for Fusion Reactor Applications**, ORNL, CONF-830466 (1984) 309.

23. Technical Data Sheet, Bulletin No. 1404, SCM Metal Products (1980).

CHAPTER II

GENERAL RADIATION DAMAGE THEORY

II. A Point Defect Production

The irradiation of crystalline materials with neutrons, ions or electrons results in the displacements of atoms from their lattice sites, thus forming Frenkel defects (vacancy-interstitial pairs). The material properties of the solid can be substantially altered by the formation and conglomeration of these defects. The Frenkel pair density produced by incident particles of energy E is given by [1]:

$$N_d(E) = N_0 \int \phi(E)\ \sigma(E)\ K(E,T)\, \nu(T)\ dT \qquad (2.1)$$

N_0 is the atomic density of the irradiated crystal, $\phi(E)$ is the incident particle flux, $\sigma(E)$ is the collision cross-section between the incident particles and the matrix atoms, $K(E,T)$ is the probability that if an interaction takes place it will produce a displacement, i.e. a primary knock-on atom (PKA) with kinetic energy T, and $\nu(T)$ is the number of atoms displaced by the PKA.

Irradiations with different particles results in different damage effects. Electrons energetic enough to cause displacements (>0.5 MeV) produce only a few Frenkel pairs per nuclear collision, thus giving rise to isolated point defects. On the other hand, neutron and ion irradiations create PKA with enough energy to produce many more displacements in a small volume. This results in areas of high Frenkel pair densities called cascades. Ions have a much larger collision cross-section than neutrons, which results in a much greater density of cascades. This also causes the damage region for ions to be limited to within a few microns of the incident surface. As collisions slow down the ions the collision cross-section increases, producing a depth dependent damage rate. The displacement rate near the end of range is greater than at the surface by a factor of 5-10.

The time integral of Eq. (2.1) (normalized to the atomic density) gives a relative measure of the level of damage in an irradiated material. This damage level is known as dpa (displacements per atom). One dpa is equivalent to each atom in the material having been displaced, on the average, from its lattice site once during irradiation. Dpa calculations do not account for dose rate effects, Frenkel pair in-cascade recombination, spatial rearrangements due to defect migration, or the effects of transmutation products, such as helium. Nevertheless, dpa can be used to calculate first-order effects; thus, giving a means of comparing various irradiation environments.

The methods used to determine the dpa profile for an ion-irradiated material are briefly outlined here. More thorough reviews are given elsewhere [2,3]. The theoretical work of Lindhard and co-workers (LSS theory) [4,5] is used as the basis for determining the energy loss of an ion in a solid. Energy loss is divided into electronic and nuclear collisions, which are considered independent of one another. Experimental evidence indicates that LSS theory may overestimate electronic stopping for heavy-ion irradiation by 15-20%.[6-10] Alternative electronic stopping power theories [11,12] have been proposed but with only limited success.

Once the stopping powers have been calculated, the commonly accepted procedure for estimating the dpa level at a given depth x is to use the Kinchen-Pease model as modified by Torren and Robinson [13]:

$$N_d(x)\ \text{(dpa/sec)} = (\phi/N)\,\frac{K\,S_d(x)}{2\,E_d} \tag{2.2}$$

ϕ is the incident particle flux, N is the atomic density of the target, S_d is the energy available for displacements at x, K is the displacement efficiency and E_d is the spatial-averaged displacement threshold energy. The displacemnet efficiecy, K was originally thought to be independent of the incident particle energy [13], with a value of 0.8. An analysis by Kinney et al. [14] has shown that K varies strongly with energy, For 14 MeV Cu ions K = 0.3. For now K = 0.8 will be used in accordance with standard practice. The threshold energy, E_d varies by a factor of 2-3 with crystallographic direction and must be averaged. This energy is considered temperature independent for calculations, but in fact it decreases by about 70% from 4 K to 300 [15]. However, in accordance with convention a value of E_d = 29 eV will be used in all calculations [16].

Various computer codes have been developed to calculate the dpa profile and the injected ion distribution for ion irradiations [17-20]. Fig. 2.1 shows a plot of the dpa profile and ion distribution for a Brice code calculation in copper. The Brice code is particularly sophisticated in its consideration of energy transport by recoil atoms. The TAMIX Code was used to calculate the dpa profile and ion distribution in Fig. 2.2 for the two Ni–Cu alloys used in this study. TAMIX is a Monte Carlo code designed to simulate the ion transport process statistically and is in good agreement with the Brice code.

II. B Void Evolution Theory

Void swelling is not the focus of this investigation. However, knowledge of the processes involved in void swelling are useful in order to understand why it is not a concern to this study. Therefore, a brief review of void evolution theory is presented.

The high concentrations of the irradiation produced vacancies and interstitials ($C_{i,v}$ irrad. >> $C_{i,v}$ thermal) can migrate and agglomerate such that the macroscopic properties of a material are seriously degraded. Interstitials are mobile at very low temperatures (<50 K), but vacancies are not mobile until about 0.3 T_{mp} [21]. Interstitials and vacancies can be absorbed at sinks (dislocations, grain boundaries, etc.), recombine, or form interstitial or vacancy clusters. Interstitial loops are formed by the rapid aggregation of highly mobile interstitials and add to the overall dislocation density. Loops and dislocations have long range interactions with point

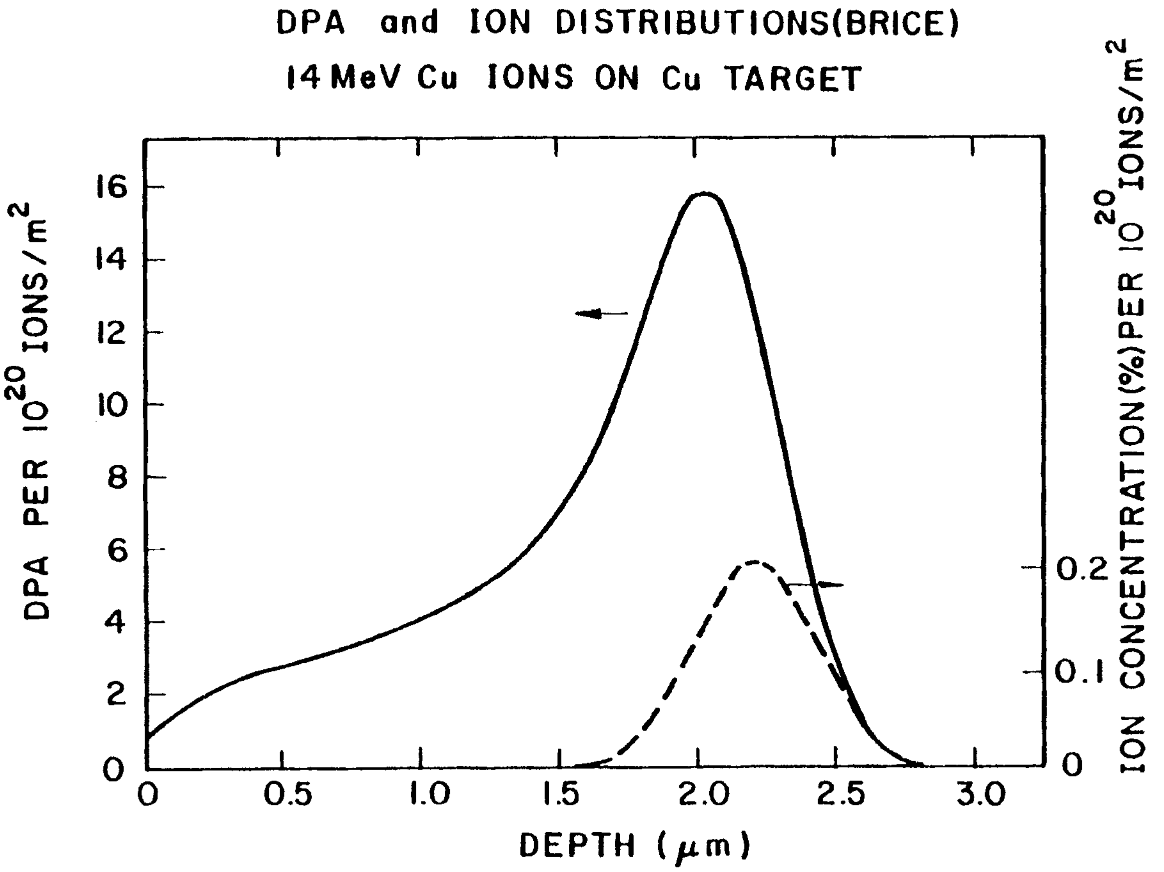

Fig. 2.2. Calculated 14-MeV Cu ion damage profile and injected ion distribution.

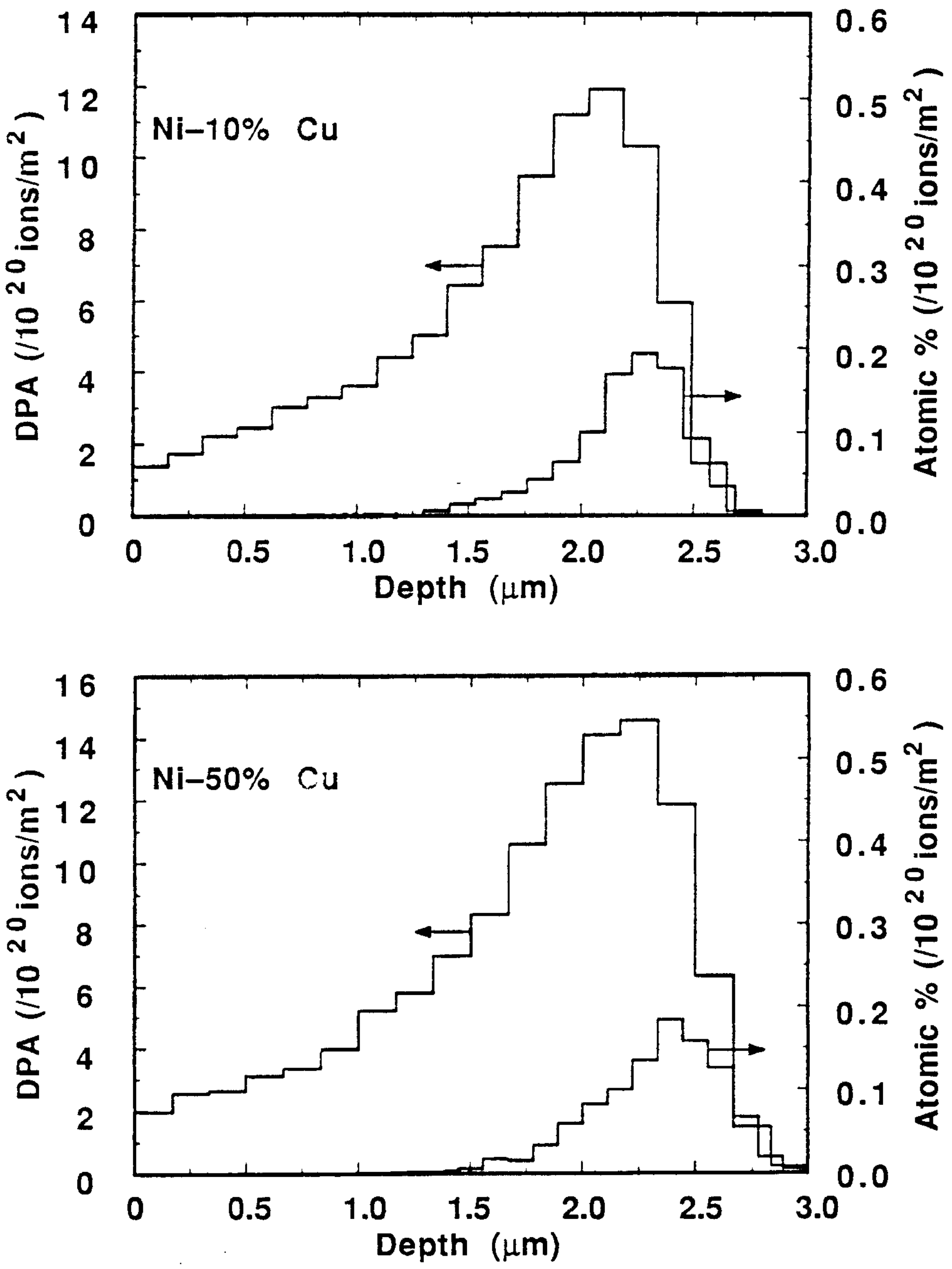

Fig. 2.2. Displacement Damage and implanted ion concentration versus depth for 14 MeV Ni ions in two Ni–Cu alloys using TAMIX Code (1000 histories).

defects, and differences in relaxation strains result in a greater dislocation bias for interstitials than vacancies [22-24]. This leads to a higher flux of vacancies to more neutral sinks and, of course, to sinks with bias for vacancies. This can result in cavity formation and growth (i. e. macroscopic swelling). However, swelling is limited to the temperature range of about 0.3 to 0.6 T_{mp}. Below 0.3 T_{mp}, low vacancy mobility leads to increased recombination and above 0.6 T_{mp} the already high thermal solubility of vacancies causes void embryos to become unstable and dissolve.

II. B. 1 Void Nucleation

Several void nucleation theories have been proposed in the literature [25-30]. Most of them assume that the void is the most stable vacancy cluster, which is not necessarily true [31,32]. A brief summary of the more accepted theories is presented here. More detailed reviews can be found elsewhere [27,33,34].

The first theories of void nucleation in the presence of a supersaturation of vacancies and interstitials were based on modifications of classical, homogeneous nucleation theory and known collectively as WKR theory (Wiedersich, Katz and Russell)[25,26]. Co-precipitation of vacancies and interstitials leads to void embryo growth by vacancy addition and shrinkage by interstitial addition. The nucleation rate is extremely sensitive to the relative arrival rates of vacancies and interstitials. Modifications of the WKR theory have included the effect of gas atoms [35,36] and the effect of immobile or highly mobile impurities [35] on nucleation. The theory offers no specific mechanism for termination of nucleation and for finding the terminal void density. The problems with the WKR model are that it offers no mechanism to determine nucleation termination, and it assumes a void surface energy of 1 J/m2 (nearly half the measured value [37]). Wolfer and co-workers [38-41] have shown that voids require a shell of impurity atoms that lower the surface energy in order for WKR to be valid.

Recently, time-dependent nucleation theories have been proposed by Wolfer and Wehner [31,40,42], and Kitajima et al. [30,43,44]. A Fokker-Planck equation is used to describe the dynamically evolving vacancy cluster distribution. The theory considers both subcritical embryos and growing voids at the same time. By considering the effects of the entire cluster distribution on its own further development, the theory provides a mechanism for nucleation termination and a means for determining void number densities. By using the most recent biases and a realistic surface energy their theory predicts void nucleation will occur without gas or a solute shell as long as the void is the most stable vacancy cluster. Wehner and Wolfer have obtained void number densities in close agreement with experiment [29], while WKR calculations are generally only accurate to within an order of magnitude of experiment.

II. B. 2 Void Growth

Void growth occurs once a vacancy cluster passes a critical size, r*, for constant irradiation conditions. Unlike void nucleation theory, void growth theory is relatively easy to quantify because of the ability to physically observe void growth. The most developed theories of void growth employ the formalism of chemical reaction rate theory [45-47]. Void growth theory has recently been reviewed by Mansur [48-50] and others [24,34,51]. The following is a brief resume of the theory.

To obtain the rate of void growth, the production rate and concentration of point defects and the strengths of the various defect sinks (voids, dislocations, etc.) must be known. Defect production and sinks are modeled as being uniformly distributed throughout the material. Sink strengths have been analyzed in detail by Brailsford et al.[52-54], while Mansur et al. [55] have shown that defect production can be modeled as uniformly distributed for void growth purposes. As a result the void growth rate is given by [49]:

$$\frac{dr_v}{dt} = \frac{\Omega}{r_v} \left(Z_v^v(r_v)\ D_v\ (C_v - C_v^e(r_v)) - Z_i^v(r_v)\ D_i\ C_i\right) \qquad (2.3)$$

r_v is the void radius, Ω is the atomic volume, $Z_{i,v}^{v}$ is the void capture efficiency of interstitials or vacancies, $D_{i,v}$ are the point defect diffusion coefficients, $C_{i,j}$ are the point defect concentrations and $C_v^e(r_v)$ is the thermal vacancy concentration at the void given by:

$$C_v^e(r_v) = C_v^e \exp\left(\left(\frac{2\gamma}{r_v} - p_g\right) \frac{\Omega}{kT}\right) \qquad (2.4)$$

C_v^e is the bulk thermal vacancy concentration, γ is the surface tension and p_g is the gas pressure in the void. The inclusion of mobile and immobile vacancy clusters (other than voids) modifies Eq. (2.3). The effects of divacancies and vacancy loops have been investigated by various authors with limited success [56-62].

Wolfer and co-workers [34,63,64] have shown that void swelling can be divided into 2 or 3 regimes. The first is a low swelling rate transient regime where nucleation and growth occur and the void sink strength approaches the dislocation sink strength (unless the dislocation sink strength remains high or there are a very large number of sinks, in which case voids are unable to nucleate). When these two sink strengths are equivalent, steady state swelling occurs. The steady state swelling rate depends on the net bias of the large voids. If the voids start to suppress the dislocation bias, swelling saturation can occur [34]. This is thought to happen in pure metals.

II. C Impurity Effects

II. C. I Gases

The nucleation and growth of voids is known to be affected by gases [49,65]. Neutron irradiation produces helium and hydrogen by transmutations, and these gases are often pre- or co-implanted in charged particle experiments. Many gases (O,N, etc.) are found in metals as residual impurities. Inert gases like helium may cluster in voids and exert a pressure in the void (see Eq. (2.4)). Reactive gases (H,O,N, etc.) can chemisorb on void surfaces and in turn lower the activation barrier for void nucleation. Extensive reviews of the effects of inert [34,49,65-68] and reactive gases [34,66] can be found in the literature. However, it is important to note that some swelling theories assume that voids are the most stable vacancy cluster and that gas is not a prerequisite for swelling. Zinkle et.al. [31,32] have shown that this is not true for many metals (stacking fault tetrahedra are the most stable cluster) and that small amounts of gas is required for voids to be stabilized (1 appm He or 1-10 appm O in Cu). Such low levels of gases are often found even in "gas free" metals.

II. C. 2 Alloying Elements

Experimental studies have shown that swelling is very sensitive to small changes in the solute content of a material [74]. Solute enrichment and depletion around voids have been observed in both steels [75-77] and copper alloys [78]. Reviews of the effects of alloying elements on void development have been done by a number of authors [35,50,69,77,79-82].

Void development is very sensitive to the diffusion coefficients of point defects, and solute segregation around a void can alter these coefficients locally [82]. Theoretical treatments of solute segregation on void nucleation have been done by Pillar and Marwick [83], and Wolfer and co-workers [44,45,84,85]. It was found that the void bias could be altered by a solute shell around the void if it slightly altered the material parameters at the void relative to the matrix, thus increaseing the nucleation rate by several orders of magnitude. A reduction of the void surface energy by solutes also enhances nucleation.

Solutes and precipitates can act to trap point defects, thereby increasing the recombination rate, and thus decreasing swelling. Harkness and Li [86] first considered the effect of solutes on point defect trapping and found that a low solute concentration (~0.1%) could drastically reduce swelling. More sophisticated models [87-89] have been developed that treat interstitial and vacancy trapping by solutes and precipitates. Precipitates are less effective traps per alloying atom than free solute atoms [79]. The binding of solutes to the point defect flux leads to solute segregation to sinks [53,77,80,89,90]. This acts to remove solutes from the matrix, thus reducing the number of traps. Radiation-induced segregation (RIS) has been found to be dose rate dependent [53,80], with the most segregation and the least swelling resistance occurring at low dose rates.

Precipitates can be expected to act as nucleation sites by reducing the void's surface energy; however, this has not been adequately treated in nucleation theories. Mansur [91] has evaluated precipitate-enhanced void growth by considering the void/precipitate pair as a larger effective sink than the void alone. This leads to enhanced growth of voids nucleated on or with precipitate relative to matrix voids.

II. D Considerations for Ion Irradiations

Ion irradiations can be conducted with damage rates far higher than neutron irradiations. Therefore, ion irradiations are often used to simulate neutron irradiations in order to gain information at a much accelerated rate. In order to extrapolate neutron damage information from high damage rate ion experiments, various factors (such as gas, damage rate and spatial effects) must be taken into account. Gas effects are easily accounted for by pre- or co-implantation of the gases needed. The other factors are considered below. Garner [87] has reviewed many of the factors that effect ion irradiations.

Swelling is very sensitive to point defect recombination and thermal vacancy emission. Higher displacement rates increase the amount of recombination and lower the ratio of thermally emitted to in-flowing vacancies. Thus, an irradiation at a high damage rate is equivalent to a low damage rate irradiation at a lower temperature. From an analysis by Bullough and Perrin [88] on damage rate effects, a temperature shift between ion and neutron irradiations was found to be:

$$T = (T_i)^2 \frac{k}{E_v} \left(1 + \frac{k T_i}{E_v} \ln\left(\frac{P_i}{P_n}\right)\right)^{-1} \ln\left(\frac{P_i}{P_n}\right) \qquad (2.5)$$

T_i is the ion irradiation temperature, k is Boltzmann's constant, E_v is the vacancy self-diffusion activation energy and P_i and P_n are the displacement rates for ion and neutron irradiations respectively. For an ion irradiation of copper at 10^{-3} dpa/sec and 400°C, Eq. (2.5) predicts it will correspond to a neutron irradiation at 10^{-6} dpa/sec and 280°C. Recombination is not completely treated in this analysis [53], thus it is not expected to be accurate at the low temperature end of the swelling regime.

The presence of the a free surface so close to the entire irradiated region can alter the response of a material compared to what might happen deep in the bulk of the material. Point defect concentrations are depressed near free surfaces relative to their bulk values. This results in a sink not encountered in bulk neutron damage studies. Several studies have shown that near the irradiated surface the swelling rate can be severely depressed and a void denuded zone of up to 1 μm deep can be expected[89-91].

The depth dependent damage rate leads to depth dependent point defect concentrations. Diffusion of the defects down the concentration gradient causes a broadening of the defect profile, and thus broadens the damage profile [49]. This decreases swelling in the damage peak and raises it in front of and behind the peak. Several experiments have seen evidence of diffusional spreading [6,92,93].

The irradiating ions come to rest as excess interstitials in the damage region (see Figs. 2.1 & 2.2). There have been several studies on the effect of injected interstitials on void nucleation [94,95] and growth [49,96]. They found that the injected interstitials suppressed swelling, and as recombination becomes more important (at lower temperatures), the effect is more pronounced. Experiments on the effect of the injected interstitials on void nucleation have confirmed the temperature dependence and the theory seems to be in qualitative agreement with experimental results [92].

To reduce these spatial effects a number of steps should be taken. Ion energies greater than 5 MeV should be used in order to avoid surface effects and to reduce the amount of the damage region effected by injected interstitials. Cross-section techniques should be used in order to assess the importance of these effects.

II. E Radiation Metallurgy

It was shown earlier (Sec. II. C. 2) that solute atoms and precipitates can have a profound effect on the swelling of a material under irradiation. The coupling between the irradiation produced point defect fluxes and solute atoms leads to fluxes of solute that can result in enrichment or depletion of alloying elements in various parts of the alloy relative to the original unirradiated composition, thus resulting in changes in the swelling behavior of a material [74,84,97]. Alloy phase stability has been found to be influenced by several general trends during irradiation:[98-100] radiation-enhanced diffusion (RED), radiation-induced segregation (RIS), radiation-enhanced precipitation (REP), radiation-induced precipitation (RIP), and radiation-modified precipitation (RMP). The optimum properties of many alloys result from specific microstructural preparations (e.g. precipitation hardened and/or cold-worked alloys and many steels), and the mechanisms mentioned above may change the microstructure, resulting in radical changes of an alloy's properties. It is these types of processes that are the main concern of this study.

II. E. 1 Radiation-Enhanced Diffusion

Substitutional solutes in alloys move via the interchange of their position with vacant lattice sites (vacancy diffusion), or via the interchange of interstitial and lattice positions (interstitial diffusion), the latter generally being unimportant in thermal diffusion. In general, the diffusion coefficient in a simple cubic metal is given by $D = \Gamma d^2/6$, where Γ is the atomic jump frequency and d is the jump distance. Under normal conditions (i.e. no irradiation) $\Gamma \sim C_v v_v$, where C_v is the vacancy concentration and v_v is the vacancy jump frequency; thus, the partial diffusion coefficient for vacancy diffusion is $D_v = \Gamma_v d^2/6$ and $D = D_v C_v$. Irradiation greatly increases the mobile defect concentration, which leads to RED via the increased concentrations of vacancies, interstitials, divacancies, etc.[101-103]. Thus, the diffusion coefficient under irradiation can be written as the sum of the various diffusion mechanisms, $D = \Sigma D_x C_x$ (x = interstitials, vacancies, divacancies, etc.)[103]. Binding and migration energies of divacancies and other higher order defects are not well known, and because their concentrations are small, only vacancies and interstitials are considered. Thus, diffusion is significantly increased during irradiation. RED could have serious consequences for alloys that depend on metastable microstructures (e. g. GP zones in precipitation hardened alloys or dislocations in cold-worked metals) by increasing the kinetics needed to reach the equilibrium.

RED has three limiting forms depending on temperature [101,103]. At high temperatures, the diffusion coefficient is basically unaltered by irradiation as a result of the thermal vacancy concentration being far greater than the irradiation produced defect concentration. At intermediate temperatures, where most defects are lost at sinks, the diffusion coefficient is temperature independent and varies linearly with the displacement rate, P (D_iC_i and $D_vC_v \propto P$). Point defect recombination of defects dominates at low temperatures and the diffusion coefficient varies as, $D \sim \sqrt{(\Gamma_v P)}$. Using this formalism, Zinkle estimated the shift in the recrystallization temperature of two cold-worked copper alloys and found good agreement with experiment (see Fig. 2.3)[104].

II. E. 2 Radiation-Induced Segregation

The flux of defects into and out of various regions of an alloy and the coupling of solutes to these fluxes results in RIS [105]. This possibility was first proposed by Anthony in 1972 [106]. Since then a great deal of theoretical work has been done in an attempt to model the mechanisms of RIS [75,107-121]. No complete model exists; however, three kinetic models have been developed that cover most of the cases. These three models, which are discussed briefly below, are [103]: (1) size factor, (2) mobile defects-solute complexes, and (3) inverse Kirkendall effect. Okamoto and Rehn [122] and Russell [103] have reviewed the theory and experimental evidence of RIS.

Self-interstitials in cubic metals are thought to exist in a "dumbbell" configuration with two atoms sharing a lattice point [75,107]. The strain energy of the dumbbell is lowered by replacing one of the solvent atoms with

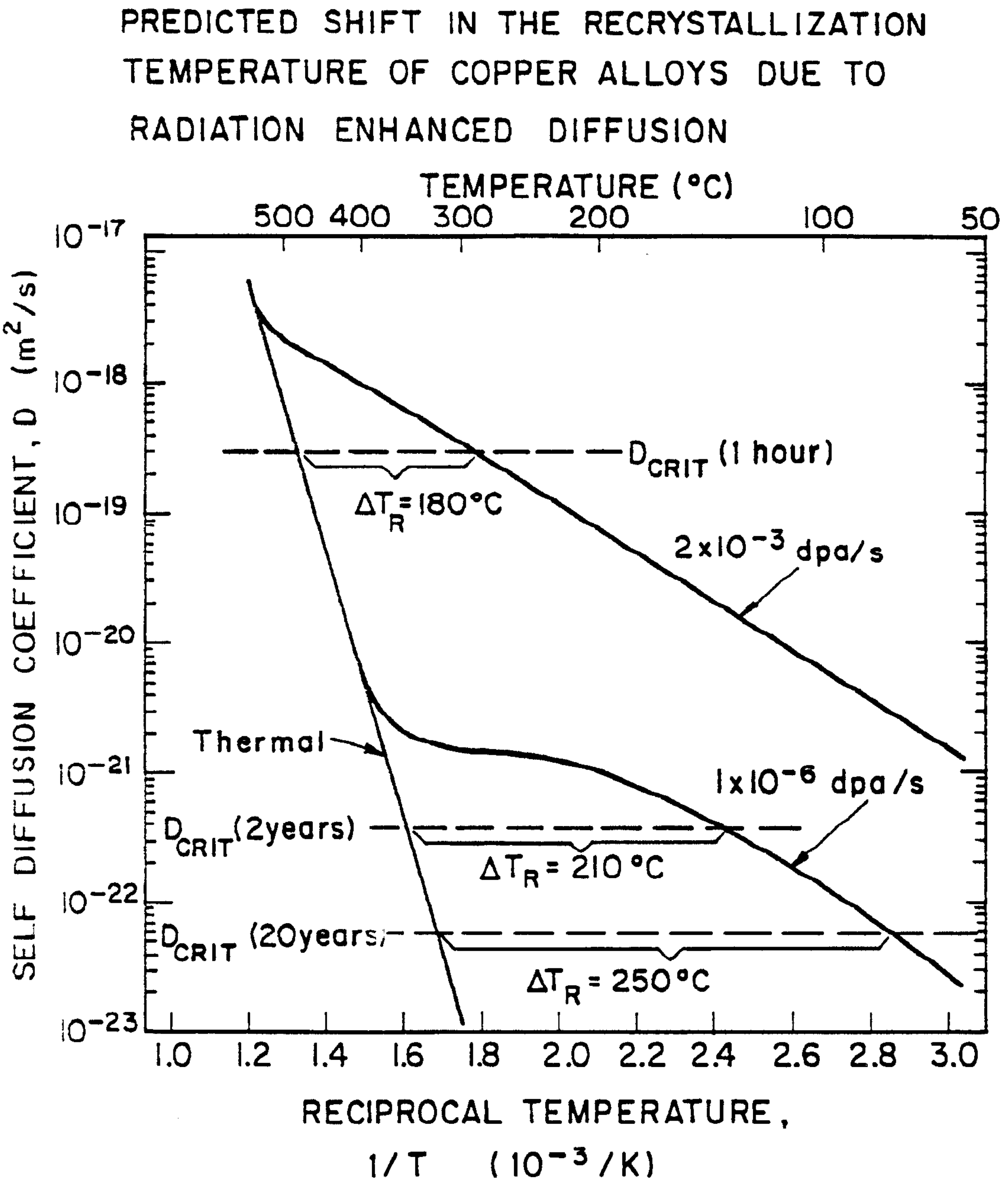

Fig. 2.3. Predicted shift in recrystallization temperature for irradiated cold-worked and aged Amzirc and MZC [104].

an undersized solute atom. The "mixed dumbbell" will preferentially migrate via the solute; thus, the solute will migrate with the irradiation-induced interstitial flux towards sinks. Oversized solutes in mixed dumbbells will tend to move into substitutional sites either by motion of the dumbbell via the solvent atom or the solute moving to a vacancy; thus, oversized solutes will migrate away from sinks.

The migration of bound defect-solute complexes was first proposed by Anthony [106]; however, Johnson and Lam [108,109] developed a more detailed atomistic model for dilute binary alloys that included both vacancy- and interstitial-solute binding. For undersized solutes the interstitial-solute mechanism was the dominant segregation process, while the size effect was found to be more important for oversized solutes (i.e. they migrate against the defect flux) unless very high vacancy-solute binding energies were used [110,111]. The Johnson-Lam model has been modified to include spatially varying displacement rates [111,112] (i. e. ion irradiations) and precipitation at sinks [111-113]. For ion irradiations, solute enrichment is predicted at the surface and beyond the damage peak, and solute depletion is predicted at the damage peak and subsurface region. The Johnson-Lam model and its modifications are in good qualitative agreement with experiment[122].

Manning [114,115], Marwick [116], and Wiedersich et al.[117,118] have postulated an inverse Kirkendall effect affecting RIS in concentrated alloys. In the Kirkendall effect, a vacancy flux results when a concentration gradient in an alloy with unequal diffusion coefficients occurs [123]. The net vacancy flux (and, hence, the relative diffusion of one element over the other) is proportional to the difference in the diffusion coefficients. For an alloy with different solute/solvent diffusion coefficients, the vacancy and interstitial fluxes caused by irradiation result in segregation of solute atoms via a Kirkendall-like mechanism called the inverse Kirkendall effect. Faster diffusing elements will flow up the vacancy gradient, resulting in an enrichment of slower diffusing elements at sinks. The solute gradient will then cause a Kirkendall flux of vacancies opposing the irradiation-induced flux, which may reduce void nucleation and growth. The solute concentration gradient was found to be proportional to the following [117,118]:

$$\nabla C_A \propto \left(\frac{D_A^v}{D_B^v} - \frac{D_A^i}{D_B^i}\right) \nabla C_v \tag{2.6}$$

where the D's are the partial diffusion coefficients of solute or solvent via interstitial and vacancy mechanisms. Thus element A will be enriched at the sink if $D_A^i/D_B^i > D_A^v/D_B^v$, i. e. A atoms migrate preferentially via interstitials and B atoms via vacancies. This model has also been extended to ternary alloys by Lam et al. [119, 120] and Marwick et al.[121].

The combination of mobile defect-solute complexes and the inverse Kirkendall effect was analyzed by Okamoto et al.[112]. The results of this analysis are generally valid for both dilute and concentrated binary alloys. They found a crossover temperature, below which segregation via defect-solute complexes dominates and above which the inverse Kirkendall effect dominates. The cross-over temperature for interstitial segregation was found to be near the melting point, while for vacancy segregation it is below 0.4 T_{mp}.

II. E. 3 Radiation Phase Stability

In addition to the mechanisms discussed in the previous sections (RED and RIS), three other general mechanisms affect phase stability. Wilkes has identified two of these mechanisms [98]: (1) radiation-enhanced precipitation (REP), where equilibrium transformations are reached more quickly during irradiation than thermally, and (2) radiation-induced precipitation (RIP), where transformations that occur during irradiation thermally revert back to their original structure. Radiation-modified precipitation (RMP) has been proposed by Lee et.al. [6], where irradiation causes changes in the composition of a phase relative to normal thermal equilibrium. These trends have been studied for over 10 years; however, there is no overall theory of phase stability during irradiation. Models have been developed to explain specific situations. Several reviews of the various models may be found in the literature [97,98,103,124,125]. The following is a short summary of the main models.

Irradiation can alter the phase boundaries of an alloy system. RIS can result in solute concentrations exceeding their solubility limits and cause precipitation. Thus, seemingly single-phase alloys can form a second phase if solubility limits exist. Lam and co-workers have considered this in their

RIS theories [111-113,117-120,122]. Russell [124] has claimed that irradiation cannot produce phases that do not appear on the phase diagram at a given temperature via segregation processes. RIS can only shift the phase diagram laterally. Martin [126] determined that RIS can only widen two-phase regions. Models of radiation-induced order-disorder processes have shown that the ordered phase disappears at lower temperature [127-129].

The effect of excess vacancies and interstitials on the formation and stability of incoherent precipitates has been investigated by Russell and co-workers [130-132]. For incoherent particles, point defects are annihilated at the particle-matrix interface. They found that vacancies greatly stabilize and enhance the nucleation of precipitates with a positive volumetric misfit. Oxide dispersoids were found to be very stable only when oxygen is an interstitial solute in the matrix [132]. Cascade destruction of nuclei was found to be minor [131]. Neither RIS or disorder resolution are considered by their model. Also this theory predicts RIP in undersaturated solutions of oversized solute atoms in contrast to experimental observations of RIP for only undersized solutes [133]. The model has been modified to include RIP by the undersized solutes [134] and cascade re-solution [135].

A model of the formation and stability of coherent precipitates has been developed by Cauvin and Martin [136,137] in a manner similar to Russell's [130]. Defects are only trapped at the particle-matrix interface. They found that the particle's critical size and its stability depends on the steady-state concentration of vacancies or interstitials trapped at the interface. However, irradiation is found to always increase precipitation, and the amount of precipitation is directly proportional to the displacement rate and the absolute magnitude of the atomic misfit of the solute.

The first model of precipitate stability was developed by Nelson, Hudson and Mazey (NHM model) and dealt with recoil re-solution [138]. It considered the effect of cascades on particle dissolution and RED on reprecipitation for a particle in an infinite medium. This model predicts that large particles will shrink and small ones will grow to an equilibrium size (inverse Ostwald ripening) as determined by the following rate equation:

$$\frac{dr}{dt} = -y\,P + \frac{3\,D\,C}{4\,\pi\,r\,c_p} - D\,r^2\,n \qquad (2.7)$$

where P is the displacement rate, D is the radiation-enhanced diffusion coefficient, C is the total solute concentration, c_p is the fraction of solute in the particle, n is the particle number density, and y is a semi-empirical constant which depends on whether sputtering or disorder dissolution is the dominant mechanism of recoil re-solution. The NHM model was modified for a finite recoil distance [139] to account for the effect of increased solute solubility for small particles [140]. Chou and Ghoniem [141] recently quantified the extent of recoil rsolution, and found that a cascade can completely destroy a particle on the order of 1 nm.

Wilkes [98] proposed a cellular model of recoil re-solution in which equal sized particles are uniformly distributed and where concentration gradients could be established. The inverse Ostwald ripening rate was found to be independent of the diffusion coefficient. This model was modified by Frost and Russell [142,143] to include a finite re-solution distance and transient effects. Steady-state matrix solute concentrations were found to be reached in about 100 seconds [103]. The matrix solute concentration was allowed to exceed the solubility limit, which resulted in the initial size distribution being transformed into a uniform dispersion of subsized particles. However, the process was estimated to take 30 years in a reactor (10 days for ion irradiations)[36].

Bilsby [144], Baron et al. [145,146] and Urban and Martin [147,148] have considered coarsening effects along with radiation resolution. Bilsby's model is valid only for small disordering rates. The model of Baron et al. is more sophisticated than Bilsby's, but it also only considered ordered phases. The average particle size was found to be inversely proportional to the disorder dissolution rate of the NHM model and was independent of the starting conditions. The model fails to include particle renucleation. The phase stability of Cauvin and Martin [136,137] for coherent precipitates was expanded to include coarsening by Urban and Martin. They did not include nucleation effects either. Coarsening for small particles (r<10 nm) is significantly enhanced during irradiation, while larger particles coarsen via RED only.

CHAPTER II

REFERENCES

1. G.L. Kulcinski, Contemp. Phys. 20 (1979) 417.
2. M.T. Robinson, **Radiation-Induced Voids in Metals**, J.W. Corbett and L.C. Ianniello (Eds), U.S. A.E.C. Technical Information Center, CONF-710601 (1972) 449.
3. G.L. Kulcinski, J.J. Laidler and D.G. Doran, Rad. Effects 7 (1971) 195.
4. J. Lindhard, M. Scharft and H.E. Schiott, Mat-Fys. Medd., Kgl. Dan. Vidensk. Selsk. 33 No. 14 (1963).
5. H.E. Schiott, Mat-Fys. Medd., Kgl. Dan. Vidensk. Selsk. 35 No. 9 (1966).
6. K. Farrell, N.H. Packan and J.T. Houston, Rad. Effects 62 (1982) 39.
7. O.S. Oen, J. Narayan and T.S. Naggle, **Applications of Ion Beams in Metals**, St. Picraux, E.P. Ear Nisse, and F.L. Vook (Eds.), (1974) 6339.
8. J.B. Roberto and J. Narayan, **Fundamental Aspects of Radiation Damage**, CONF-751006-PI (1975) 120.
9. J. Narayan, O.S. Oen and T.S. Naggle, J. Nucl. Mater. 71 (1977) 160.
10. J.B. Whitley, Ph.D. Thesis, Nuclear Engineering Department, University of Wisconsin-Madison (1978).
11. O.B. Firsov, Soviet Phys. JETP (Engl. Trans.) 36 (1959) 1076.
12. L.C. Northcliffe and R.F. Schilling, Nucl. Data (Sect. A) 7 (1970) 233.
13. I.M. Torrens and M.T. Robinson, in **Radiation Induced Voids in Metals** (1972) 739.
14. J.H. Kinney, M.W.Guinan, Z.A. Murir, J. Nucl. Mater. 122/123 (1984) 1028.

15. K. Urban and N. Yoshida, Phil. Mag. A. 44 (1981) 1193.

16. R.R. Coltman, Jr. et al., J. Nucl. Mater. 99 (1981) 284.

17 I. Manning and G.P. Mueller, Computer Physics Comm. 7 (1974) 85.

18. D.K. Brice, "Ion Implantation Range and Energy Deposition Codes COREL, RASE4 and DAM62," SAND-7500622, Sandia National Laboratories, Albuquerque, NM, (July 1977).

19. H. Attaya, Ph.D. Thesis, Nuclear Engineering Department, University of Wisconsin-Madison (1981).

20. S.Han,Ph.D. Thesis, Nuclear Engineering Department, University of Wisconsin-Madison (1988).

21. J.W. Corbett, Electron **Radiation Damage in Semiconductors and Metals**, Solid State Physics Supplement 7, Academic Press (1966).

22. R. Bullough and R.C. Perrin, in **Radiation Damage in Reactor Materials**, Vol. II IAEA, Vienna (1969) 233.

23. S.D. Harkness and Che-Yu Li, in **Radiation Damage in Reactor Materials**, Vol. II (1964) 189.

24. J. Gittus, **Irradiation Effects in Crystalline Solids**, Applied Science Publ. Ltd., Barking, Essex, England (1978).

25. J.L. Katz and H. Wiedersich, J. Chem. Phys. 55 (1971) 1414.

26. K.C. Russell, Acta Met. 19 (1971) 753.

27. R.M. Mayer et al., J. Nucl. Mater. 95 (1980) 44.

28. A.J.E. Foreman and B.N. Singh, Proc. of the Intern. Conf. on **Irradiation Behavior of Metallic Materials for Fast Reactor Core Components**, Corsica, France (1977) 113.

29. M.F. Wehner and W.G. Wolfer, Phil. Mag. A 52 (1985) 184.

30. K. Kitajima, N. Yoghrda, and E. Kuramota, J. Nucl. Mater. 103/109 (1981) 1355.

31. S.J. Zinkle, L.E. Seitzman and W.G. Wolfer, Phil. Mag. A 55 (1987) 111.

32. S.J. Zinkle, W.G. Wolfer, G.L. Kulcinski and L.E. Seitzman, Phil. Mag. A 55 (1987) 127.

33. K.C. Russell, Acta Met. 26 (1978) 1615.

34. W.G. Wolfer, J. Nucl. Mater. 122/123 (1984) 367.

35. K.C. Russell, Scripta Met. 7 (1973) 755.

36. J.L. Katz and H. Wiedersich, J. Nucl. Mater. 46 (1973) 41.

37. L.E. Murr, in **Interfacial Phenomena in Metals and Alloys**, Addision-Wesley Public. Company, Reading (1975) 124.

38. W.G. Wolfer and M.H.Yoo, ORNL/TM-5398 (May 1976).

39. W.G. Wolfer, L.K. Mansur and J.A. Sprugue, in **Radiation Effects in Breeder Reactor Structural Materials** (1977) 841. .

40. L.K. Mansur and W.G. Wolfer, J. Nucl. Mater. 69/70 (1978) 825.

41. W.G. Wolfer and L.K. Mansur, J.Nucl. Mater. 91 (1980) 265; also UWFDM-329.

42. M.F. Wehner, Ph.D. Thesis, Nuclear Engineering Department, University of Wisconsin-Madison (1885).

43. K. Kitajima, E. Kuramo and N. Yoshida, J. Nucl. Mater, 108/109 (1982) 267.

44. K. Kitajima, J. Nucl. Mater. 122/123 (1984) 608.

45. S.D. Harkness and Che-Yu Li, Met. Trans. 2 (1971) 1957.

46. H. Wiedersich in 2nd Intern. Conf. on the Strength of Metals and Alloys, Vol. 2 ASMA (1970); also Rad. Effects 12 (1972) 1 1 1.

47. A.D. Brailsford and R. Bullough, J. Nucl. Mater. 44 (1972) 121.

48. L.K. Mansur, Nucl. Tech. 40 (1978) 5.

49. L.K. Mansur and M.H. Yoo, J. Nucl. Mater. 85/86 (1979) 523.

50. L.K. Mansur and M.H. Yoo, Corsica Conf. Supplement (1979) 9.

51. M.H. Wood, R. Bullough and M.R. Hayns, in **Irradiation Behavior of Metallic Materials for Fast Reactor Core Components** (1973) 107.

52. A.D. Brailsford, R. Bullough and M.R. Hayns, J. Nucl. Mater. 60 (1976) 246.

53. A.D. Brailsford, J. Nucl. Mater. 60 (1976) 257.

54. A.D. Brailsford and R. Bullough, Phil. Trans. Roy Soc. Lon. A302 (1981) 87.

55. L.K. Mansur, W.A. Coghlan and A.D. Brailsford, J. Nucl. Mater. 85/86 (1979) 591.

56. M.H. Yoo, Phil. Mag. A 40 (1979) 193.

57. M.H. Yoo, Script. Met. 13 (1979) 635.

58. W.G. Wolfer and A. Si-Ahmed, Phil. Mag. A 46 (1982) 723.

59. R. Bullough, B.L. Eyre and K. Krishan, Proc. Roy. Soc. Lond. A 346 (1975) 81.

60. A.D. Brailsford, J. Nucl. Mater. 84 (1979) 269.

61. M.R. Hayns and M.H. Wood, Harwell Res. Rep. AERE-TP 832 (April 1982).

62. R. Bullough and T.M. Quisley, J. Nucl. Mater. 113 (1983) 179.

63. J.J. Sniegowski and W.G. Wolfer, "On the Physical Basis for the Selling Resistance at Ferritic Steels," UWFDM-535 (1983).

64. F.A. Garner and W.G. Wolfer, J. Nucl. Mater. 122/123 (1984).

65. K. Farrell, Rad. Effects, 53 (1980) 175.

66. A.J.E. Foreman and B.N. Singh, in **Dimensional Stability and Mechanical Behavior of Irradiated Metals and Alloys** (Brighton Conf.), British Nuclear Energy Society, London (1983) 95.

67. M.R. Hayns, Res. Mech. 6 (1983) 67.

68. L.K. Mansur and W.A. Coghlan, J. Nucl. Mater. 79 (1983) 1.

69. Proc. Intern. Conf. on Radiation **Effects in Breeder Structural Materials**, M.L. Bleiberg and J.W. Bennett (Eds.), Scottsdale, AZ, AIME (1977); also G.R. Gessel and A.F. Rowcliffe, 431.

70. R.R. Okamoto and H. Wiedersich, J. Nucl. Mater. 53 (1974) 336.

71. L. Laour et al., ASTM STP 782 (1982) 310.

72. W.G. Wolfer, F.A. Garner and L.E. Thomas, ASTM STP 782 (1982) 1023.

73. S.J. Zinkle and R.W. Knoll, "A Literature Review on Radiation Damage Data for Copper and Copper Alloys," UWFDM-578 (June 197~)

74. L.K. Mansur, M.R. Hayns and E.H. Lee, in **Phase Stability During Irradiation**, J.E. Holland, L.K. Mansur and D.T. Poster (Eds.), Pittsburgh (Oct. 1980) TMS-AIME, 359.

75. P.R. Okamoto, N.Q. Lam and H. Wiedersich, Proc. of the **Workshop on Correlation at Neutron and Charged Particle Damage**, J.O. Stiegler (Ed.), ORNL (June 1976) CONF-76O673, ~

76. A. Si-Ahmed, Ph.D. Thesis, Nuclear Engineering Department, University of Wisconsin-Madison (1981).

77. A.D. Brailsford, J. Nucl. Mater. 56 (1975) 7.

78. R.C. Pillar and A.D. Marwick, J. Nucl. Mater. 83 (1979) 92.

79. A. Si-Ahmed and W.G. Wolfer, ASTM-STP 782 (1982) 1008.

80. F.A. Garner and W.G. Wolfer, J. Nucl. Mater. 102 (1981) 143.

81. S.D. Harkness and Che-Yu Li, in **Radiation-Induced Voids in Metals** (1971) 798. .

82. L.K. Mansur and M.H. Yoo, J. Nucl. Mater. 74 (1978) 228.

83. A.O. Brailsford, J. Nucl. Mater. 78 (1978) 354.

84. L.K. Mansur, J. Nucl. Mater., 83 (1979) 109.

85. L.Q. Lam, P.R. Okamoto and H. Wiedersich, J. Nucl. Mater. 74 (1978) 101.

86. L.K. Mansur, Phil. Mag. A 44 (1981) 741.

87. F.A. Garner, J. Nucl. Mater. 117 (1983) 107.

88. R. Bullough and R.C. Perrin, in **Irradiation Effects on Structural Alloys in Nuclear Reactor Applications**, ASTM STP 484 (1970) 317.

89. M.H. Yoo and L.K. Mansur, J. Nucl. Mater. 62 (1976) 282.

90. R. Bullough and M.R. Hayns, Harwell Res. Rep., AERE-TP.699.

91. F.A. Garner and L.E. Thomas, in **Effects of Radiation on Substructure and Mechanical Properties of Metals and Alloys**, ASTM STP 529 (1973) 303.

92. B. Badger, Jr. et al., 12th Intern. Symp. on the **Effects of Radiation on Materials, Williamsburg**, VA, ASTM STP 870 (June 1985).

93. C.H. Henager, Jr., J.L. Brimhall and E.P. Simonen, Rad. Effects 76 (1978) 49.

94. D.L. Plumton and W.G. Wolfer, J. Nucl. Mater. 120 (1984) 245.

95. D.L. Plumton, H. Attaya and W.G. Wolfer, J. Nucl. Mater. 122/123 (1984) 650.

96. A.D. Brailsford and L.K. Mansur, J. Nucl. Mater. 71 (1977) 110.

97. P.R. Okamoto, N.Q. Lam and H. Wiedersich, Proc. of the **Workshop on Correlation of Neutron and Charged Particle Damage**, J.O. Stiegler (Ed.), ORNL (June 1976) CONF-760673, 111 .

98. P. Wilkes, J. Nucl. Mater. 83 (1979) 166.

99. A. Wolfenden, J.R. Holland, R.G. Lott and J.H. Spitznagel, in **Phase Stability During Irradiation** (1981) 383.

100. E.H. Lee, P.J. Maziasz and A.F. Rowcliffe, in **Phase Stability During Irradiation** (1981) 191.

101. G.J. Dienes and H.C. Damsk, J. Appl. Phys. 29 No. 12 (1958) 1713.

102. Y. Adda, M. Beyler and G. Brebec, Thin Solid Films 25 (1975) 107.

103. K.C. Russell, Progress in Materials Science 28 (1984) 229.

104. S.J. Zinkle, Ph. D. Thesis, Nuclear Engineering Department, University of Wisconsin-Madison (1985)

105. H. Wiedersich and P.R. Okamoto, in **Phase Stability During Irradiation** (1981) 23.

106. T.R. Anthony, in **Radiation Induced Voids in Metals**, J.W. Corbett and L.C. Ianniella (Eds.) U.S.A.E.C., Technical International Center, CONF-710601 (1972) 630.

107. H.G. Haubord and D. Martinson, J. Nucl. Mater. 69/70 (1978) 644.

108. R.A. Johnson and N.Q. Lam, Phys. Rev. B 13 (1976) 4364.

109. R.A. Johnson and N.Q. Lam, Phys. Rev. B. 15 (1977) 1794.

110. H. Wiedersich, P.R. Okamoto and N.Q. Lam, in Proc. Int. Conf. on **Radiation Effects in Breeder Reactor Structured Materials**, M.L. Bleiberg and J.W. Bennet (Eds.), Scottsdale AIME (1977) 801.

111. N.Q. Lam, P.R. Okamoto and R.A. Johnson, J. Nucl. Mater. 78 (1978) 908.

112. P.R. Okamoto, L.E. Rehn and R. S. Averback, J. Nucl. Mater. 108/109 (1982) 319.

113. N.Q. Lam, P.R. Okamoto, H. Wiedersich and A. Taylor, Met. Trans. A 9 (1978) 1707.

114. J.R. Manning, Bull. Am. Phys. Soc. 23 (1978) 287.

115. J.R. Manning in **Phase Stability During Irradiation** (1981) 3.

116. A.D. Marwick, J. Phys. F 8 (1978) 1849.

117. H. Wiedersich, P.R. Okamoto and N.Q. Lam, J. Nucl. Mater. 83 (1979) 98.

118. N.Q. Lam, H. Wiedersich and P.R. Okamoto, in Proc. of the Intern. Conf. on **Irradiation Behavior of Metallic Materials for Fast Breeder Core Components**, Corsica, France (1979) 51.

119. N.Q. Lam, A Kumar and H. Wiedersich, in **Effects of Radiation on Materials**, ASTM STP 782, H.R. Brager and J.S. Perrin (Eds.), Scottsdale (1982) 985.

120. N.Q. Lam, J. Nucl. Mater. 117 (1983) 106.

121. A.D. Marwick, R.C. Pillar and M.E. Horton, in **Irradiation Behavior of Metallic Materials for Fast Breeder Core Components** (1979).

122. P.R. Okamoto and L.E. Rehn, J. Nucl. Mater. 83 (1979) 2.

123. Z.D. Jastrzebski, **The Nature and Properties of Engineering Materials**, 2nd Ed., John Wiley and Sons, New York (1976) 134.

124. K.C. Russell, J. Nucl. Mater. 83 (1979) 176.

125. H.J. Frost and K.C. Russell, "Phase Stability Under Irradiation," in **Phase Transformation and Solute Redistribution in Alloys During Irradiation**, Res. Mechanical Monograph, F.V. Nolfi (Ed.), Applied Science Publ., England (1983).

126. G. Martin, Phil. Mag. A 38 (1978) 131.

127. K.Y. Liou and P. Wilkes, J. Nucl. Mater. 87 (1979) 317.

128. R.H. Zee and P. Wilkes, J. Nucl. Mater. 97 (1981) 171.

129. S. Banerjee and K. Urban, Phys. Stat. Sol. A 81 (1984) 145.

130. S.I. Maydet and K.C. Russell, J. Nucl. Mater. 64 (1977) 101.

131. M.R. Mruzik and K.C. Russell, J. Nucl. Mater. 78 (1978) 343.

132. M.S. Saiedfar and K.C. Russell, J. Nucl. Mater. 85/86 (1979) 936.

133. G. Martin, J.C. Aocquet, A. Barbu and Y. Adda, in **Radiation Effects in Breeder Reactor Structural Materials** (1977) 899.

134. R. Lauvin and G. Martin, J. Nucl. Mater. 83 (1979) 67.

135. G. Abromeit, in **Irradiation Behavior of Metallic Materials for Fast Reactor Core Components** (1979) 89.

136. R. Cauvin and G. Martin, Phys. Rev. B 23 (1981) 3322.

137. R. Cauvin and G. Martin, Phys. Rev. B 23 (1981) 3333.

138. R.S. Nelson, J.A. Hudson and D.J. Mazey, J. Nucl. Mater. 44 (1972) 318.

139. A.D. Brailsford, J. Nucl. Mater. 91 (1980) 221.

140. A J. Ardell and 0. Schwartz, unpublished, referenced in Ref. 124.

141. P. Chou and N.M. Ghoniem, J. Nucl. Mater. 117 (1983) 55.

142. H.J. Frost and K.C. Russell, Acta Met. 30 (1982) 953.

143. H.J. Frost and K.C. Russell, J. Nucl. Mater. 103/104 (1982) 1497.

144. C.F. Bilsby, J. Nucl. Mater. 55 (1975) 125.

145. M. Baron, H. Chang and M.L. Bleiberg, in **Radiation Effects in Breeder Structural Materials** AIME (1977) 395.

146. M. Baron, in **Phase Stability During Irradiation** (1981) 63.

147. K. Urban and G. Martin, Acta Met. 30 (1982) 1209.

148. K. Urban and G. Martin, "Precipitation Coarsening in Alloys Under Irradiation," in **Phase Transformations in Solids**, H.I. Aaronson (Ed.), AIME Warrenville, PA (1982).

CHAPTER III

LOW LOAD MICROINDENTATION HARDNESS

The irradiation facilities presently available ast fission reactors, accelerators, etc.) have a limited amount of space fc samples. Irradiated volume in ion and electron irradiations is further limited by the shallow depth of penetration of the particles (on the order of a few microns or less). This is not a major problem for microstructural studies (3 mm diameter by < 250 µm thick for TEM samples). However, the volume limitations present a major obstacle in the study of radiation effects on mechanical properties. The use and development of small specimen test techniques have been developed to overcome this obstacle. More details on small specimen test techniques for irradiated materials can be found in references 1 and 2.

One of the most useful techniques used in the study of mechanical property changes following irradiation is the microindentation hardness test. For the well established conventional microindentation hardness tests the sample volume is an order of magnitude smaller than for the recently developed miniature tensile test (~1.5 mm^3 vs. ~15 mm^3), and numerous indentations can be made in this volume versus only one tensile test [2]. For ion irradiated materials the irradiated volume is a thin surface layer (a few mircons thick) that often occupies only in a small part of the sample surface area. Tensile tests are completely impractical for this type of sample. In order to test such a small volume (< 0.1 mm^3) conventional microindentation hardness machines need to be pushed to and often beyond their limits. Spurred by the needs of present thin film and ion implantation technologies, ultra-low load microindentation hardness devices have been developed that are capable of extracting information from sub-micron structures [3-9]. The following is a brief review of indentation hardness with a particular emphasis on low load testing.

Indentation hardness is defined as an applied load divided by some applicable area (usually contact or projected area) over which the load is applied [10]. As defined, hardness is not a fundamental property of a material, but an arbitrarily defined value. As a result hardnesses are often given a dimensionless number. One of the most important aspects of indentation hardness numbers are their empirically determined relationship to various material properties, particularly yield strength [10].

For indenters giving geometrically similar indentations (e.g. pyramidal and conical indenters), Tabor [11] demonstrated that hardness (H) could be related to yield strength (Y) by $H = CY$ where C is referred to as the constraint factor. Empirically, C was determined to be about 3 for most metals [11-13]. This relationship has been modified to include strain hardening effects [12,15]. The physical origin of the constraint factor has been examined using both slip-line field theory and Hertzian analysis [10,16]. Both approaches yield a value for C of ~2.8 [10,16].

It was assumed that pyramidal and conical indenters produced hardness values independent of load and/or indentation depth because they produce geometrically similar indentations under all conditions. However, at loads below about 500 grams hardness values tend to deviate from the constant value at higher loads. In general, hardness tends to increase with decreasing load, but it has also been seen to decrease [10,17]. Many different factors influence hardness at low loads. These include specimen related factors such as surface finish, cold-working, precipitates, grain size,etc., and machine related factors such as load application, loading rate, vibrations, indenter defects, optics, etc. Mott [17] and Bückle [18,19] have extensively reviewed the various factors involved in this phenomena for conventional microindentation tests. Monte Carlo simulations of microindentation tests that consider the resolution of the load and area (ie. diagonal or depth) measurements have found the hardness tends to increase with decreasing load and deceasing resolution [20]. The increased resolution of both load and area measurements of the specially designed ultra-low load microindentation hardness machines have produced hardness results that are relatively constant to the lowest loads found in conventional machines (~1-10 g) [3-9,20-27].

At ultra-low loads (<1 g), hardness tends to increase with decreasing load [3-9,20-27]. This is particularly true for well annealed materials [3,4,20,21,24-26]. The observed rise is greater than that expected from resolution effects (<1 mg and <1 nm). For well annealed materials, the initial portion of the indentation is in a dislocation free volume and the theoretical ultimate lattice yield strength must be reached in order to nucleate dislocations and cause any plastic deformation [28]. This accounts for the large rise in hardness for indentations less than 20 nm deep, but it should have little effect on the value of the hardness once dislocations are nucleated. Various explanations have been developed to explain the apparently real hardness increase. These include, few dislocations in the small deformed zone [17,18], extreme local work hardening [20], attraction of dislocation to a free surface and their subsequent pinning by the indenter [24] and decreasing dislocation source size [25]. Using dislocation etch pitting techniques on indented silver shows that dislocation movement changes dramatically with load [21,26]. At very low loads no rosette pattern is seen [26]. At intermediate loads a rosette pattern appears [21,26], and at high loads (~1 g) a hemispheric pattern appears [21,26]. The appearance and change in the pattern is associated with an increase in dislocation mobility [21,26]. As dislocations are nucleated and as more slip planes become active, the dislocations become more mobile and there is a drop in hardness. It appears that the increase in hardness that is observed in even a high resolution ultra-low load microindentation hardness test is related to the nature of dislocations in volumes comparable to the interaction volume of the dislocations ($<1 \mu m^3$).

CHAPTER III

REFERENCES

1. **The Use of Small-Scale Specimens for Testing Irradiated Material**, ASTM STP 888, W.R. Corwin and G.E. Lucas (Eds.) (1986)
2. G.E. Lucas and G.R. Odette,Nucl. Eng. and Des./Fus. 2 (1985) 145.
3. N. Gane, Proc. Roy. Soc. Lond. A 317 (1970) 367.
4. J.B. Pethica, in **Ion Implantation into Metals**, V. Ashworth, W.A. Grant and R.P Procter (Eds.s) Pergamon, Oxford (1982) 147.
5. D Newey, H.M. Pollock and M.A. Wilkins, in **Ion Implantation into Metals**, V. Ashworth, W.A. Grant and R.P Procter (Eds.s) Pergamon, Oxford (1982) 157.
6. P.E. Wierenga and A.J.J. Franken, J. Appl. Phys. 55 (1984) 42244.
7. J.L. Loubet, J.M. Georges, O. Marchesini and G. Meille, J. Trib. 106 (1984) 43.
8. H Bangert, et.al., Thin Solid Films 187 (1986) 193.
9. S.-P. Hannula, J. Wanagel and C.-Y. Li, in **The Use of Small-Scale Specimens for Testing Irradiated Material**, ASTM STP 888, W.R. Corwin and G.E. Lucas (Eds.) (1986) 233
10. **Hardness Testing**, H.E. Boyer (Ed.) ASM (1987).
11. D. Tabor, **The Hardness of Metals**, Clarendon Press, Oxford (1951).
12. J.R. Cahoon, W.H. Broughton and A.R. Kutzak, Met. Trans 2 (1971) 1971.
13. J.J. Gilman, in **The Science of Hardness Testing and Its Research Applications**, J.H. Westbrook and H. Conrad (Eds.) ASM (1973) 51.
15. D. Tabor, J. Inst. Metals 79 (1951) 1.

16. M.C. Shaw, in **The Science of Hardness Testing and Its Research Applications**, J.H. Westbrook and H. Conrad (Eds.) ASM (1973) 1.

17. B.W. Mott, **Micro-indentation Hardness Testing**, Butterworths, London (1956).

18. H. Bückle, Met. Rev. 4 (1959) 49.

19. H. Bückle, in **The Science of Hardness Testing and Its Research Applications**, J.H. Westbrook and H. Conrad (Eds.) ASM (1973) 453.

20. N. Gane and J.M. Cox, Phil. Mag. 22 (1970) 881.

21. C.C. Chen and A.A. Hendrickson, in **The Science of Hardness Testing and Its Research Applications**, J.H. Westbrook and H. Conrad (Eds.) ASM (1973) 274.

22 H.M. Pollock, D. Maugis and M. Barquins, in **Microindentation Techniques in Materials Science and Engineering**, ASTM STP 889, P.J. Blau and B.R. Lawn (Eds.) (1985) 47.

23. R.M. Westrich, in **Microindentation Techniques in Materials Science and Engineering**, ASTM STP 889, P.J. Blau and B.R. Lawn (Eds.) (1985) 196.

24. J.B. Pethica, R. Hutchings and W.C. Oliver, Phil. Mag. A 48 (1983) 593.

25. W.C. Oliver, R. Hutchings and J.B. Pethica, **Microindentation Techniques in Materials Science and Engineering**, ASTM STP 889, P.J. Alan and B.R. Lawn (Eds.), ASTM, Philadelphia (1985) 90.

26. G.M. Pharr and W.C. Oliver, J Mater. Res. 4 (1989) 94.

27. M.F. Doerner and W.D. Nix, J Mater. Res. 1 (1986) 601.

28. J.B. Pethica and W.C. Oliver,in **MRS Symposium Proceedings**, Vol. 130, (1989) 13.

CHAPTER IV

REVIEW OF PREVIOUS EXPERIMENTS

IV. A Alloy Metallurgy

IV. A. 1 Ni-Cu Alloys

The Ni-Cu system is one of the simplest alloy systems known. Experimental studies indicate that there is complete miscibility in the solid state [1]. However, thermodynamic analyses of the system predict the existence of a misciblity gap below 325°C [2-5]. The Metals Handbook's phase diagram of the Ni-Cu system [6] (see Fig 4.1) includes a miscibility gap based on Elford's calculations [3]. The gap's maximum temperature is 322°C at Ni-20% Cu. Mass transport becomes too small below 347°C to experimentally verify these predictions.

IV. A. 2 Cu-Be-Ni Alloys

There have been very few studies of the metallurgy of Cu-Be-Ni alloys similar to the alloy being used in this thesis work (Cu-0.3% Be-1.5% Ni) [7-20]. This alloy (CDA No. C17510 or Brush Alloys 3) [7-9] is a variant of a Cu-Be-Cobalt alloy (CDA No. C17500 or Brush Alloy 10) [7-9] in which the cobalt has been replaced by nickel for economic reasons. The properties of C17510 are very similar to C17500 [7-11]. The most common use for this alloy is for high-current springs in switches and relays that often operate at elevated temperatures [20,21]. It is presently being considered for

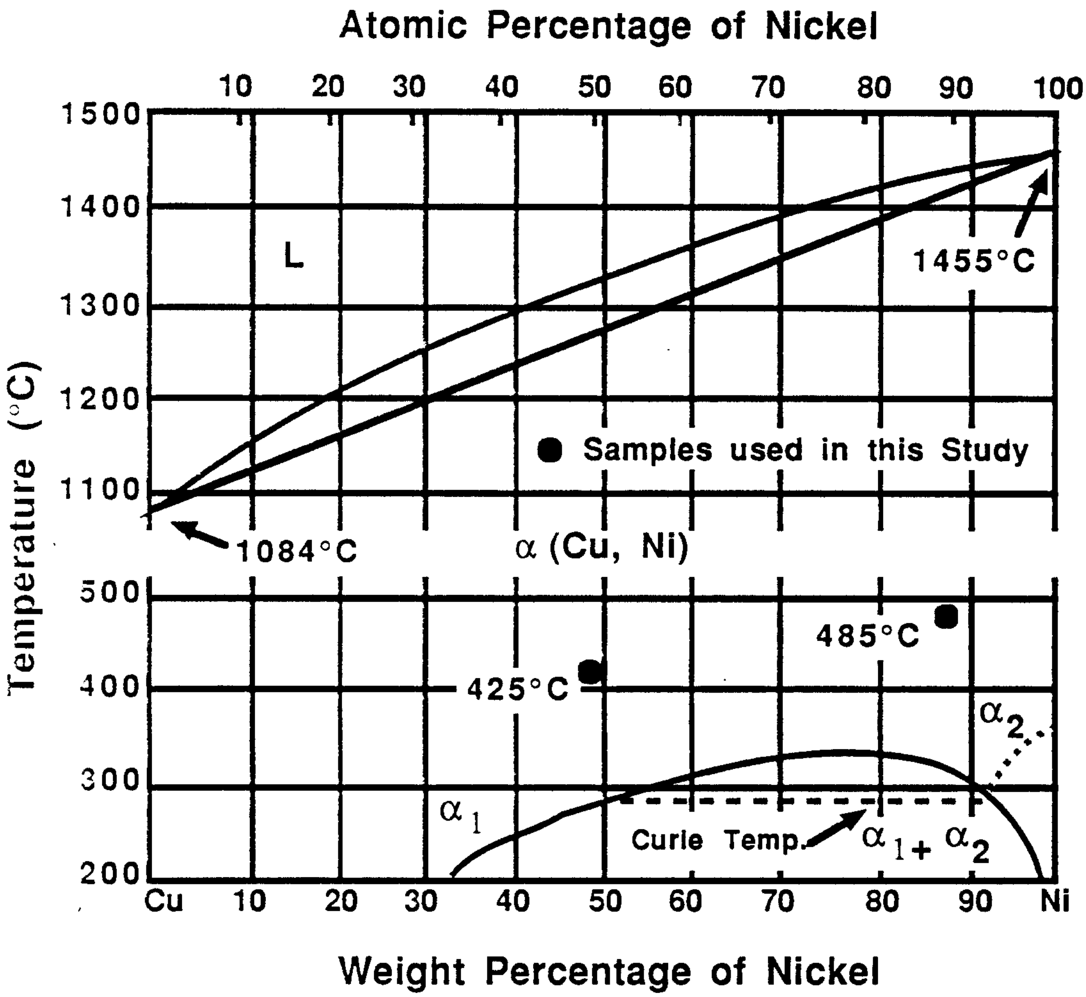

Fig. 4.1. Phase diagram of Cu-Ni system showing compositions used in this study.

application in fusion reactors where both high-conductivity and high-strength are required [17].

The addition of nickel (or cobalt) to the well known copper-beryllium system greatly reduces the maximum solubility of beryllium in the matrix [12,13] and raises the temperature of the α-Cu/γ-beryllide (called β'-beryllide by Chang et al.[13]) peritectic [13]. Addition of beryllium and nickel to copper in equal atomic amounts reduces the solubility of beryllium by an order of magnitude, completely suppresses the Cu_2Be phase and raises the α-γ peritectic (not a eutectic) point to 425°C [13]. This system can be considered a simple eutectic pseudo-binary Cu-NiBe system in the copper-rich corner of the ternary system [11,13-15], as shown in Fig. 4.2. The two phase region consists of an α-copper solid solution and a nickel beryllide (NiBe). The equilibrium NiBe phase is an ordered CsCl structure with Ni (with the occasional substitution of Cu) on the Cs sites and Be on the Cl sites [7,8,11-14,16]. However, this is a classic age-hardening system in which a number of metastable phases precede the equilibrium phase [7-12,14,16,17].

While the Cu-Be-Ni system has not been extensively studied, the Cu-Be system has been thoroughly investigated. Wilkes [22], Bonfield and Edwards [23], and recently Roijo and Laughlin [24] have performed the most complete studies of the precipitation kinetics of the Cu-Be system and their results apply fairly well to the Cu-Be-Ni system. Solution annealing and then quenching creates a supersaturation of Be in the matrix. Aging (usually at elevated temperatures) results in decomposition of the supersaturated

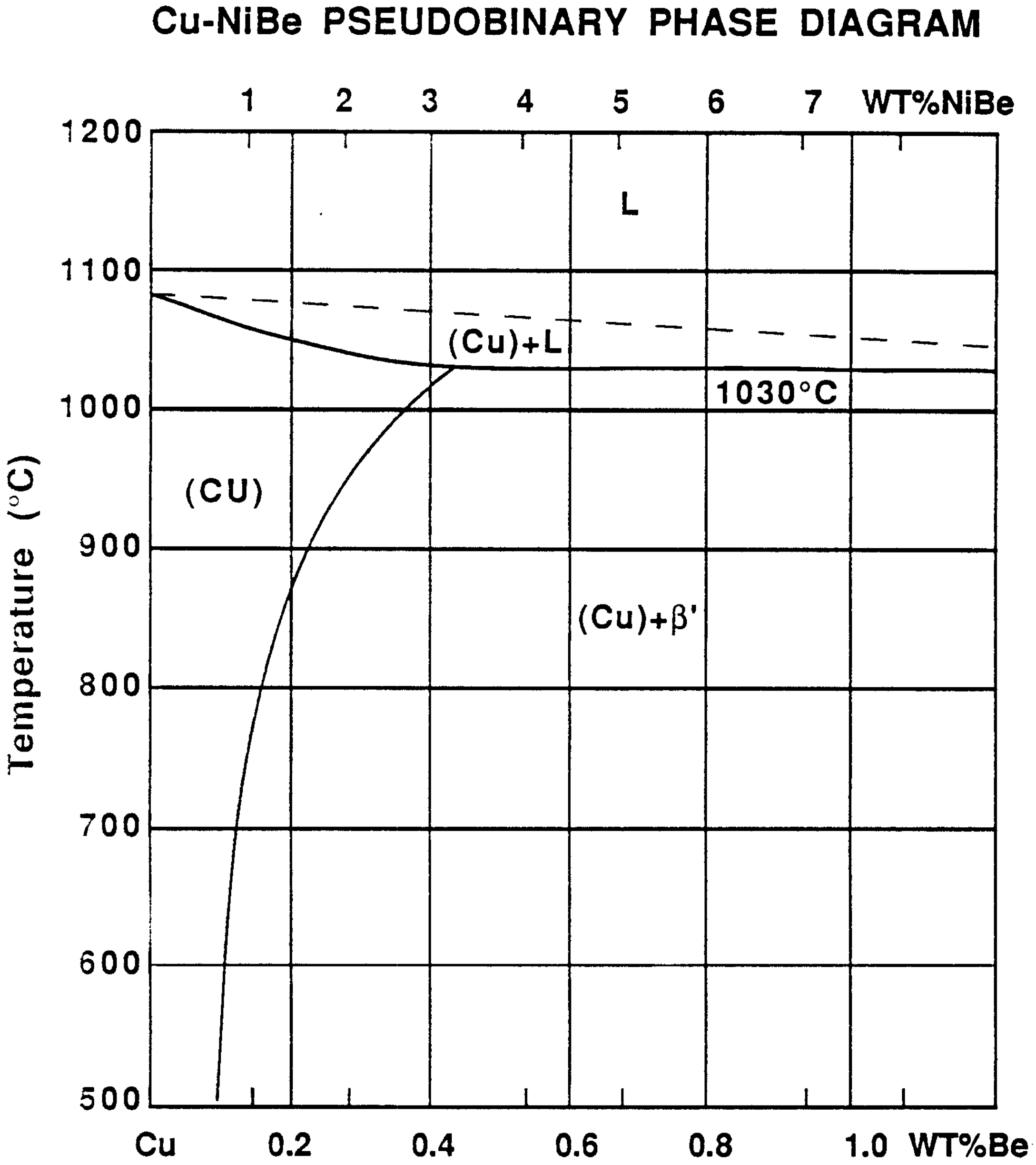

Fig. 4.2. Pseudobinary phase diagram of Cu-NiBe.

matrix via the following precipitation sequence: supersaturated solution $\Rightarrow$ equiaxed Be clusters $\Rightarrow$ G.P. zones (coherent monolayers of Be atoms) $\Rightarrow \gamma''$ (coherent ordered bct platelet) $\Rightarrow \gamma'$ (semi-coherent ordered bcc [CsCl] platelet) $\Rightarrow \gamma$ (equilibrium incoherent ordered CsCl-type phase). The coherency strains of the G.P. zones give Cu-Be alloys their high strength. The coherent γ'' strains the matrix less than the G.P. zones and strengthens Cu-Be alloys less. Each metastable phase forms directly from the previous metastable phase; however, the stable γ phase does not form directly from γ'. γ forms via cellular precipitation at the grain boundaries and then sweeps through the grain.

Copper-beryillium alloys can have very high yield-strengths, but they tend to have very poor conductivity ($Y_{0.2}$ ~180 ksi (1200 MPa) and σ ~20% IACS for Cu-2% Be [25]). This is a result of the large volumetric misfit of both Be (~ 26%) [27] and its precipitates in copper. The resulting strains help strength but diminish conductivity. By lowering the solubility of Be in copper by the addition of Ni (or Co), high strength can be maintained and a significant increase in conductivity can be achieved with a lower solute content [10,14]. As the quasi-binary composition is approached, there is a sharp rise in conductivity and a drop in strength [14,16]. This is attributed to a chemical reaction between nickel and beryllium resulting in a localization of lattice straining [16]. Nickel is co-precipitated with Be, which lowers the matrix straining via ordering effects [14]. This lowers the strength slightly, but greatly improves conductivity and ductility [14].

Overaging limits the temperature range within which precipitation-hardened alloys can be used. Standard Cu-Be alloys are limited to temperatures well below their aging temperature (320°C for Cu-2% Be [25]) as a result of coarsening and cellular precipitation. The addition of Ni significantly retards the kinetics of coarsening [14]. Furthermore, cellular precipitation seems to be eliminated until temperatures exceed the normal aging temperature [12,27] (480°C for Cu-0.3% Be-1.5% Ni [21]). Thus, serious overaging does not occur until temperatures approach 500°C for Cu-Be-Ni [10,12,14,18,19]. The addition of small amounts of very oversized solutes (Nb, Ti, Zn, Zr) increases the strength and conductivity of Cu-Be-Ni alloys and stabilizes them thermally to nearly 500°C [14,28-30]. Additional strength and resistance to overaging and recrystallization can be achieved by solutionizing at higher temperatures (>950°C versus the conventional 900°C) [8]. This increases the amount of Ni and Be in solution (increasing the strength after aging) and forms very stable beryllides (retarding coarsening) [8.].

IV. A. 3 Copper-Alumina Alloys

The Copper-Alumina used in this study contains 0.2% Al as Al_2O_3 (~0.9 vol% Al_2O_3) [31-34]. This alloy (Cu-Al20, CDA No. 15720 or GlidCop Al-20) is generally used in applications where high temperature, high currents and high stresses are found [31-34]. Alloys of this type are presently being considered for use in fusion reactor [35].

The Cu-Alumina alloy system is a relatively simple one. It consists of a pure copper matrix with inert aluminum oxide (Al_2O_3) dispersed throughout. Dispersion strengthened (DS) copper alloys provide a unique way of providing excellent high temperature strength, while maintaining the high thermal and electrical conductivity of pure copper. Mechanical mixing [36], co-precipitation [37] and melting of nitrates [31] were early methods of making DS copper alloys. These methods failed to produce alloys any better than those produced by conventional thermo-mechanical treatments. Internal oxidation has been shown to produce a finer, denser oxide dispersion, thus producing far superior DS copper alloys [31,32,38].

The manufacture of internally oxidized Cu-Al_2O_3 is accomplished via powder metallurgy methods [31,32]. A dilute melt of Al in Cu is is atomized by high pressure gas into a fine powder. It is then blended with an oxidant (Cu_2O) sufficient to oxidize all the aluminum. The blend is heated to 870°C for one hour. Because aluminum is a much stronger oxide former than copper, it is readily converted to alumina instead of copper oxide. As a result of diffusion effects, the smaller the Cu-Al powder the finer alumina dispersoids. Ideally, this process should produce an even distribution of dispersoids about 3.0 nm in diameter. However, at higher aluminum concentrations ($\geq$ 0.6% Al) there is a tendency to obtain regions with a few large particles (> 10.0 nm) [12]. Once all the the aluminum is oxidized, any excess oxygen is reduced by heating the powder in an atmosphere of dissociated ammonia. Failure to remove all dissolved oxygen can result in hydrogen embrittlement at high temperatures [31,39]. Hydrogen embrittlement cause the alloys to form water vapor internally which can result in swelling of up to 40% [39,40].

With only small amounts of discrete alumina particles present, the matrix is essentially pure copper and retains many of pure copper's properties. Cu-Alumina alloys can have electrical and thermal conductivities 80-95% of pure copper, and a melting point, density,modulus and coefficient of thermal expansion nearly identical to pure copper [31 32]. The Cu-Al20 used in this study had a conductivity of ~90% IACS [31-34].

Oxide dispersion strengthened (ODS) alloys have very unique high temperature mechanical properties. Unlike precipitates, the Al_2O_3 particles in the copper matrix are completely inert well beyond the melting point of the matrix (T_{MP} Al_2O_3 = 3500°C versus T_{MP} CU = 1083°C). Room temperature tensile tests and microscopy of non cold-worked alloys after annealing to within 10° of the melting point of copper, show only a slight decrease in strength and no recrystallization [31-34,41-43]. Cold-work greatly increases the strength of these alloys (580 MPa 96% CW versus 320 MPa 0% CW for Cu-Al20), however, annealing over 650°C tends to completely rmoves the effects of cold-working [31-34]. While the room temperature tensile properties of Cu-Al20 are lower than Cu-Ni-Be (580 MPa versus 780 MPa) and stainless steels, its stress-rupture properties at elevated temperatures are far superior to other copper alloys above 400°C [31-34] and as good or better than the 300 series stainless steels at temperatures greater than 650°C [44,45]. Copper-Alumina alloys have excellent fatigue properties

[31,32]. The creep properties of these alloys is very good [31,46]. The amount of elongation at rupture is much smaller than for stainless steels.[45]

IV. B Radiation Effects

IV. B. 1 Ni-Cu Alloys

The Ni-Cu system displays a remarkable resistance to void formation under irradiation [47-53]. No voids have been observed for Ni-Cu alloys with greater than 10% alloying elements. The lack of voids has been attributed to clustering effects which form a high density of traps for vacancies and gas atoms [47,48]. Void formation in Ni-Cu alloys is beyond the scope of this study and is reviewed in reference 47. The following is a brief summary of the effects of irradiation on clustering, which is reviewed more extensively in reference 47.

Clustering has not been directly observed in irradiated Ni-Cu alloys [47]. Segregation of nickel to sinks has been observed in both ion and electron irradiations of Ni-Cu alloys [54-58]. Electrical resistivity, neutron diffraction, positron annihilation and TEM yield results consistent with a clustering mechanism in irradiated alloys [47,48,59-65]. Thermal annealing studies of irradiated Ni-Cu alloys [62-63] produced changes commensurate with those predicted by Elford [3]. The scale of the cluster depends on the alloy content, with more concentrated alloys producing a finer scale of cluster [47,48]. Evidence of the alloy concentration dependence can be seen in the formation of dislocation loops and stacking fault tetrahedra (SFT) [47,48,65].

IV. B. 2. Copper Alloys

The effect of irradiation on copper and its alloys has been thoroughly reviewed recently by Zinkle and Knoll [66,67]. Other reviews have been done by Corbett [68], Adda e.al.[69] and Russell.[70] The following is a brief review of irradiation effects in Cu-Be alloys and Cu-Alumina alloys.

Caution must be used when examining the results and conclusions of electron and ion irradiations (see Chapter II. A and Chapter II. D). Electrons do not produce displacement cascades, so they are limited in simulating neutron and ion damage. The vast majority of ion irradiations have been done with low ion energies (~500 keV) and the results of these studies are probably seriously influenced by surface effects (peak damage depth ~150 nm for 500 keV Cu ions).

No void formation has been observed in Cu-Be containing more than 0.1 at% Be following neutron, electron or ion irradiation [18,19,71-77]. Brager et.al.[18,19,76,77] found that Cu-2% Be densified after neutron irradiation to 63 dpa and showed a small amount of swelling at 98 dpa. No void formation was found in Cu-1.2 at% Be irradiated to 100 dpa by 1 MeV electrons [71]. Irradiation to 40 dpa with 14 MeV Cu ions of 3.4 at% Be copper by Knoll showed no voids [73]. Copper-0.1 at% Be irradiated to 60 dpa with 200 keV Cu ions by Leister swelled more than pure copper, while no swelling was found in Cu-1 at% Be [72]. Only a few studies of Cu-0.3% Be-1.5% Ni have been done [12,18,19,76-78]. A very low density of voids (<<1% swelling) were seen after irradiation up to 20 dpa by 28 MeV Si ions + 30 appm/dpa He at 250-350°C , but no voids were seen above 425°C [12]. In one set of neutron irradiations to 98 dpa at 450°C voids were found in cold-worked and aged samples that had recrystallized with up to ~25% swelling [18,19,76,77]. About 10% swelling was found in solution-annealed and aged samples [18,19,76,77]. A recent irradiation of this alloy to about 30 dpa at 414°C and 529°C shows no significant amount of swelling [78] (~1% versus ~10% at 450°C [19]). Beryllium lowers the stacking fault energy of copper [79,80], thus making SFT more stable relative to voids.

Beryllium is a highly undersized solute in copper (~26% volumetric misfit) [26] and is thought to have an interstitial-solute binding energy greater than 0.9 eV [81]. Thus, Be will tend to strongly segregate to sinks via the interstitial flux as described in Chapter II. E, and because of its low solubility in copper, radiation-enhanced and -induced precipitation can occur. Several extensive studies have been performed on the Cu-Be system to examine RED, RIS, REP and RIP (see Refs. 27-43 in Ref. 66).

Resistivity measurement have been used to study precipitation in Cu-Be alloys following irradiation [82-84]. Low dose irradiations between 0°C and 40°C of supersaturated alloys indicated that REP had taken place [83]. Lensa et.al.[83] and Bartels et.al.[84] studied RIS in undersaturated alloys (up to 0.018 at% Be) during 3 MeV electron irradiation. They found that Be migrated to point defect sinks and that one Be atom was removed from solution for every 2-4 Frenkel pairs.

Yoshida and co-workers [85-88] irradiated copper with 9.5-13 at% Be and some Cu-Be ternaries with neutrons to about 10^{-3} dpa at 20-160°C. They found enhanced formation of G.P. zones and the semi-coherent γ' phase. Precipitation was accelerated by Mg and Zn, while Co and Fe retarded precipitation [88].

Both undersaturated and oversaturated 3.4 at% Be copper alloys were examined by Knoll et al.[73,89-91] following irradiation with 14 MeV Cu ions over the temperature range 300-475°C. Beryllium was found to segregate to the surface by what was thought to be RED. Copious precipitation in the matrix of the equilibrium CuBe phase was found only in the peak damage region for undersaturated alloys and throughout the damage region for supersaturated alloys. Post-irradiation annealing determined that this was RIP and not REP. The precipitates dissolved in undersaturated alloys and were replaced by cellular precipitates in supersaturated alloys.

Irradiations with 650 keV electrons were found to accelerate The kinetics of supersaturated Cu-Be alloys by Kinoshita et al. [92], while irradiation of undersaturated alloys resulted in seemingly homogeneous precipitation. They proposed that interstitial-solute binding caused Be migration to interstitial clusters resulting in homogeneous-like precipitation.

Wollenberger and co-workers have recently studied the effects of 300 keV Cu ions [75,93-95] and 1 MeV electrons [96] on the phase stability of Cu-1.35 at% Be. Like Kinoshita et al. [92], they found that electron irradiation tended to accelerate the precipitation kinetics [96]. Ion irradiations produced homogeneous-like precipitation of the equilibrium CuBe phase without any evidence of metastable phases [75,93-95.] Beryllium segregation to cascade-induced vacancy loops was the proposed cause of the precipitation. Evidence of radiation dissolution of precipitates smaller than 2.5 nm by cascades was observed [75,93].

There have been several recent irradiations of Cu-2% Be [18,19,76,77] and Cu-0.3% Be-1.5% Ni [12,18,19,76,77]. Irradiation of Cu-Be-Ni with 26 MeV Si ions + He up to 20 dpa at 250-500°C resulted in a small amount of coarsening at 425°C, enhanced coarsening at 500°C relative to thermal aging and G.P. zone dissolution below 350°C only when irradiated with both Si and He [12]. No evidence of cellular precipitation was found. Yield strength and resistivity measurements [18] and TEM [19,76,77] were performed on Cu-Be and Cu-Be-Ni after neutron irradiation to 98 dpa at 450°C (yield strength and resistivity only to 16 dpa) [18]. Some radiation-enhanced coarsening was observed and thermally-induced recrystallization was observed in cold-worked alloys.

Only a very few irradiations have been done on Cu-Al_2O_3 alloys [12, 18,19,76-78,97-104). Ion irradiation of Cu-Al60, with 28 MeV Si ions + 30 appm/dpa He to 20 dpa over the temperature range 250-500°C, resulted in localized void formation in regions with a low density of large alumina dispersoids at 300 and 350°C [12]. Fragmentation of the dispersoids was claimed for irradiation over 10 dpa from 250-350°C [12]. No voids have been observed in neutron irradiated Cu-Al_2O_3 alloys [18,19,76-78,98-100,102-104]. Irradiation of Cu-Al25 in FFTF at 450°C to 98 dpa produced only a few percent increase in volume [77], and tensile test of this alloy after only 16 dpa show about a 20% decrease in strength [18]. Other irradiations in FFTF of Cu-Al20 and Cu-Al25 at 410°C to 50 dpa and 530°C to 30 dpa yielded similar swelling and tensile results as the 450°C irradiations [78,98]. Only a welded sample of Cu-Al25 showed poor irradiation response [78,98]. Welding destroys the fine dispersoid distribution [31-34]. The welded area behaves like pure copper, with swelling of about 10% was observed for the entire sample [78,98]. Irradaitions in EBR-II of Cu-Al20 and Cu-Al60 to 15 dpa at 385°C resulted in less than 1% swelling and only 5 to 10% changes in yield strength [99,100,102]. Irradiation of several Cu-Al_2O_3 and Cu-Al-Al_2O_3 alloys in EBR-II at 400°C to 13 dpa also responded well to irradiation [103,104]. The alloys with unoxidized aluminum did not respond as well the fully oxidized alloys [103,104]. Electrical conductivity measurements of the neutron irradiated alloys show that the conductivity of the Cu-Al_2O_3 alloys approaches that of neutron irradiated pure copper and then surpasses it [18,97,102,104,105]. This is a result of the large amount of swelling in pure copper, which negatively affects the conductivity of an alloy [97,102,104,105]. Copper-alumina alloys have had the best overall response to high doses of irradiation at elevated temperatures of all the copper alloys tested [12, 18,19,76-78,97-104].

There has been only one other study of the effects of heavy-ion irradiation on the mechanical properties of copper alloys using the techniques employed in this thesis work [105]. Using the Nanoindenter, Zinkle and Oliver [105] indented, normal to the irradiated surface, OFHC copper irradiated with 4 MeV Fe ions + 50 appm He to 0.1 and 15 dpa at 220°C and 18 dpa at 440°C. Radiation hardening was observed in the near surface region of the 220°C samples, with a 70% hardness increase measured. Only a slight increase in hardness was observed in the 440°C sample. It appears that the radiation hardening at low temperatures saturates at very low fluences. Indentations were made in cross-sectioned samples of 14 MeV Cu ion irradiated OFHC copper (40 dpa peak at 100°C) and AMZIRC (40 dpa at 400°C). An increase in hardness of about 40% was observed in the OFHC copper. The microstructure of the irradiated AMZIRC had previously been compared to the microstructure of AMZIRC samples, with known tensile strength and Vickers microhardness, following various annealing treatments [67 and see Chapter V. A]. Changes in strength after irradiation were extrapolated from the microstructural comparisons. MPM indentations of the AMZIRC sample showed about a 20% decrease in hardness. Using hardness-yield strength correlations this change is similar to those in neutron irradiation and about what was expected from the microstuctural extrapolations.

CHAPTER IV

REFERENCES

1. M. Hansen, **Constitution of Binary Alloys**, 2nd edition, McGraw Hill Book Company, Inc. (1958).
2. B. Mozer, D.T. Keating and S.C. Moss, Phys. Rev. 175 (1968) 868.
3. L. Elford, F. Muller, O. Kubaschewski, Ber Bunsenges Physik Chem. 73 (1969) 601.
4. J. Vrijen, ECN Patten Report, ECN-31 (1977).
5. J. Vrijen and S. Redelaar, Phys. Rev. B 17 (1978) 409.
6. **Metals Handbook**, 8th edition, vol. 8, ASM (1973) 294.
7. A. Guha and W.D. Spiegelberg, Ann. Connector Symp. Proc. 12 (1979) 133.
8. A. Guha, in **High Conductivity Copper and Aluminum Alloys**, E. Ling and P.W. Taubenblat (Eds.), TMS-AIME (1984) 133.
9. J.C. Harkness and C.S. Lorenz, Ann. Connector Symp. Proc. 12 (1979) 38.
10. W. Weinlich, Metall. 34 (1980) 135.
11. S. Spaic and A. Klemencic, Rud. Metal. Zb. 29 (1982) 309.
12. J.A. Spitznagel, et. al., Nucl. Instr.and Meth. B 16 (1986) 279.
13. Y.A. Chang, J. . Neumann, A. Mikula and D. Goldberg, in **Phase Diagrams and Thermodynamic Properties of Ternary Copper-Metal Systems**, INCRA Monograph Series VI (1979) 318.
14. A Mihajlovic, S. Malcio, 0. Nesic, in **Copper and Its Alloys**, Inst. Metal Monograph 34 (1970) 238.
15. J. Tigect, Rev. Metall. 64 (1967) 773.

16. V.M. Glazor, M.V. Stepanova and M.V. Chuprakova, Russ. Metall. No. 3 (1962) 34.

17. S.N. Rosenwasser, in **Copper and Copper Alloys for Fusion Reactor Applications**, F.W. Wiffen and R.E. Gold (Eds.), DOE-OFE Workshop, ORNL, CONF-830466 (1984) 309; See also A. Guha, 143.

18. HR. Brager, H.L. Heinish and F.A. Garner, J. Nucl. Mater. 133/134 (1985) 676.

19. H.R. Brager, J. Nucl. Mater., 141-143 (1986) 163.

20. M. Kostic and D. Mihajlovic, Zast. Mater. 18 (1970) 109.

21. Alloy Dig. Filing Code CU-454 (1983).

22. Wilkes, Ph.D. Thesis, University of Manchester, England (1967).

23. W. Benfield and B.C. Edwards, J. Mater. Sci. 9 (1974) 398.

24. R.J. Rioja and D.E. Laughlin, Acta Met. 28 (1980) 1301.

25. **Metals Handbook**, Vol. 2, "Properties and Selection: Nonferrous Alloys and Pure Metals," 9th Ed., ASM, Metals Park, OH.

26. H.W. King, J. Mater. Sci. 1 (1966) 79.

27 K.B. Alexander, D.H. Stelgerwald and D.E. Laughlin, in **Solid-Solid Phase Transformations**, H.I. Aaronson et al. (Eds.), TMS-AIME (1982) 945.

28. A. Mihajlovic, M. Jovanovic and 0. Nesic, Met. Tech. 6 (1979) 190.

29. A. Mihajlovic, 0. Nesic and V. Perovic, Glas. Hem. Drus. 40 (1975) 557.

30. A. Mihajlovic and 0. Nesic, Glas. Hem. Drus. 44 (1979) 229.

31. A.V. Nadkarni, in **High Conductivity Copper and Aluminum Alloys**, E. Ling and P.W. Taubenblat (Eds.) TMS-AIME (1984) 77

32 A.V. Nadkarni and J. Synk, in **Copper and Copper Alloys for Fusion Reactor Applications**, F.W. Wiffen and R.E. Gold (Eds.), DOE-OFE Workshop, ORNL, CONF-830466 (1984) 152.

33 Alloy Digest, Filing Code CU-546 (1982.

34 Technical Data Sheet, Bulletin No. 1404, SCM Metal Products (1980).

35 F.W. Clinard, Jr., in **Copper and Copper Alloys for Fusion Reactor Applications**, F.W. Wiffen and R.E. Gold (Eds.), DOE-OFE Workshop, ORNL, CONF-830466 (1984) 347.

36 K.M. Zwilsky and N.J. Grant, Trans. AIME 221 (1961) 371.

37 M.F. Grimwade and K. Jackson, Powder Met. 10 (1962) 13.

38 O. Preston and N.J. Grant, Trans. AIME 221 (1961) 164

39 S.J. Zinkle, ADIP Semiannual Report, DOE/ER-0045/16 (1986).

40 D.H. Plantz, unpublished research.

41. E.N.C. Dalder, W. Ludemann and B. Schumacher, in **Copper and Copper Alloys for Fusion Reactor Applications**, F.W. Wiffen and R.E. Gold (Eds.), DOE-OFE Workshop, ORNL, CONF-830466 (1984) 252.

42. N.J. Grant, in **Copper and Copper Alloys for Fusion Reactor Applications**, F.W. Wiffen and R.E. Gold (Eds.), DOE-OFE Workshop, ORNL, CONF-830466 (1984) 332.

43. N.J. Grant, A. Lee and M. Lou, in **High Conductivity Copper and Aluminum Alloys**, E. Ling and P.W. Taubenblat (Eds.) TMS-AIME (1984) 103.

44. O.K. Harling, G.P. Yu, N.J. Grant and J.E. Meyer, J. Nucl. Mater. 103/104 (1981) 127.

45. N.J. Grant, in **Copper and Copper Alloys for Fusion Reactor Applications**, F.W. Wiffen and R.E. Gold (Eds.), DOE-OFE Workshop, ORNL, CONF-830466 (1984) xxxiv.

46. B. Burton, Metal Science Journal 5 (1971) 11.

47. L.-M. Wang, Ph.D. Thesis, Materials Science Program, University of Wisconsin-Madison (1988)

48. L.-M. Wang, R.A. Dodd and G.L. Kulcinski, J. Nucl. Mater. 155-157 (1988) 1241.

49. J.L. Brimhall and H.E. Kissinger, Rad. Eff. 15 (1972) 259.

50. D.J. Mazey and F.Menzinger, J. Nucl. Mater. 48 (1978) 15.

51. K.-H. Leister, Ph.D. Thesis, Kernforschungszentrum, Karlsruhe, W. Germany (1983)

52. P. Dauben and R.R. Wahi, Progress Report 2 (1981-1984) Hahn-Meitner Institute.

53. P. Barlow, Ph.D. Thesis, University of Sussex-United Kingdom (1977).

54. H. Shimizu, et.al., J. Japan Inst. of Metals 45 (1981) 210.

55. H. Shimizu, et.al., J. Japan Inst. of Metals 45 (1981) 678.

56. L.E. Rehn, W. Wagner and H. Wiedersich, Scripta Met. 15 (1981) 683.

57. H. Takahashi, S. Ohnuki and T. Takeyama, J. Nucl. Mater. 103/104 (1981) 1415.

58. T. Takeyama, Bull. Japan Inst. Met. 22 (1983) 135.

59. W. Schule, P. Spindler and E. Lang, Z. Metallk. 66 (1975) 50.

60. K. Chountes, et.al., Rad. Eff. Letters 43 (1979) 249.

61. S.J. Zinkle and G.L. Kulcinski, J. Nucl. Mater. 122/123 (1984) 449.

62. R. Poerschke and H. Wollenberger, Thin Solid Films 25 (1975) 50.

63. R. Poerschke and H. Wollenberger, Rad. Eff. 49 (1980) 225.

64. W. Wagner, R. Poerschke and H. Wollenberger, J. Phys. F 12 (1982) 405.

65. B.N. Sigh, T. Leffers and P. Barlow, Fifth International Conference on HVEM, Kyoto, Japan (1977) 581.

66. S.J. Zinkle and R.W. Know, "A Literature Review of Radiation Damage Data for Copper and Copper Alloys," June 1984 UWFDM- 578.

67. S.J. Zinkle, Ph.D. Thesis, Nuclear Engineering Department, University of Wisconsin-Madison (1985).

68. J.W. Corbett, **Electron Radiation Damage in Semiconductors and Metals**, Solid State Physics Supplement 7, Academic Press (1966).

69. Y. Adda, M. Beyeler and G. Brebec, Thin Solid Films 25 (1975) 107.

70. K.C. Russell, Progress in Materials Science (1984).

71. M.J. Makin, in **Voids Formed by Irradiation of Reactor Materials**, S.F. Push (Ed.), ANES (1971) 269.

72. K-H. Leister, Ph.D. Thesis, Kernforschungszentrum, Karlsruhe (1983) Kfk Report 3499.

73. R.W. Knoll, Ph.D. Thesis, Nuclear Engineering Department, University of Wisconsin-Madison (1981).

74. C. Kinoshita and T.E. Mitchell, Electron Microscopy 4 (1980) 263.

75. M.-P. Macht, V. Naundorf, R. R Wahi and H.Wollenberger, J. Nucl. Mater. 122/123 (1979) 698.

76. H. R. Brager, J. Nucl Mater. 141-143 (1986) 79.

77. H. Brager and F.A. Garner, in ASTM STP 1046, in press.

78. F.A. Garner, H.R. Brager and K.R. Anderson, FRM Semiannual Progress Report, DOE/ER-0313/7 (1989) 223.

79. A. Stathopoules, et.al., Phil. Mag. A 44 (1981) 309.

80. A. Stathopoules and C.A. English, J. Nucl. Mater. 108/109 (1982) 69.

81. H. Wollenberger, J. Nucl. Mater. 69/70 (1978) 362.

82. G.T. Murray and W.E. Taylor, Acta Met. 2 (1954) 52.

83. W.L. Lensa, A. Bartels, F. Dworschak and H. Wollenberger, J. Nucl. Mater. 71 (1974) 78.

84. A. Bartels, F. Dworschak, H. . Abromet and H. Wollenberger, J. Nucl. Mater. 83 (1979) 24.

85. H. Yoshida, Phil. Mag. 19 (1969) 987.

86. H. Yoshida and T. Sagane, J. Nucl. Sci. Tech. 9 (1972) 1.

87. H. Yoshida, in **Solid-Solid Phase Transformations**, TMS-AIME (1982) 299.

88. H. Yoshida, S. Yamamoto, Y. Murakami and H. Kodaka, Trans. J.I.M. 12 (1971) 229.

89. R.W. Knoll, P. Wilkes and G.L. Kulcinski, in **Phase Stability During Irradiation**, J.R. Holland, L.K. Mansur and D.I. Potter (Eds.), Pittsburgh, TMS-AIME (1981) 123.

90. R.W. Knoll and G.L. Kulcinski, J Nucl. Mater. 131 (1984) 172.

91. R.W. Knoll and G.L. Kulcinski, J Nucl. Mater. 131 (1984) 187.

92. L. Kinoshita, L.W. Hobbs and T.E. Mitchell, in **Phase Stability During Irradiation**, AIME (1981) 561.

93. R. Koch, R. R Wahi and H. Wollenberger, J. Nucl. Mater. 103/109 (1981) 1216.

94. M.-P Macht, V. Naundorf and H. Wollenberger, J. Nucl. Mater. 103/104 1487.

95. H-J Gudradt, V. Naundorf, M- P Macht and H. Wollenberger, J. Nucl. Mater. 118 (1983) 73.

96. R. R Wahi and H. Wollenberger, J. Nucl. Mater. 11 (1983) 207.

97. K.R. Anderson, F.A. Garner, M.L. Hamilton and J.F. Stubbins, FRM Semiannual Progress Report, DOE/ER-0313/6 (1989) 357.

98. K.R. Anderson, F.A. Garner, M.L. Hamilton and J.F. Stubbins, FRM Semiannual Progress Report, DOE/ER-0313/7 (1989) 213.

99. R.J. Livak, T.G. Zucco and J.C. Kennedy, ADIP Semiannual Progress Report, DOE/ER-0045/14 (1985) 152.

100. R.J. Livak, H. M. Frost, T.G. Zucco, J.C. Kennedy and L.W. Hobbs, J. Nucl. Mater. 141-143 (1986) 160.

101. H. M. Frost and , J.C. Kennedy, J. Nucl. Mater. 141-143 (1986) 169.

102. R.J. Livak, T.G. Zucco and L.W. Hobbs, J. Nucl. Mater. 144 (1987) 121.

103. M. Ames, G. Kohse, T.-S. Lee, N.J. Grant and O.K. Harling, J. Nucl. Mater. 141-143 (1986) 169.

104. O.K. Harling, N.J. Grant, G. Kohse, M. Ames, T.-S. Lee and L.W. Hobbs, J. Mater. Res. 2 (1987) 568.

105. S.J. Zinkle and W.C. Oliver, J. Nucl. Mater. 141-143 (1986) 548.

CHAPTER V

EXPERIMENTAL PROCEDURE

V. A Materials Investigated

The first phase of this study investigated the relationship of radiation-induced dislocation loops to strength changes in two Ni-Cu alloys (Ni–10 at% Cu and Ni–50 at% Cu). These alloys had a very low impurity content and were in the solution-annealed condition (i.e. nearly dislocation free) [1]. The initial microindentation hardness, as determined by the MPM at a depth of 300 nm, and the irradiation conditions are shown in Table 5.1. More details of the history of the alloys can be found in reference 1

The alloy used in the main phase of this thesis was a precipitation hardened, high-strength, high-conductivity beryllium copper alloy containing nickel (Cu–1.5% Ni–0.3% Be). The alloy was manufactured by Brush Wellman using oxygen-free, high-conductivity copper [2] and was provided by Inesco, Inc.[3] This alloy meets the specifications of copper alloy number C17510 (known commercially as Brush Alloy 3) [4]. The impurity content of this alloy is listed in Table 5.2 [5].

Two different thermomechanical treatments of the Cu-Ni-Be alloy were used. The as-received alloy has been solutionized at 899°C (1650°F), then 20% cold-worked and, finally, aged at 482°C (900°F) for 3 hours.[5] Some of the as-received alloy was subsequently resolutionized at ~950°C

Table 5.1. **Initial Microindentation Hardness and Irradiation Conditions for Ni-Cu Alloys**

Composition	MPM Hardness (300 nm)	Irradiation Temperature	Dpa (1 μm)	Dpa (Peak)
Ni–10%Cu	2.1 GPa	485°C	5	20
			10	40
			25	100
Ni–50% Cu	2.0 GPa	425°C	5	20
			10	40
			25	100

Table 5.2 **Alloying and Impurity Elements in Cu–1.5% Ni–0.3% Be**

Element	ppm	Element	ppm
Al	100	Ni	14900
Be	3000	Pb	<30
Co	<100	Si	100
Cr	<50	Sn	<50
Fe	<100	Zn	100

for ~0.33 hours and then aged for 3 hours at 480°C, in order to remove the cold working. The properties of the as-received alloy [5], as well as Vickers microindentation hardness and MPM measurements (done by the author) of the alloy in both states, are listed in Table 5.3. The irradiation conditions are listed in Table 5.4.

A dispersion hardened copper alloy (Cu–Al20) was also irradiated. It is a high-strength, high-conductivity copper alloy with 0.2 wt% aluminium dispersed through the alloy as alumina (Al_2O_3). The alloy meets the specifications of Copper Alloy Number C15720 (known commercially as GlidCop AL-20) [6]. The alloy was manufactured by SCM Metal Products and was provided by Los Alamos. The impurity level of the Cu-Al20 is not known; however, it is expected that the level is similar to the Cu-Al60 alloy used by Livak, et.al.[7] and Spitznagel, et.al.[8]. The alloy was heavily cold-worked (~90%) and microindentation hardness measurements(with the MPM) were about 1.5 GPa at a depth of 1 µm. Table 5.4 lists the irradiation conditions for Cu-Al20.

V. B **Irradiation Facility**

The University of Wisconsin Heavy-ion Irradiation Facility was used for all of the irradiations [9]. A schematic of the facility is shown in Fig. 5.1. A SNICS [10, 11] (Source of Negative Ions by Cesium Sputtering) source is used to produce a high current (30 µA) of Cu^- (or other negative ions). This Cu^- beam is "steered" into a tandem Van de Graaf accelerator (High Voltage Engineering Corp. , model EN) and accelerated into the high-voltage

Table 5.3 Physical and Mechanical Properties of Cu–Ni–Be

Property	Cold-Worked & Aged	Solution-Annealed & Aged
Ultimate Tensile Strength (MPa)	860	
Yield Strength (MPa)	780	
Elongation (% in 2 in.)	13	
Rockwell Hardness	Rc 23	
Electrical Conductivity (% IACS)	69.2	
Vickers Microhardness (200 g) (GPa)*	2.20	2.35
MPM Microhardness (1500 nm) (GPa)*	3.00	3.30
MPM Young's Modulus (GPa)*	145	140

* Measurements made by author

Table 5.4. Irradiation Conditions for Cu–Ni–Be and Cu–Al20

		Dpa		Temperature (°C)				
Alloy	Condition	1 µm	Peak	100	200	300	400	500
Cu–Ni–Be	Cold-Worked & Aged	10	40	X	X	X	X	X
	Soln-Ann & Aged	10	40	X	X	X	X	X
Cu–Al20	Cold-Worked	20	80		X	X	X	X
		40	160			X	X	

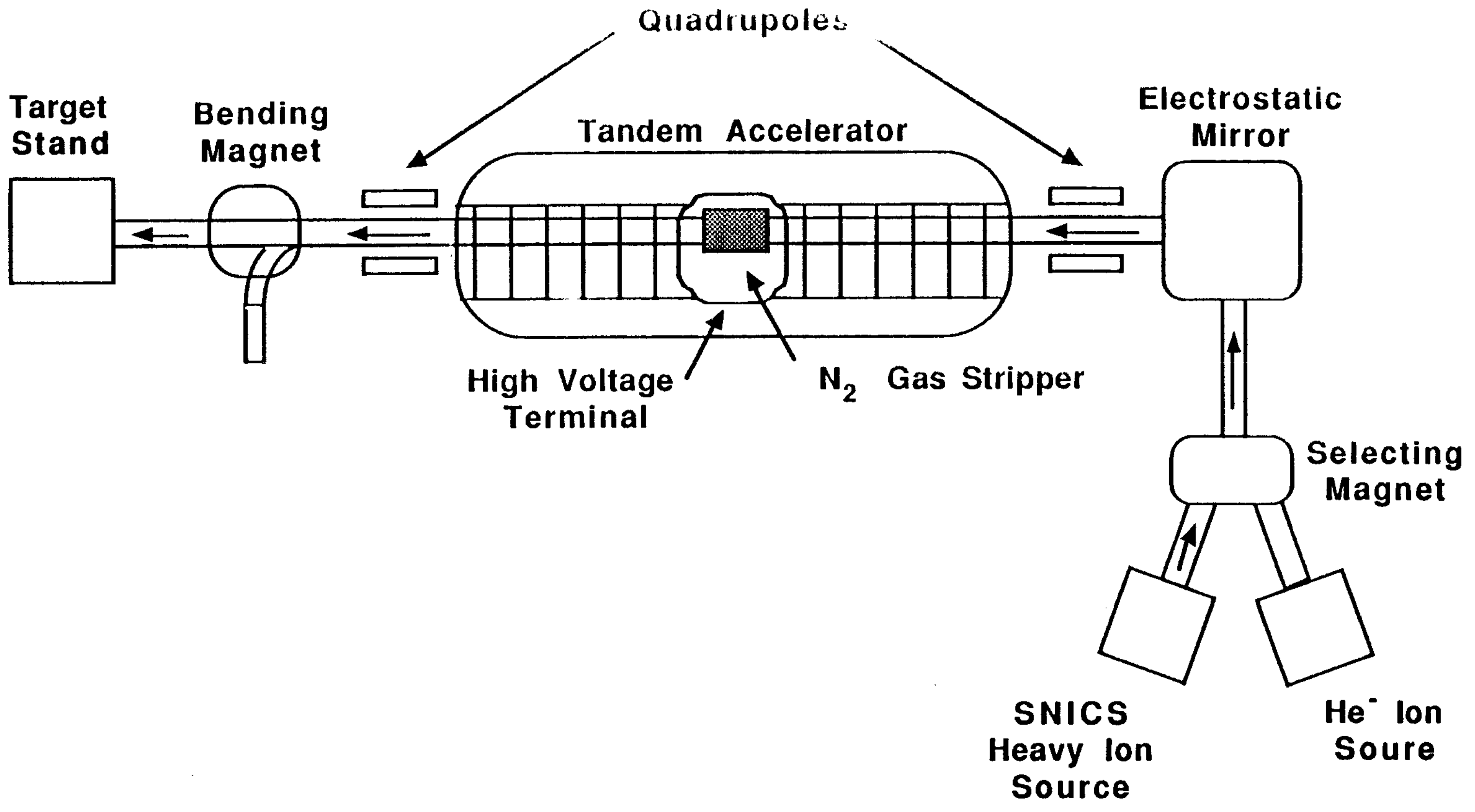

Fig. 5.1. Schematic of the University of Wisconsin Heavy–Ion Irradiation Facility.

terminal (at +V). A gas stripper converts the beam into Cu^{+n} which is accelerated away from the terminal. The beam is then focused on the target. The final energy of the ions is given by $E_{ion}=qV(l+n)$ where q is the electronic charge. Charge state analysis indicates that proper lens and magnet settings at a dome voltage of 3.5 MV results in 99% of the beam being 14 MeV Cu^{+3}.

The samples are mounted in a carousel holder designed such that the samples not being irradiated are thermally isolated from the sample being irradiated at high temperature [12]. The temperature range available is 100-700°C with the lower limit a result of beam heating. A high vacuum at the sample of $\sim 10^{-7}$ torr is maintained during irradiation. Beam current is measured periodically by Faraday cups located in front of and behind the sample. Beam stability is monitored by a 3 mm mask aperture in front of the sample which defines a beam on target of essentially constant intensity profile. A current of $\leq$ 100 nA of Cu^{+3} ($\sim 10^{-3}$ dpa/sec) is typical during an irradiation.

V. C Sample Preparation

Proper preparation of samples is a key to obtaining accurate results for both microscopy and microindentation hardness testing. Unirradiated samples must be prepared for either irradiation, microscopy or indentations. Post-irradiated samples must be prepared for both indentations and plating for cross-sectional analysis. Once plated, specimens must be sectioned and then prepared for more indentation tests and finally TEM (Transmission

Electron Microscopy). A mistake at any point could affect the results of a test at another point in the chain. Except for the details of sample preparation for indentation tests all details for the Ni-Cu alloys may be found in reference 1.

V. C. 1 Pre-Irradiation Sample Preparation

Some of the as-received cold-worked and aged Cu-Ni-Be alloy was encapsulated in evacuated Vycor tubes and solution-annealed at about 950°C for 0.33 hours. This removed all traces of cold-work and put almost all of the solutes into solution. Most of the solution-annealed material was then aged at 482°C for 3 hours in order to reprecipitate the solutes. Some of both thermo-mechanical treatments (TMT) were subsequently aged further at 300-400°C for 10-1000 hours in a limited aging study.

Samples of both copper alloys were cut into 5 mm by 10 mm foils 250 µm thick. The foils were first mechanically polished using successively finer grades of emery paper (down to 600 grit), followed by polishing on a wheel with 1 µm diamond and/or 0.3 µm alumina, and then on a Syntron metallographic polisher using a slurry of 0.05 µm alumina powder and/or MasterMet® polishing solution (0.06 µm silica in a basic solution). Immediately prior to indentation or irradiation the foils were electropolished (33% $HN0_3$/67% CH_30H, -40°C, 10 V) to remove the work-hardened surface layer caused by mechanical polishing. To prevent the introduction of gas into the foils a low electropolishing temperature was used. Some indentation tests were preformed on samples with only the final mechanical polish.

V. C. 2 Post-Irradiation Sample Preparation

After irradiation the "beam spot" was marked and the samples were stored in a vacuum dessicator until they were prepared for analysis. The samples were prepared following procedures outlined by Zinkle and Sindelar [13], modified for microindentation hardness testing, and briefly described below. Figure 5.2 outlines the steps needed to produce a cross-sectioned specimen. The foil was cleaned by a light swabbing with a dilute solution of 0.05 µm alumina followed by ultrasonic cleaning in an acetone bath. At this point the Cu-Ni-Be alloy was indented in the MPM. The foils were then transferred to the plating solution (180 g $CuS0_4$, 30 ml H_2S0_4, 950 ml H_20) where they were made anodic for 1 second (100 mA/cm^2). This cleaning process removes less than 0.1 µm. The polarity was then reversed to begin electroplating. A magnetic stirrer was used to agitate the solution and prevent the build up of hydrogen formed by electrolysis, which can result in porosity in the plating.. After 12 to 18 hours the plating thickness exceeded 3 mm and was stopped. The plated sample was sliced normal to the foil surface into thin sections (150-250 µm thick). About 5-8 slices from the irradiated region could be obtained.

V. C. 3 Cross-Section Microindentation Sample Preparation

Cross-sectioned samples were mechanically polished to either a 0.05 µm finish with alumina or to a slightly better finish with MasterMet® polishing solution. All alloy specimens were electropolished using 67% CH_3OH and 33% HNO_3 polishing solution. The conditions for the

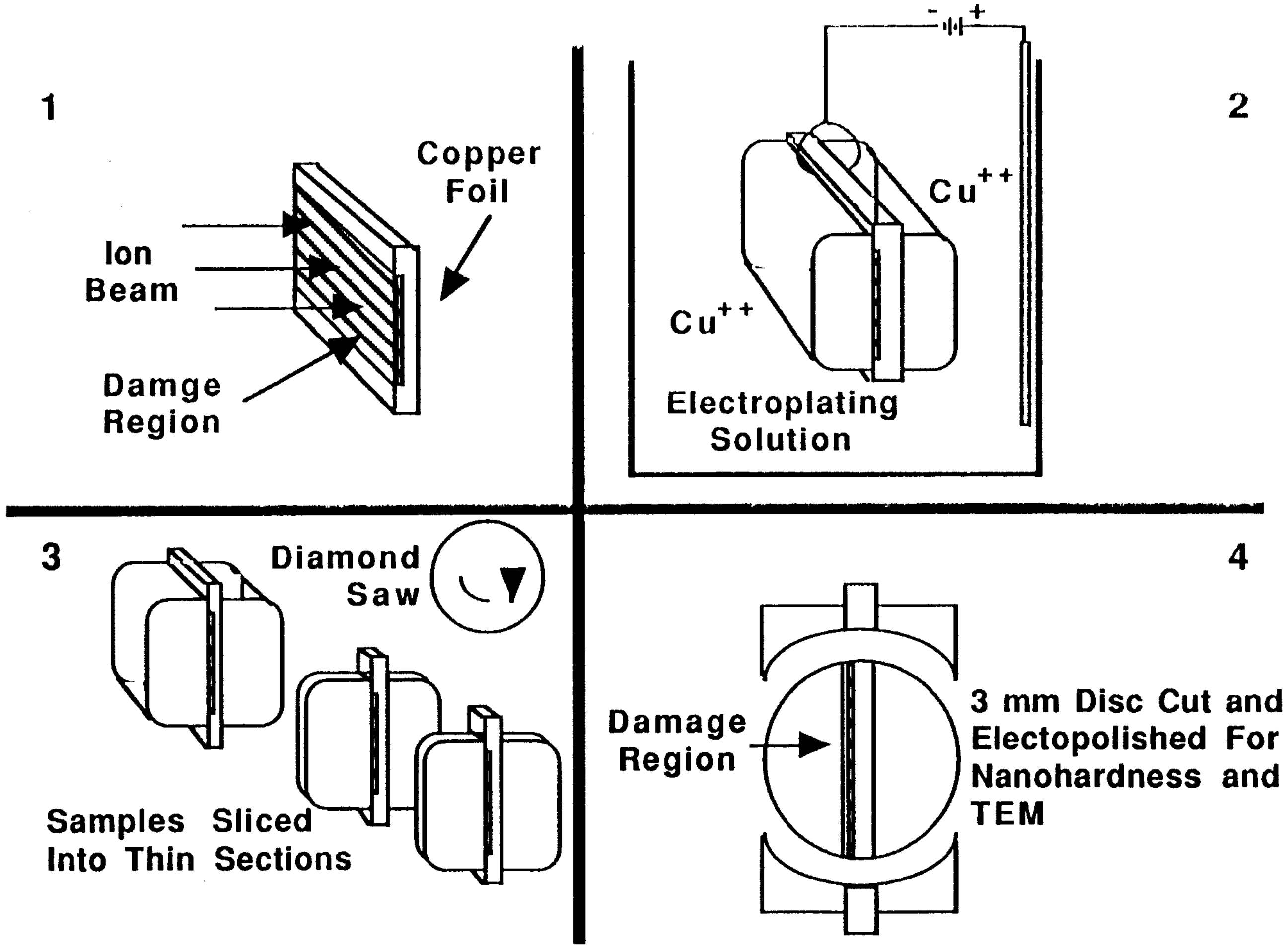

Fig. 5.2. Outline of procedure to prepare cross-section specimens for the TEM and the MPM.

Ni-Cu alloys were 15 V at -30°C to -50°C for <5 seconds. The copper alloys were polished at 5 V at -30°C for <5 seconds.The foil was preferentially polished at the interface between it and the plating. This was reduced by polishing at very low temperatures and keeping the time to a minimum. Some preferential polishing was needed in order to see the interface for indenting. As a result, very often the first few microns from the plating were not level enough to indent. This was a particular problem with the Ni-Cu alloys because of the amount of alloying elements(>10% versus <5% for the copper alloys). These specimens were repolished with MasterMet® (at a very low load to reduce mechanical polishing artifacts) to level the interface. The basic pH of the MasterMet®, etched the interface enough so it could be seen without overpolishing the first few microns of the foil.

V. C. 4 TEM Sample Preparation

The plating slices were ground down to less than 150 μm thick and then 3 mm disks were punched out with the irradiated region centered. The discs were prepared for electrothinning by lacquering all but a thin region around the irradiated surface on one side and completely masking off the other side. A Fishcione™ jet electropolisher using a 33% $HN0_3$/67% CH_30H solution at -25°C and operated at 10-15 V (90-100 mA) was used for thinning. The lacquered discs were electropolished for 15-20 seconds. Then the lacquer was removed, and the process repeated for the other side. Once this was completed the sample was polished until perforation. If no thin area was found the disc was ion milled at a few kV at about 12° for 15-

30 minutes and checked for thin area. The milling was repeated until adequate thin area was achieved.

V. D Sample Analysis

V. D. 1 Conventional Microindentation Hardness Testing

Vickers and Knoop microindentation hardness measurements were made on a Micromet II® designed for a load range of 10 to 1000 g and a Micromet II® designed for a load range of 0.5 to 50 g. All tests on the low-load machine were done with vibration isolation; however, only some tests on the high load machine were done with vibration isolation. At least 5 indentations were made in a sample.

V. D. 2. The Mechanical Properties Microprobe

Ultra-low load microindentation hardness measurements were performed on a recently developed, fully automated Mechanical Properties Microprobe (MPM) (known as the Nanoindenter and manufactured by Nano Instruments, Inc.) [14,15]. A schematic of the MPM is shown in Fig. 5.3. A well controlled voltage is applied to the indenter (creating a downward force on it) and then removed once maximum force has been achieved. The displacement of the indenter causes a change in voltage between the capacitor and a plate connected to the indenter that floats in the capacitor. Both the applied voltage and the voltage between the capacitor and the plate are monitored continuously and have been calibrated to load and displacement

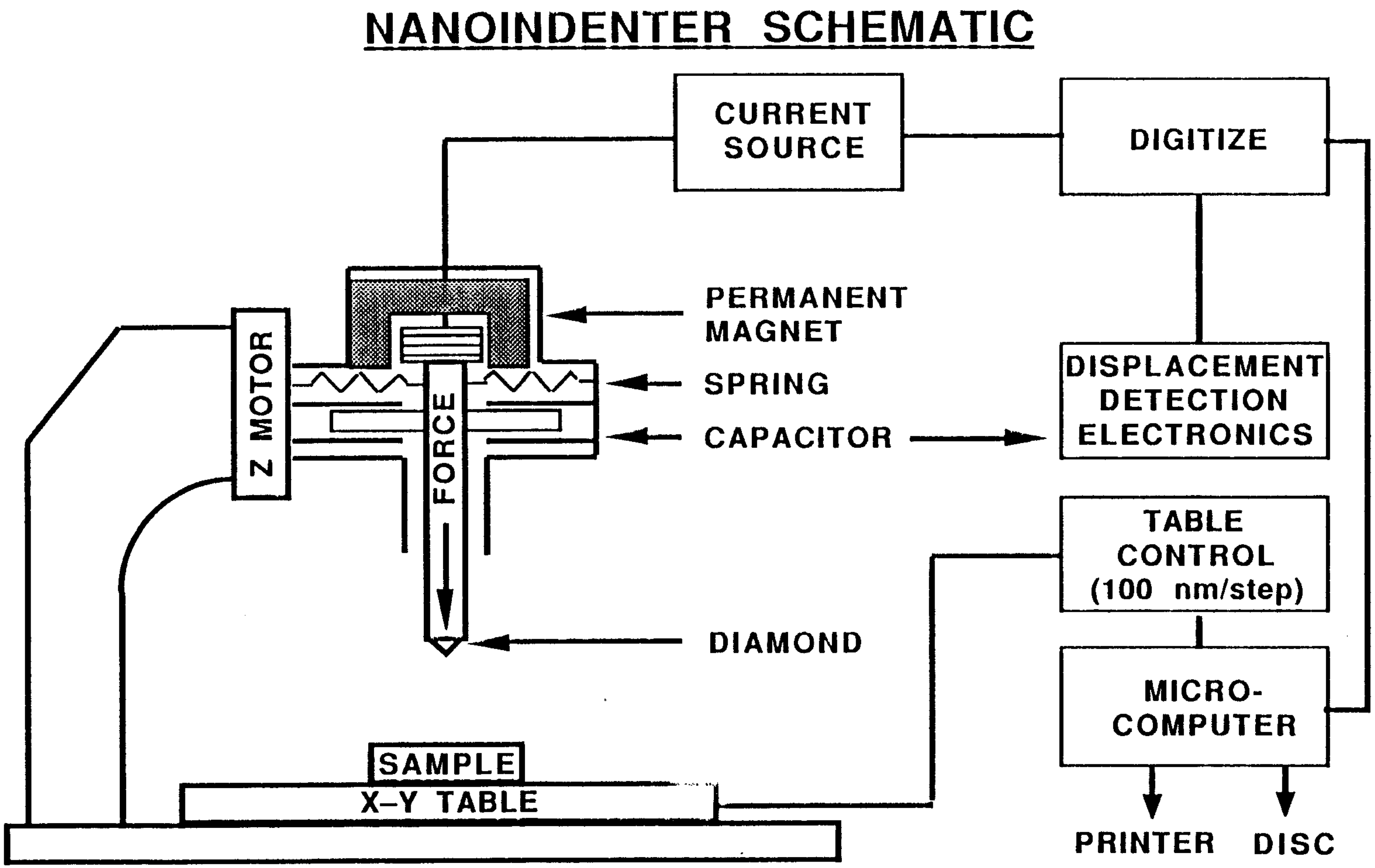

Fig. 5.3. Mechanical properties microprobe (MPM) schematic

respectively. Table 5.5 lists the capabilities of the MPM. A typical load-displacement curve obtained from the MPM is represented in Fig. 5.4.

In order to achieve the maximum depth resolution, the MPM is kept on an anti-vibration air table in a thermally stable enclosure. Prior to the start of any group of indentations, a drift test is performed to determine if thermal and vibrational drift is small enough to have an insignificant effect on the data. Normally a drift rate less than 0.1 nm/s must be maintained for a minute before indentations can begin. During most indentations the drift rate is <0.05 nm/s. This results in less than 1% error from thermal and vibrational effects. The system can not block out strong, low frequency events (e.g. slammed doors, large machinery being turned on or off) and the load-displacement curves of each indentation must be examined closely for evidence of such events. Such events occur frequently (every 10 to 20 minutes) during the hours of 7 am to 6 pm, Monday through Friday. At other times, only a few such events occur (< 1 event / 6 hours).

Exact depth measurement is achieved by knowing where the surface is. The MPM knows roughly where the surface is before every indentation. It begins looking for the surface approximately 1 μm above the surface. The indenter is slowly (very low loading rate) lowered to the surface (~5 nm/s) until resistance is met and the loading is terminated. The force with which the indenter "hits" the surface is not enough to damage the surface [14,15]. This point is assumed to be zero (0) depth for that indentation.

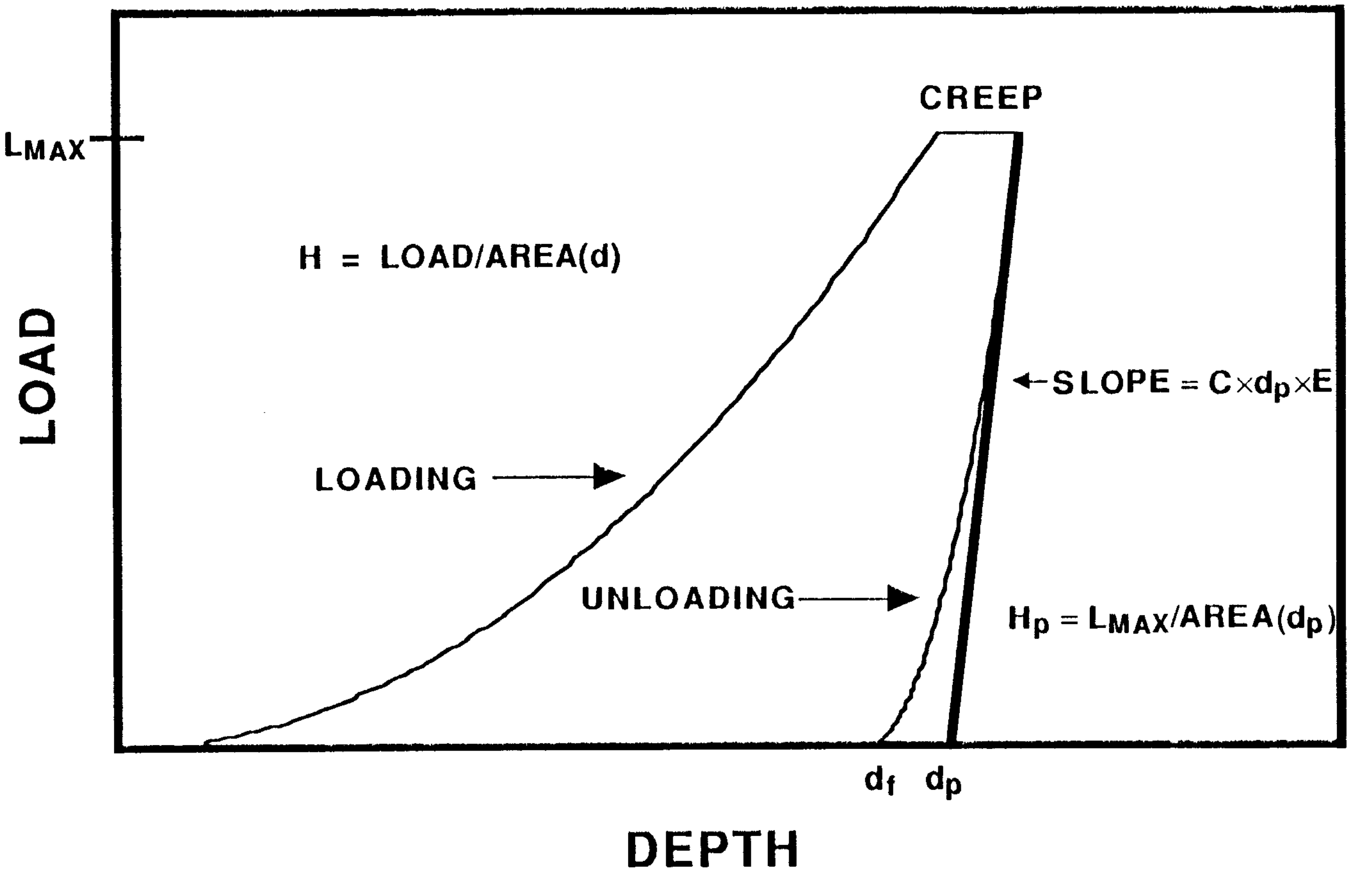

Fig. 5.4. Representative load-displacement curve from the NanoIndenter (MPM).

Table 5.5 Capabilities of the Nanoindenter

Depth Resolution	± 0.4 nm
Force Resolution	± 2.5 µN (250 µg)
Load Application	0-3 g (12,000 steps)
	0-12 g
X-Y Positioning	± 1.0 µm 1st indentation
	± 0.1 µm movement

Once load and displacement voltages are converted to actual loads and displacements, corrections are made to these value to account for the compliance of the MPM and the stiffness of the spring holding the indenter. The load is corrected for the spring's resistance to movement. The force of indentation not only causes the sample to be indented, but also pushes the rest of the MPM apart. This means that the indenter moves more than the amount it indents into the sample. The amount of the extra movement is proportional to the load applied and must be subtracted from the the total indenter movements to get the actual indentation depth.

Hardness under load (uncorrected for elastic effects) can be calculated from the loading curve as a function of depth using $H = AL/d^2$, where d is the depth of penetration on the loading curve, L is the load at that depth and A is a geometric factor relating depth to the projected area (PA) of the indentation. The indenter's diamond tip is a triangular based Berkovitch pyramid, which has a depth to projected area ratio identical to a Vickers pyramid. Ideally, for the Berkovitch pyramid, PA = 24.56 d^2; however, the diamond is slightly blunted and this shape effect must be taken into account in order to get accurate hardness results.

Analysis of the unloading portion of the load-displacement curve yields both plastic hardness and the Young's modulus [16,17]. The plastic hardness is equivalent to the hardness measured in conventional indentation hardness tests. Plastic hardness is given by $H_p = AL_{max}/d_p^2$, where L_{max} is the maximum load applied and d_p is the maximum depth corrected for elastic effects [16]. It has been shown the initial slope of the unloading curve is proportional to the plastic depth (d_p) and Young's modulus (E) [16,17]. For an ideal Berkovitch diamond the relationship is:

$$\frac{dL}{dd} = 2\, d_p\, E_r \left(\frac{24.56}{\pi}\right)^{1/2} \qquad 6.1$$

where E_r is a composite modulus given by the following relationship:

$$\frac{1}{E_r} = \frac{1 - v_s^2}{E_s} + \frac{1 - v_o^2}{E_o} \qquad 6.2$$

and E_s and v_s , as well as E_o and v_o are the Young's modulus and Poisson's ratio for the sample and the diamond indenter respectively. The modulus can be determined from an individual unloading curve or it can be determined from the slope of a plot of dd/dL (the sample compliance) versus

d_p for a number of indentations of various indentation depths. The second method is better if the nonsample compliances (MPM's, sample mount, etc.) are not well known because they only shift the plot up or down, but they change the slope of the individual unloading curves. The y-intercept of dd/dL versus d_p is a measure of the extra compliance that needs to be accounted for.

V. D. 3. Mechanical Properties Microprobe Calibration

Careful calibration of the mechanical properties microprobe (MPM) or Nanoindenter is essential to its reliable operation. Calibration of the Nanoindenter's compliance, spring stiffness, and displacement and load measurements were performed by Dr. J. B. Pethica of Nano Inc. when the machine was assembled. These calibrations remain constant over time. Two other calibrations required are the shape of the diamond indenter and the compliance of the sample mountings. These calibrations do not remain constant over time and must be continually checked by the operator.

As stated above the Berkovitch diamond indenter is slightly blunted. This blunting can be modeled as a parabola of revolution with the corrected area to depth relation given by the relationship, $PA = 24.56\ d^2 + A1\ d^{1.5} + A2\ d$. The coefficients A1 and A2 are geometric variables depending on angle of the diamond faces to the vertical axis (65.3°) and the tip radius of the parabola (r). The area/depth relationship can be determined by either direct imaging of the indentations and measuring the area for a given depth, or from the analysis of compliance versus $1/d_p$ for indentations made over a wide range of depths.

For the first method, indentations made in alpha brass were observed using a high-resolution SEM. Figure 5.5 shows indentations to 20, 40 and 60 nm deep (left) and an indentation to 20 nm deep (right). Shallow indentations are extremely difficult to image. It is also very difficult to account for piling up of material around the indentation and elastic recovery distortion of the indentation edges after the indenter is removed.

Equation 6.1 shows the relationship between sample compliance, plastic depth and sample modulus (E) for an ideal indenter. For a blunt indenter the plastic depth (d_p) must be replaced by an effective plastic depth (d_{eff}). This effective depth is the depth the indenter would penetrate for a given area if it were ideal and is given by the relationship, $d_{eff} = (PA/24.56)^{1/2}$. Thus, a plot of compliance versus d_{eff} has a slope proportional to 1/E, if the area/depth relationship is correct. By indenting materials of known modulus, the value of r can be adjusted until the slope of compliance versus $1/d_{eff}$ is what is should be. This method is relatively simple, can be performed on any sample at any time and avoids the problems of direct imaging.

Using both methods, the value of r was originally determined to be 20 nm. However, after four years of use the indenter has become blunter. Using the second method only, the value of r is presently 40 nm. Figure 5.6 shows the effect of using various values for the tip radius on hardness (a)

Fig. 5.5. High-resolution SEM micrographs of 20, 40 and 60 nm indentations (left) and an enlarged 20 nm indentation (right) in brass.

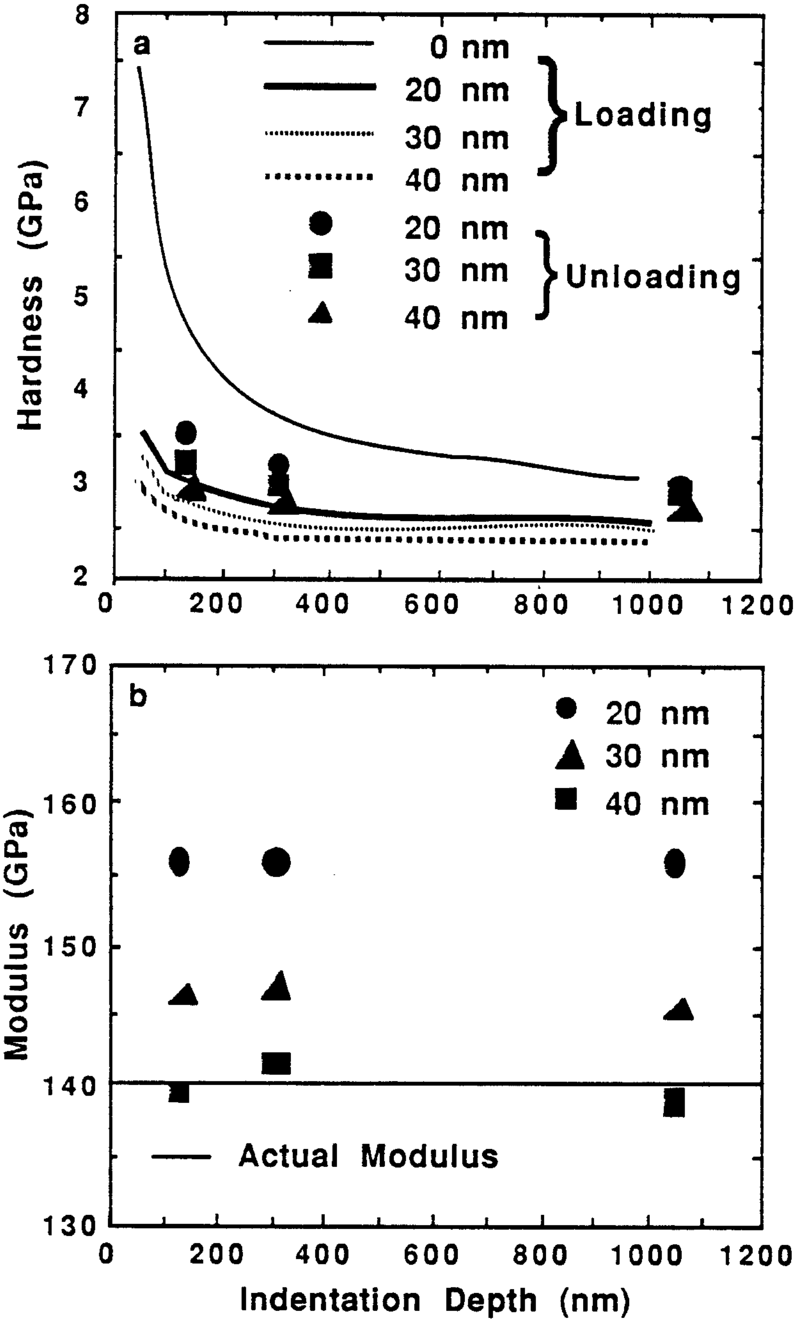

Fig. 5.6. Hardness (a) and Modulus (b) versus Indentation depth as a function of indenter tip radius.

and modulus (b). Using too small a radius results in modulus measurements being too high, and causes hardness to be higher and to rise much faster as load decreases. The reason for this blunting and the rate of deterioration of the indenter is unknown; however, the indentation of very hard, high modulus materials(eg. nitrides, carbides, diamond-ike carbon) will probably accelerate the process.

The way a sample is mounted for indentation changes the measured compliance (or stiffness) of the sample. Every time a sample is loaded into the Nanoindenter it is mounted slightly differently. As a result, the measured compliance of a given sample will be different each time it is mounted into the indenter. Compliances are additive and the calibration of the Nanoindenter already accounts for the compliance/stiffness of the machine and springs. While sample compliance is a function of the contact area, all other non-sample compliances are constant. Thus, extra non-sample related compliances shift the plot of sample compliance versus 1/deff up or down a given amount. Figure 5.7 are plots for solution-annealed and aged and cold-worked and aged Cu-Ni-Be that shows this shift resulting from different mountings. Non-sample compliance (Cc) has a load (L) dependent effect on the actual depth of indentation (d) given by, $d(L) = d_o(L) + Cc\ L$, where d_o is the total displacement of indenter. This extra compliance is given by the y-intercept of the compliance versus $1/d_{eff}$ curve and is known as the compliance correction. Figure 5.8 schematically shows how this added compliance effects the load-displacement curve. As result the uncorrected curve will yield incorrect loading hardnesses and by shifting the

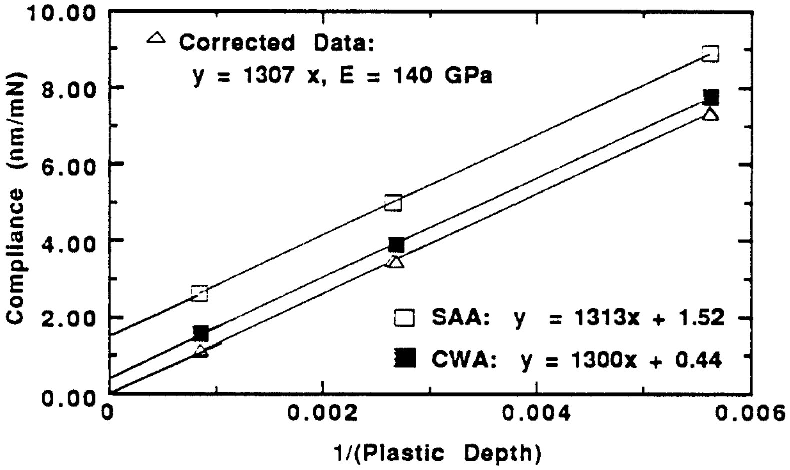

Fig. 5.7. Compliance vs. 1/plastic depth for cold-worked and aged (CWA) and solution-annealed and aged (SAA), corrected & uncorrected.

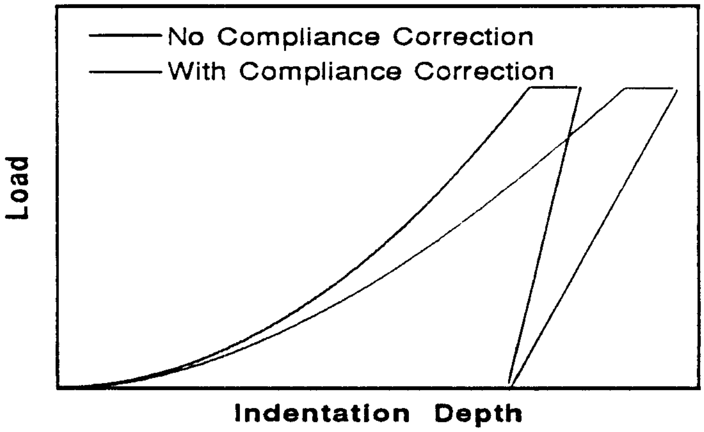

Fig. 5.8. Schematic of load vs. depth with/without compliance correction.

slope of the unloading curve the modulus value determined from that slope will be wrong. Using the uncorrected curves from the two samples shown in Fig. 5.7, modulus values were calculated and are shown in Fig. 5.9. Without knowing the proper compliance correction it is impossible to compare two separate samples. In order to compare different samples, at least a few indentations to at least two depths are required to determine the value of the compliance correction.

V. D. 4. Indentation of Irradiated Samples

For the Cu-Ni-Be alloy, indentations were made both normal to the irradiated surface (on as-irradiated specimens) and parallel to it (on cross-sectional specimens). Only cross-sectioned samples of the Ni-Cu alloys and the Cu-Al20 alloy were made. A schematic of these types of indentations is shown is Fig. 5.10. The normal indentations were made at a constant displacement rate of 5 nm/s in both irradiated and unirradiated areas to depths of 500 and 1500 nm before unloading. For parallel indentations a line of indentations 5 μm apart were made at an angle of ~5.7° relative to the interface between the irradiated foil and the plating, to a depth of 150 nm, at a constant displacement rate of 3 nm/s. Figure 5.11 shows a line of indentations in a cross-sectioned sample.

V. D. 5 TEM

Microstructural changes in only the Cu-Ni-Be samples were examined. The analysis was performed using a JEOL TEMSCAN-200CX electron microscope operated at 200 kV. CTEM was performed using

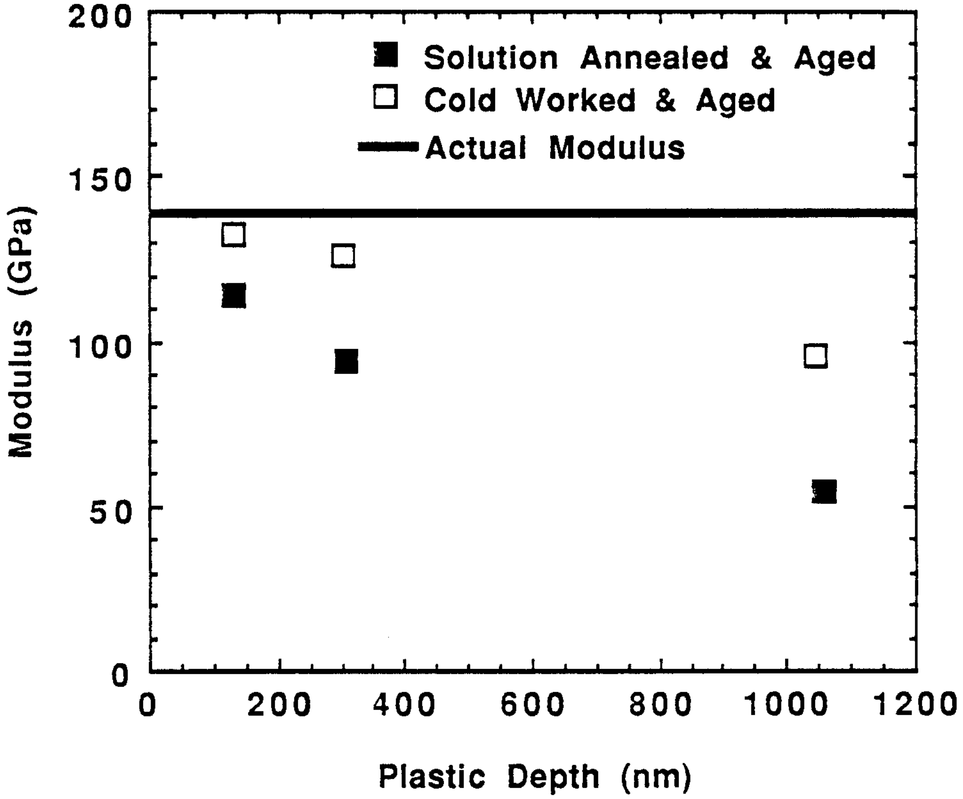

Fig. 5.9. Uncorrected Elastic Madulus as function of indentation depth for Cu-Ni-Be.

INDENTATION PROCEDURE FOR ION-IRRADIATED MATERIALS:

INDENTATIONS NORMAL TO THE IRRADIATED SURFACE AND CROSS-SECTION INDENTATIONS NORMAL TO THE INCIDENT ION BEAM

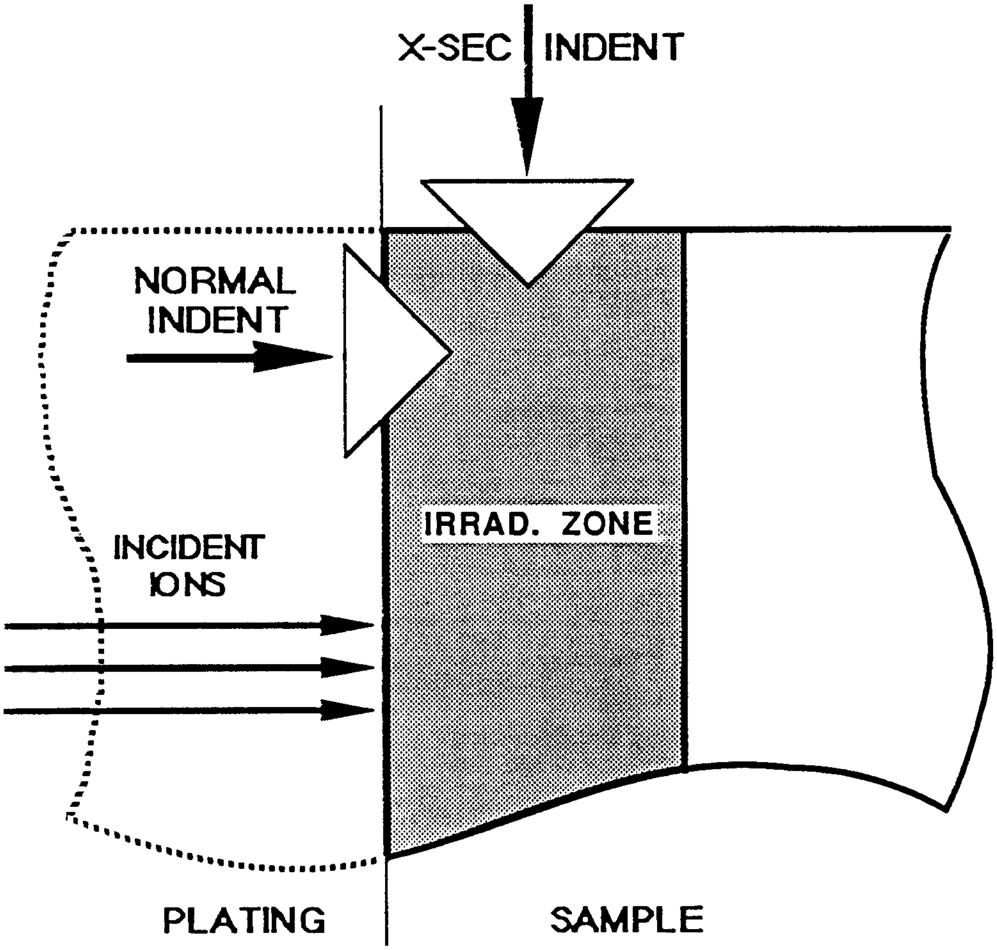

Fig. 5.10. Indentation procedure schematic for ion irradiated materials

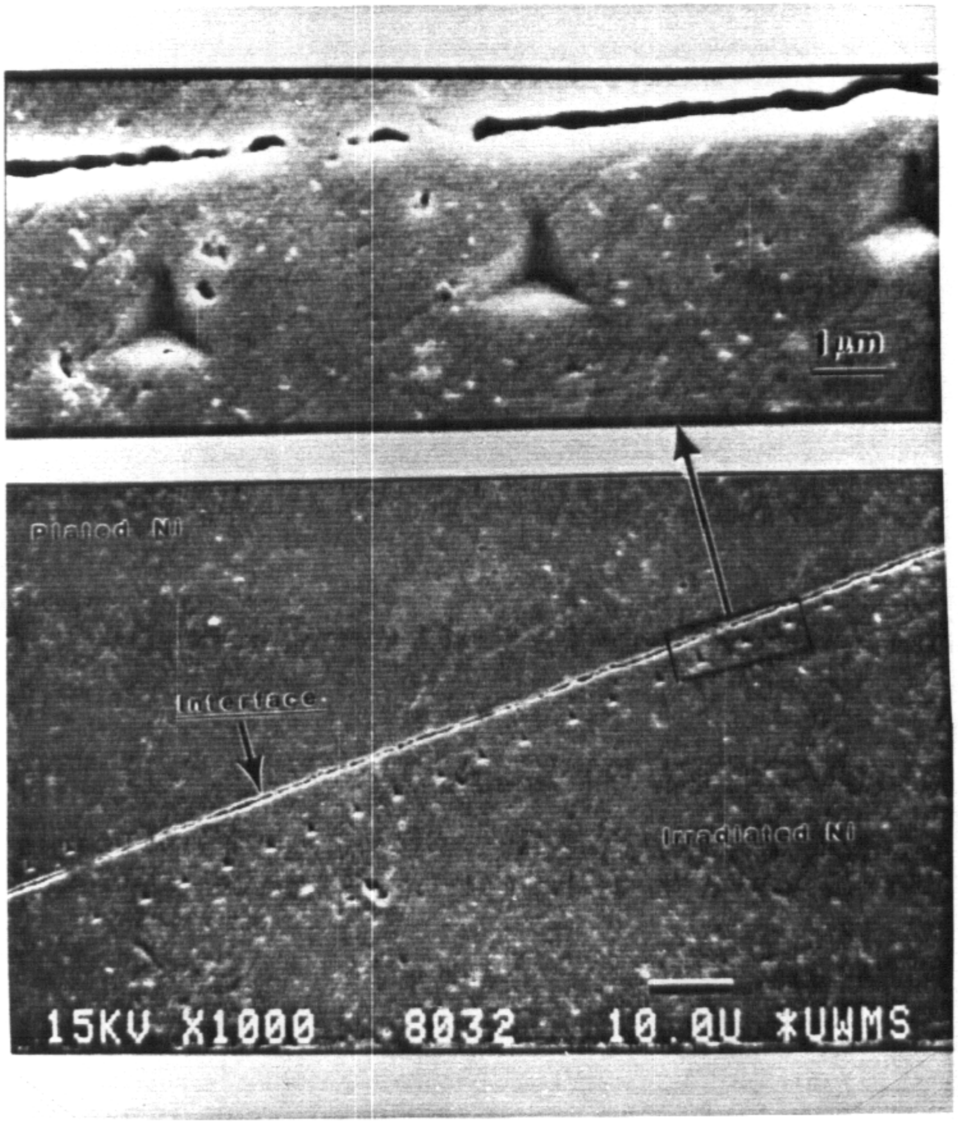

Fig. 5.11. SEM micrographs of indentations made is cross-sectioned sample.

techniques outlined by Edington [18]. The main emphasis was on the changes in the precipitate morphology. Coarsening of the G.P. zones was examined by observing the growth of the zones imaged in dark-field with the <100> relrods (streaks),the disappearance of the relrods in the diffraction pattern, and the appearance of equilibrium NiBe precipitates.

CHAPTER V

REFERENCES

1. L.-M. Wang, Ph. D. Thesis, Materials Science Program, University of Wisconsin-Madison (1988).
2. A. Guha, Brush Wellman, Inc., Private communication (1984).
3. S. Rosenwasser, Inesco, Inc., Private communication (1984).
4. Alloy Digest, Filing Code CU-454 (1983).
5. Certification of Material Conformance, Brush Wellman Inc., Elmore, Ohio 43416, May 13, 1981 (received 1984).
6. Alloy Digest, Filing Code CU-546 (1982).
7. R.J. Livak,T.G. Zocco and J.C. Kennedy, ADIP Semiannual Progress Report, DOE/ER-0045/14 (Mar. 1985) 152.
8. J.A. Spitznagel, et.al., Nucl. Instr. and Meth B, 16 (1986) 279.
9. H.V. Smith and R.G. Lott, Nucl. Instr. Methods 143 (1977) 125.
10. J.H. Billen and H.T. Richards, Proc. of Symp. of Northeastern Accelerator Personnel, CONF-781051, Oak Ridge, TN (Oct. 1978) 137.
11. J.H. Billen, IEEE Trans. Nuclear Science, N5-28 (1981) 1535.
12. R.W. Knoll, Ph.D. Thesis, Nuclear Engineering Department, University of Wisconsin-Madison (1981).
13. S.J. Zinkle and R.L. Sindelar, Nucl. Instr. and Meth. B, 16 (1986) 154.
14. J.B. Pethica, R. Hutchings and W.C. Oliver, Phil. Mag. A, 48 (1883) 593.

15. W.C. Oliver, R. Hutchings and J.B. Pethica, in **Microindentation Techniques in Materials Science and Engineering**, ASTM STP 889, P.J. Alan and B.R. Lawn (Eds), ASTM, Philadelphia (1985) 90.

16. M.F. Doerner and W.D. Nix. J. Mater. Res., 1 (1986) 601.

17. J.L. Loubet, J.M. Georges, O. Marchesini and G. Meille, J Tribology, 106 (1984) 43.

18. J.W. Edington, **Practical Electron Microscopy in Materials Science**, Monograph (Phillips Technical Library, 1974).

CHAPTER VI

RESULTS

VI. A. Ni-Cu Alloys

Figure 6.1 shows examples of the microstructures of irradiated Ni-10% Cu (Fig. 6.1 a) and Ni-50% Cu (Fig. 6.1 b) in cross-section*. Both compositions display a high dislocation loop density in the irradiated region and are virtually defect free beyond that region. Enlargements of the irradiated region in Ni-10% Cu and Ni-50% Cu are shown in Figs. 6.2 a and 6.2 b, respectively. Table 6.1 shows the dislocation loop density and average diameter, and Fig. 6.3 shows the distribution of loop sizes. It can be seen that Ni-50% Cu has a very high density of small dislocation loops, while Ni-10% Cu has a lower density with a large range of loop sizes. Very few voids were seen in Ni-10% Cu [1], and the volume fraction was so small that they have been ignored for the purpose of this study.

Although the two compositions start out with approximately the same hardness (Table 5.1), they have very different radiation hardening characteristics (Fig. 6.4). All Ni-50% Cu samples display about a 55% increase in hardness in the irradiated region. The 5 and 10 dpa Ni-10% Cu samples have about a 25 to 30% increase in hardness, while the 25 dpa

---

* The author wishes to thank Dr. Lu-Min Wang for his assistance in performing the microscopy for the Ni-Cu alloys.

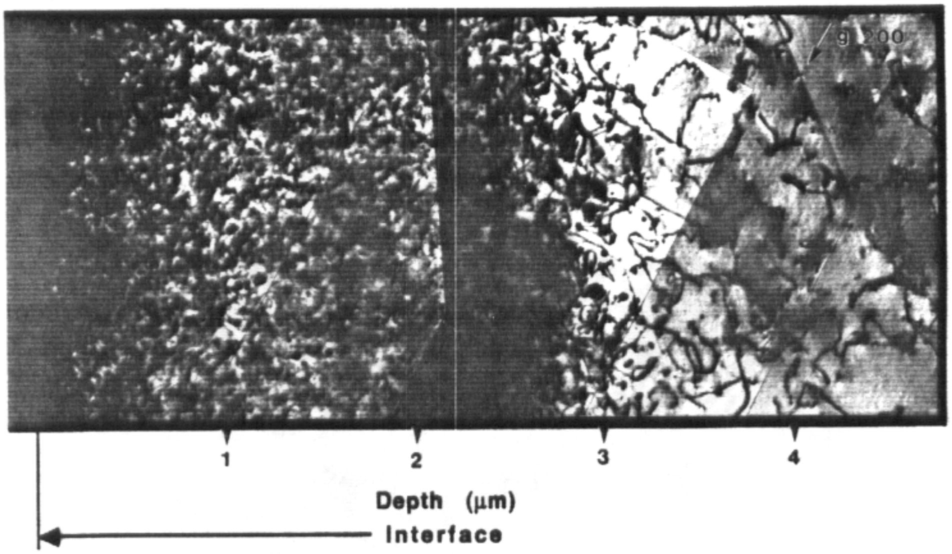

ENTIRE ION DAMAGED REGION IN 14 MeV Ni ION IRRADIATED Ni-10Cu
(Peak damage level: 40 dpa, 485°C, 100 appm Oxygen preinjection)

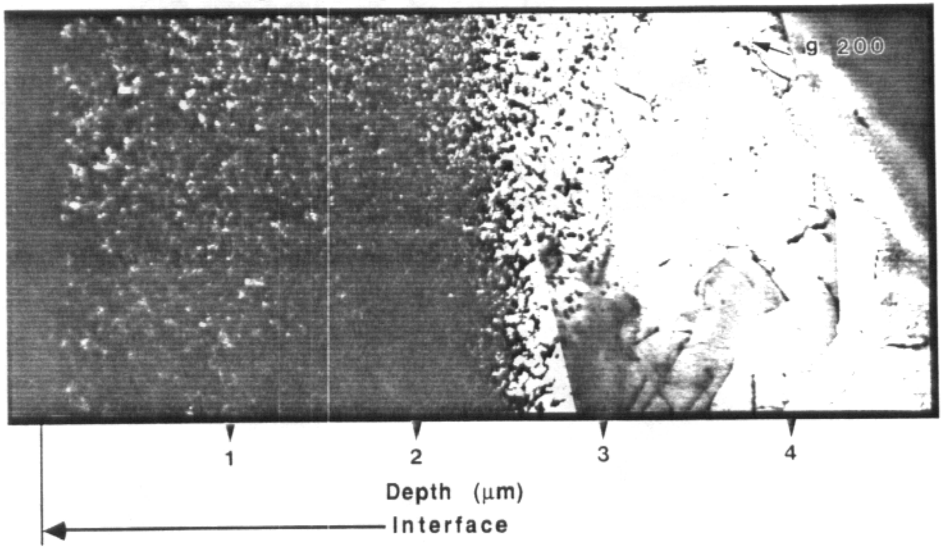

ENTIRE ION DAMAGED REGION IN 14 MeV Ni ION IRRADIATED Ni-50Cu
(Peak damage level: 40 dpa, 425°C, 100 appm Oxygen preinjection)

Fig. 6.1. TEM micrographs of Ni-10% Cu (a) and Ni-50% Cu (b) irradiated to 10 dpa at 1 μm at 0.45 Tm in cross-section showing the entire irradiated region.

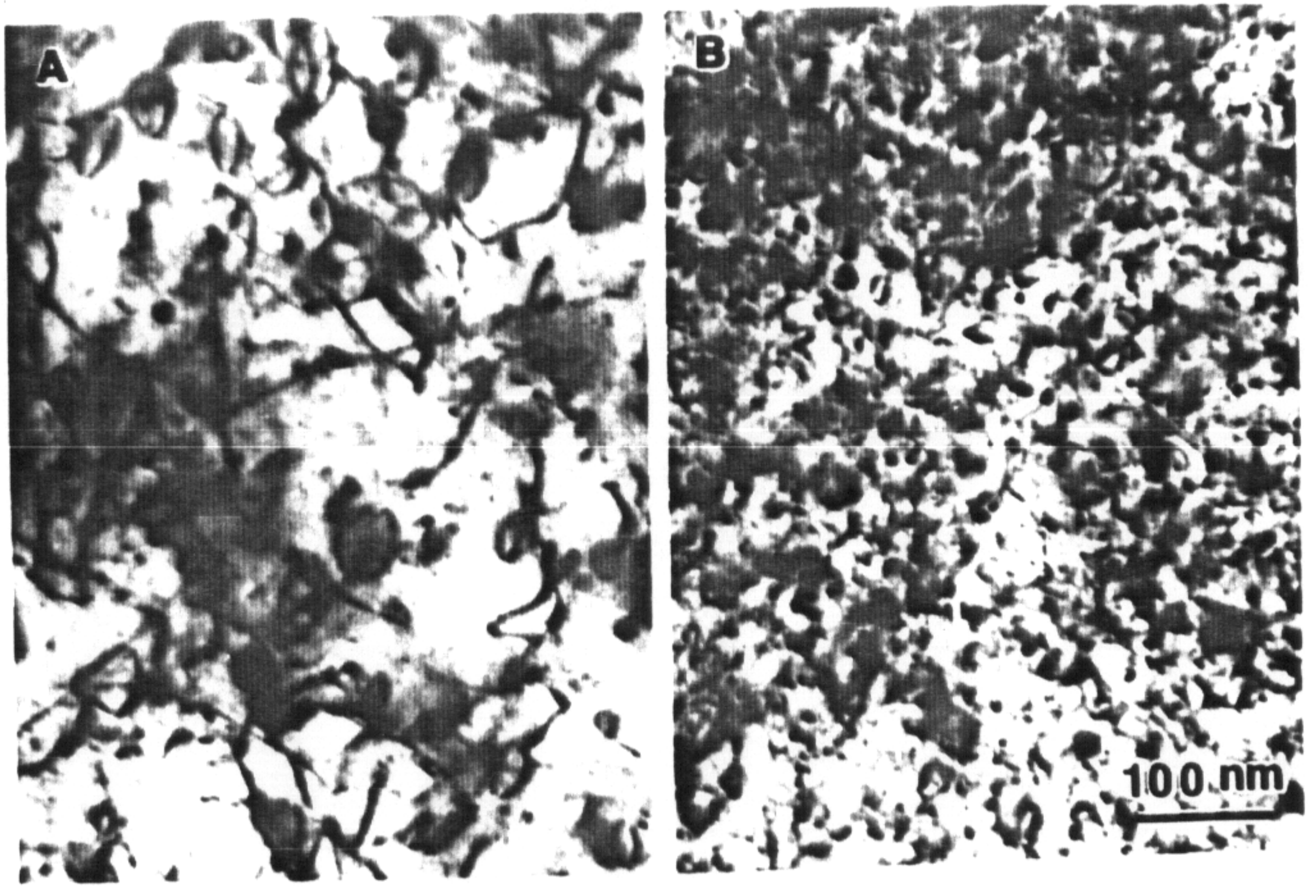

Fig. 5—Enlargements of the irradiated regions from Fig. 4 for Ni-10% Cu (a) and Ni-50% Cu (b).

Plantz

Fig 6.2. Enlargements from the irradiated regions from Fig. 6.1 for Ni-10% Cu (a) and Ni-50% Cu (b).

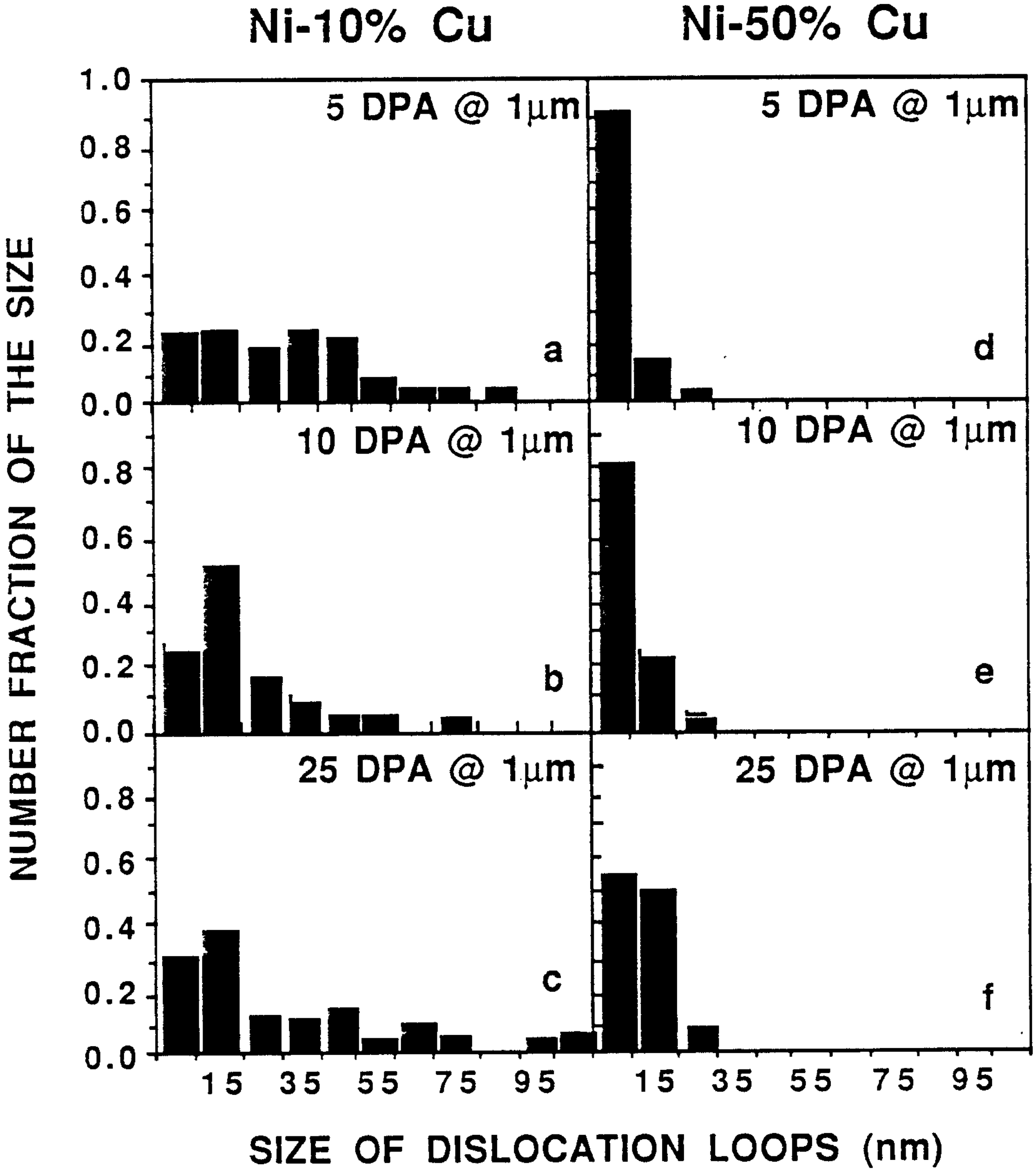

Fig. 6.3. Distribution of dislocation loops in irradiated Ni-10% Cu (a-c) and Ni-50% Cu (d-f) for different fluences.

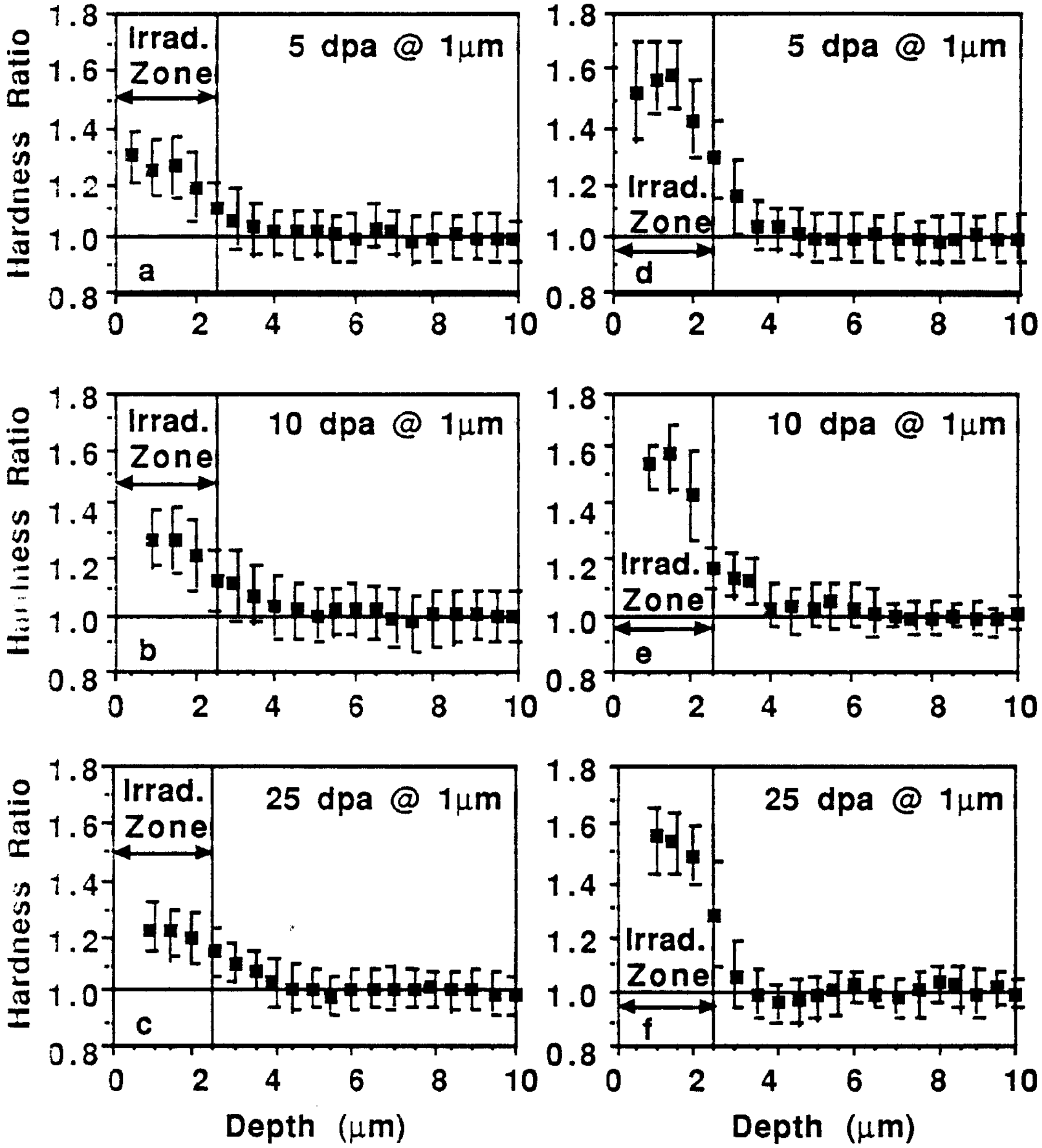

Fig. 6.4. Ratio of hardness to average unirradiated hardness versus depth in Ni-10% Cu (a-c) and Ni-50% Cu (d-f) irradiated at 0.45 Tm To various fluences.

Table 6.1. Dislocation Loop Characteristics for Irradiated Ni-Cu

Composition	Irradiation Temperature	Dpa (1 μm)	Dislocation Loop Density (m^{-3})	Average Loop Diameter (nm)
Ni-10% Cu	485°C	5	1×10^{21}	29
		10	1×10^{21}	19
		25	1×10^{21}	25
Ni-50% Cu	425°C	5	7×10^{21}	6
		10	5×10^{21}	7
		25	5×10^{21}	10

sample has only about a 20% increase. All hardness data has about a 10% standard deviation except near either end of the irradiated region where the scatter is usually larger.

VI. B. Copper Alloys

VI. B. 1. Cu-Ni-Be

Figures 6.5 and 6.6 show optical micrographs of the unirradiated alloy in the cold-worked and aged, and solution-annealed and aged conditions, respectively. The grains of the cold-worked and aged alloy tend to be elongated and about 25 to 50 μm across, while the grains of the solution-

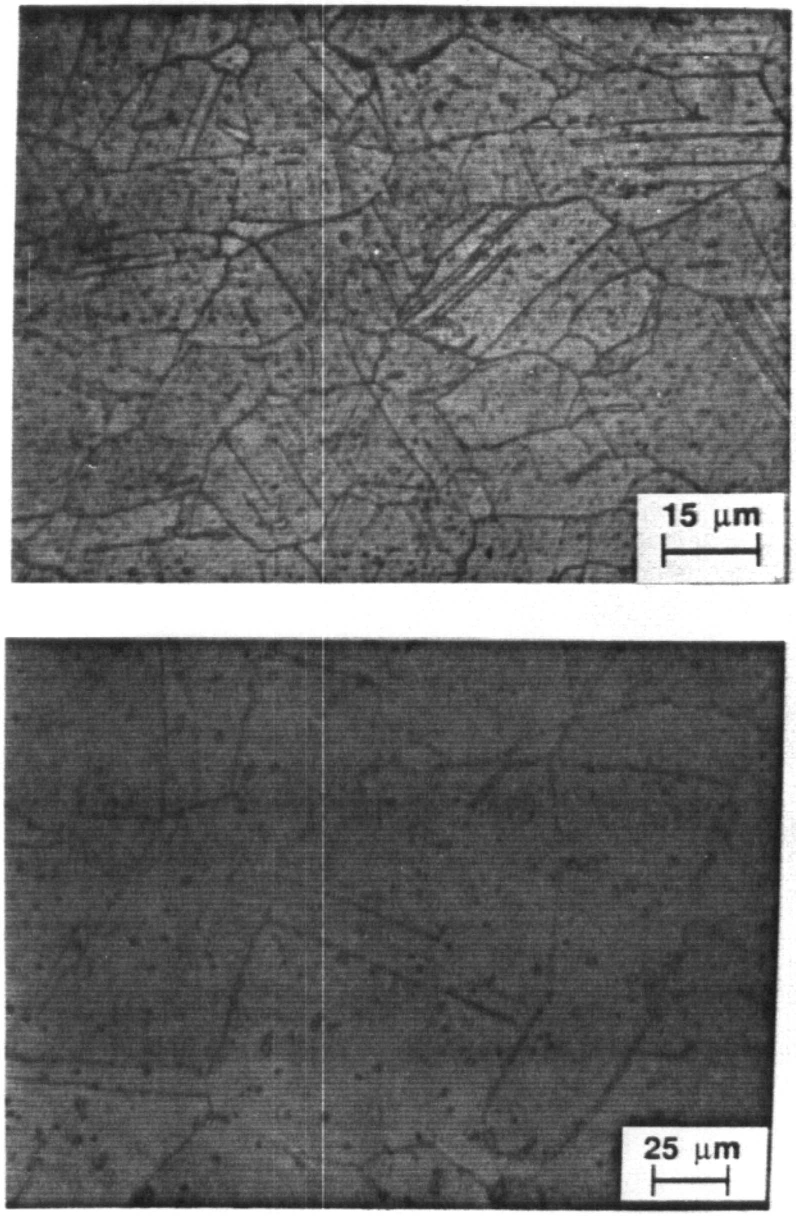

Optical microstructure of cold-worked & aged Cu-Be-Ni

Fig. 6.5. Optical micrographs of cold-worked and aged Cu-Ni-Be.

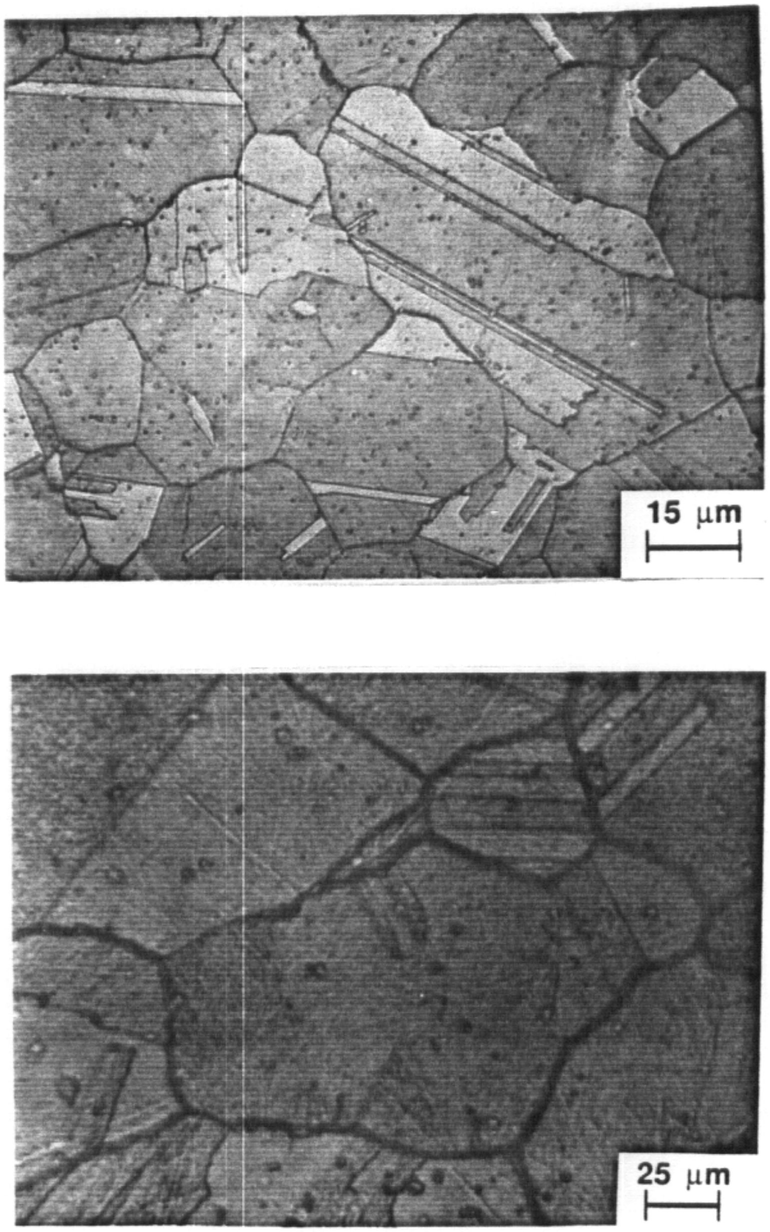

Optical microstructure of solution annealed & aged Cu-Be-Ni

Fig. 6.6. Optical micrographs of solution-annealed and aged Cu-Ni-Be.

annealed and aged alloy tend to be equi-axed and a few hundred microns across. Bright and dark field TEM micrographs and diffraction patterns of the two thermo-mechanical treatments are shown in Figs. 6.7 and 6.8. Both alloys contain a very high density of G.P Zones, which causes the streak or relrod in the <002> diffraction spots. The strain fields of the G.P zones makes it nearly impossible to see dislocation even the the cold-worked and aged condition.

Table 6.2 shows the initial mechanical properties of the samples, the yield strength have been measured prior to receiving the alloy [2]. The modulus measurements represent a comparison of values found in the literature using conventional testing methods [3] and values measured on the MPM, which have about a 10% standard deviation. The MPM hardness measurements were obtained with loads of about 10 g. The Vickers microhardness and MPM harness values have comparable standard deviations of less than 5%.

Vickers microhardness measurements of the alloy in both starting conditions, following further aging at 300 and 400°C for 10 to 1000 hours, showed no appreciable change in hardness. Figures 6.9 a and b show diffraction patterns and dark field TEM micrographs of the cold-worked and aged, and solution-annealed and aged samples, respectively, following further aging at 400°C for 1000 hours. The solution-annealed and aged sample shows no change in microstructure. However, the cold-worked and aged sample shows an increase in intensity or bunching of the <002>

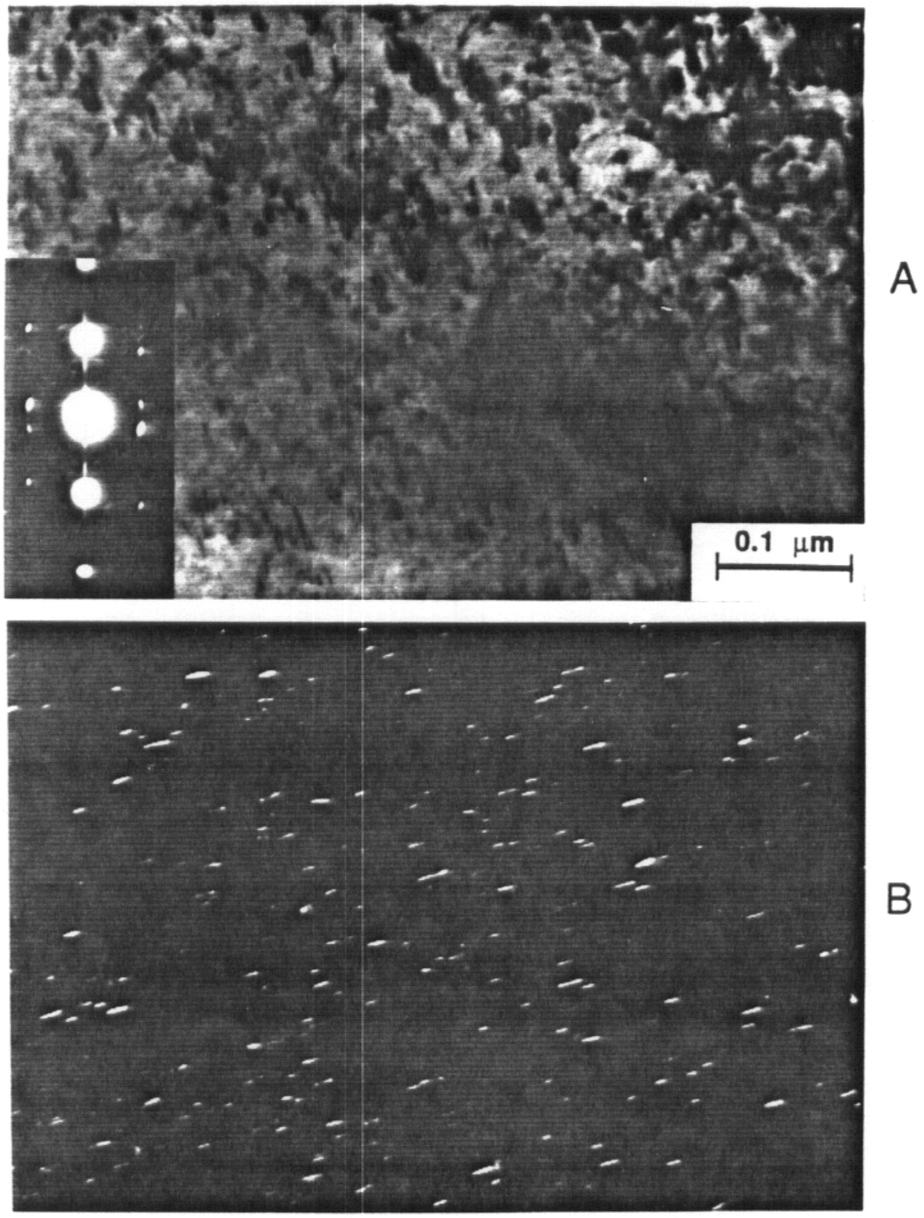

Fig. 6.7. Bright field TEM micrograph and SAD pattern (a) and dark field TEM micrograph imaged with <002> streak (b) showing G. P. zones in cold-worked and aged Cu-Ni-Be.

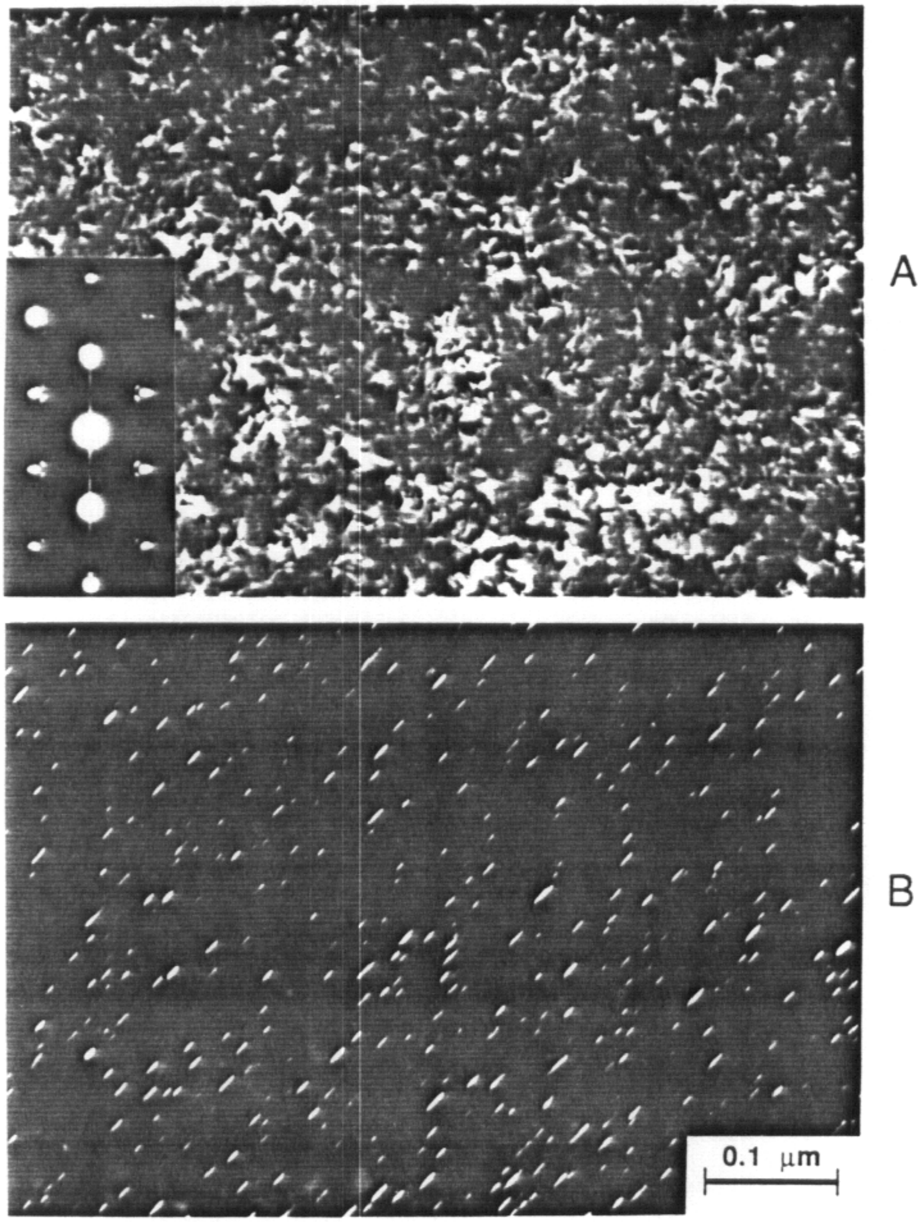

Fig. 6.8. Bright field TEM micrograph and SAD pattern (a) and dark field TEM micrograph imaged with <002> streak (b) showing G. P. zones in solution-annealed and aged Cu-Ni-Be.

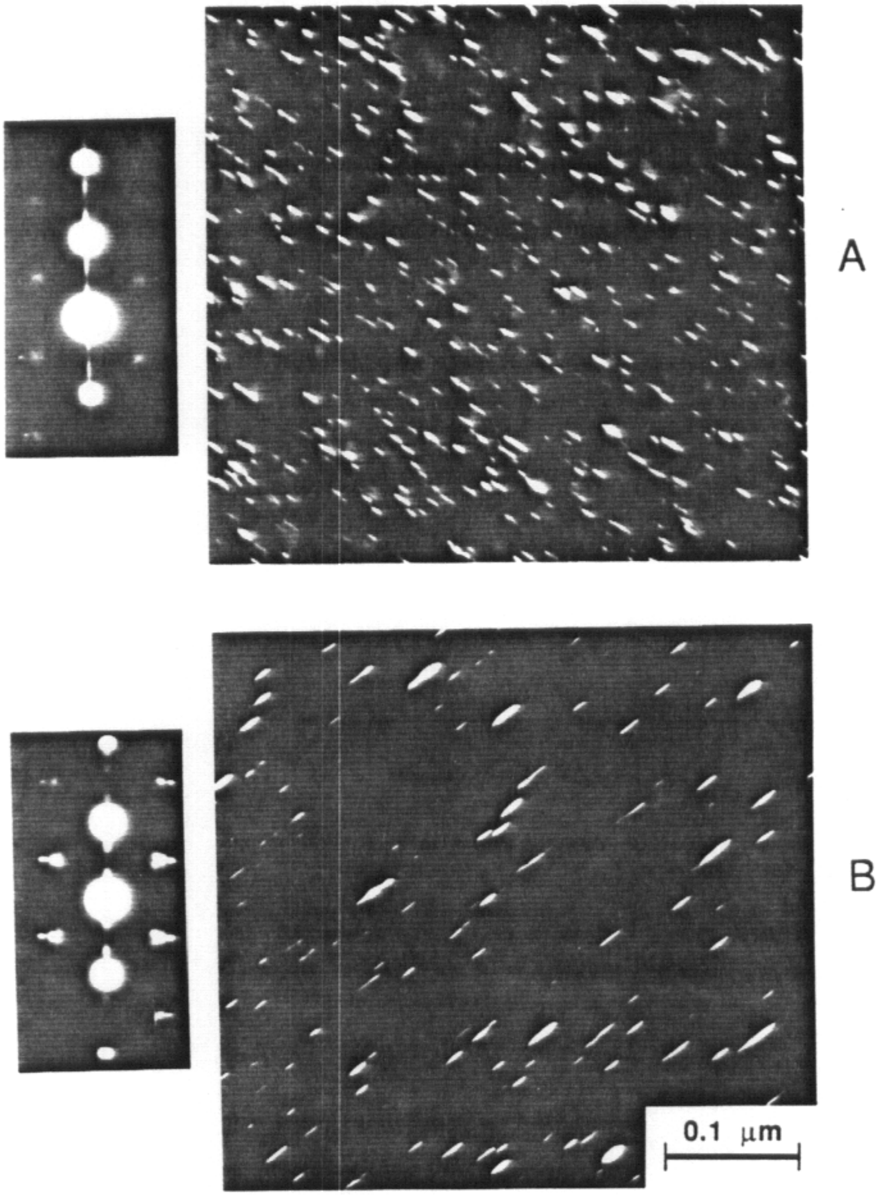

Fig. 6.9. SAD patterns and dark field TEM micrographs of G.P. zones in cold-worked and aged (a) and solution-annealed and aged (b) Cu-Ni-Be after further aging at 400°C for 1000 hours.

Table 6.2. Initial Mechanical Properties of Cu-Ni-Be in GPa

Thermo-mechanical	Yield	Youngs Modulus		VHN	MPM
Treatment	Strength	Standard	MPM	(200g)	(1500 nm)
Cold-Worked and Aged	0.78	135	145	2.20	2.40
Solution-Annealed and Aged	–	135	140	2.35	2.70

streaks at 2/3 <002> position and the precipitates in dark-field seem to be slightly larger, indicating some coarsening of the precipitates.

Figures 6.10 and 6.11 show the microstructures, at a depth of 1 to 2 μm from the irradiated surface, of the solution-annealed and aged alloy irradiated at 300 and 400°C, respectively. There is no apparent change in the microstructure due to irradiation. Bright field micrographs and a diffraction pattern of irradiated (about 1 to 2 μm deep) and unirradiated regions in the same grain in the solution-annealed and aged alloy irradiated at 500°C are shown in Figs. 6.12 a and b, respectively. Dark field micrographs of the corresponding areas are shown in Fig 6.13. The diffraction pattern shows a distinct diffraction spot at the 2/3 <002> position. Distinct platelets can be seen in bright field. No significant differences can be seen between the irradiated and unirradiated regions

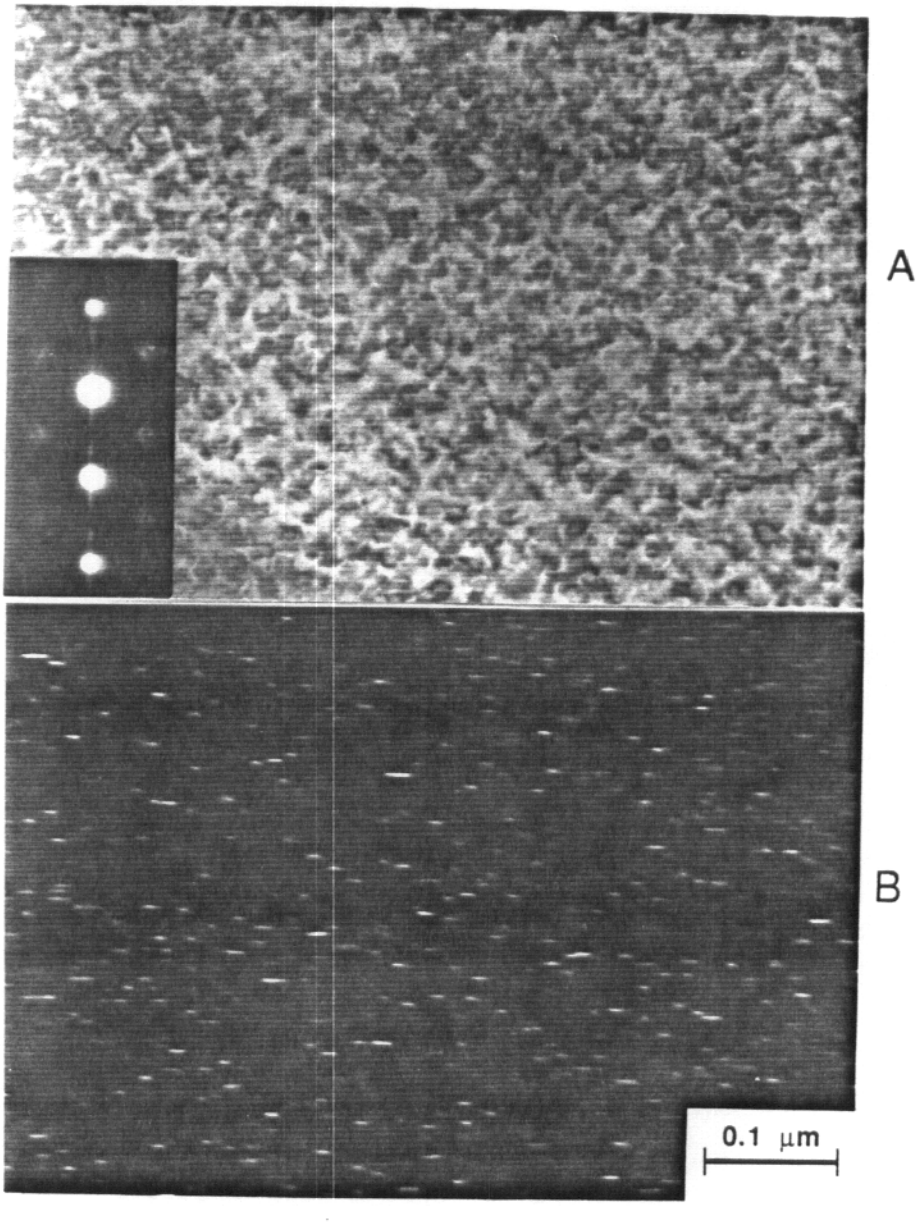

Fig. 6.10. SAD pattern and bright field (a) and dark field (b) TEM micrographs of G. P. zones in irradiated solution-annealed and aged Cu-Ni-Be following irradiation at 300°C.

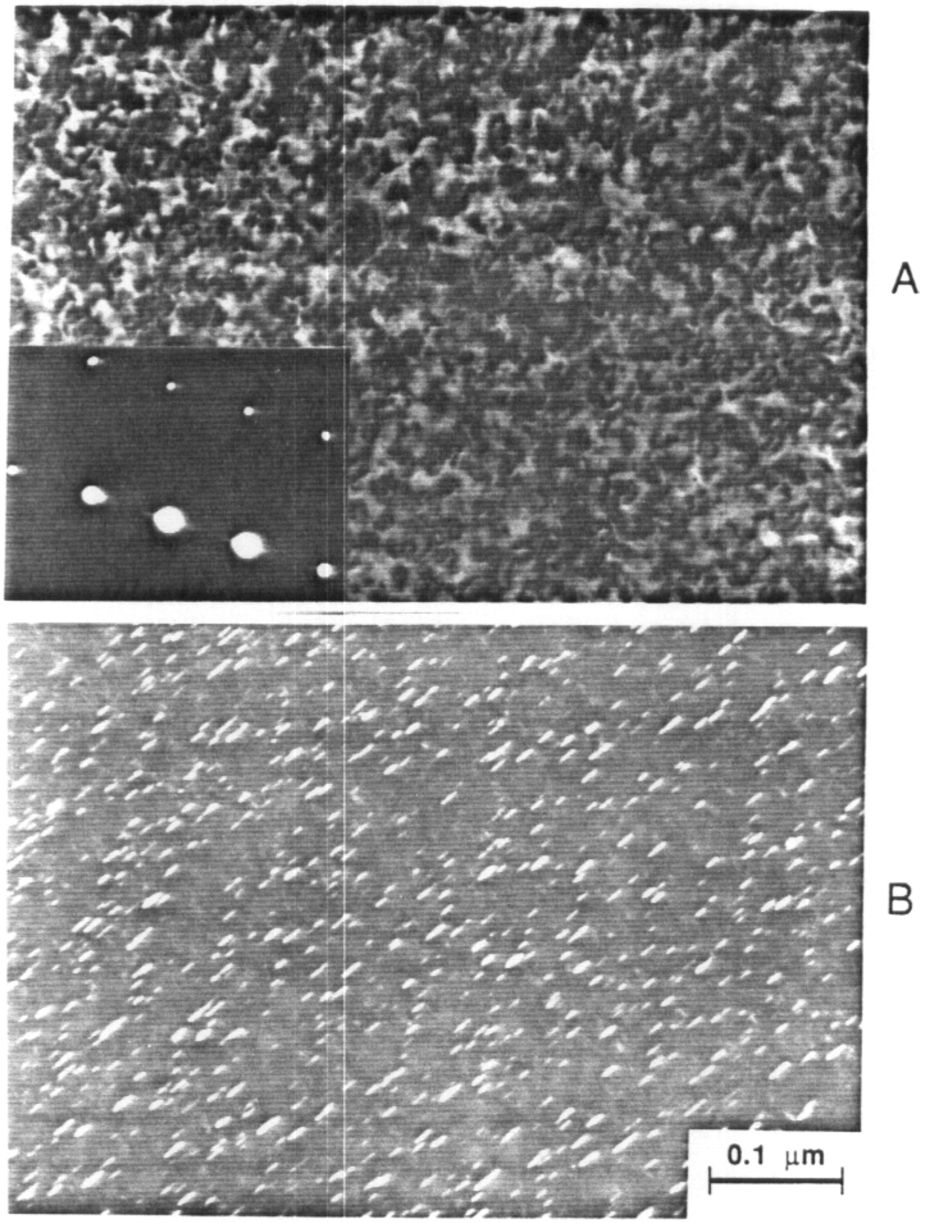

Fig. 6.11. SAD pattern and bright field (a) and dark field (b) TEM micrographs of G. P. zones in irradiated solution-annealed and aged Cu-Ni-Be following irradiation at 400°C.

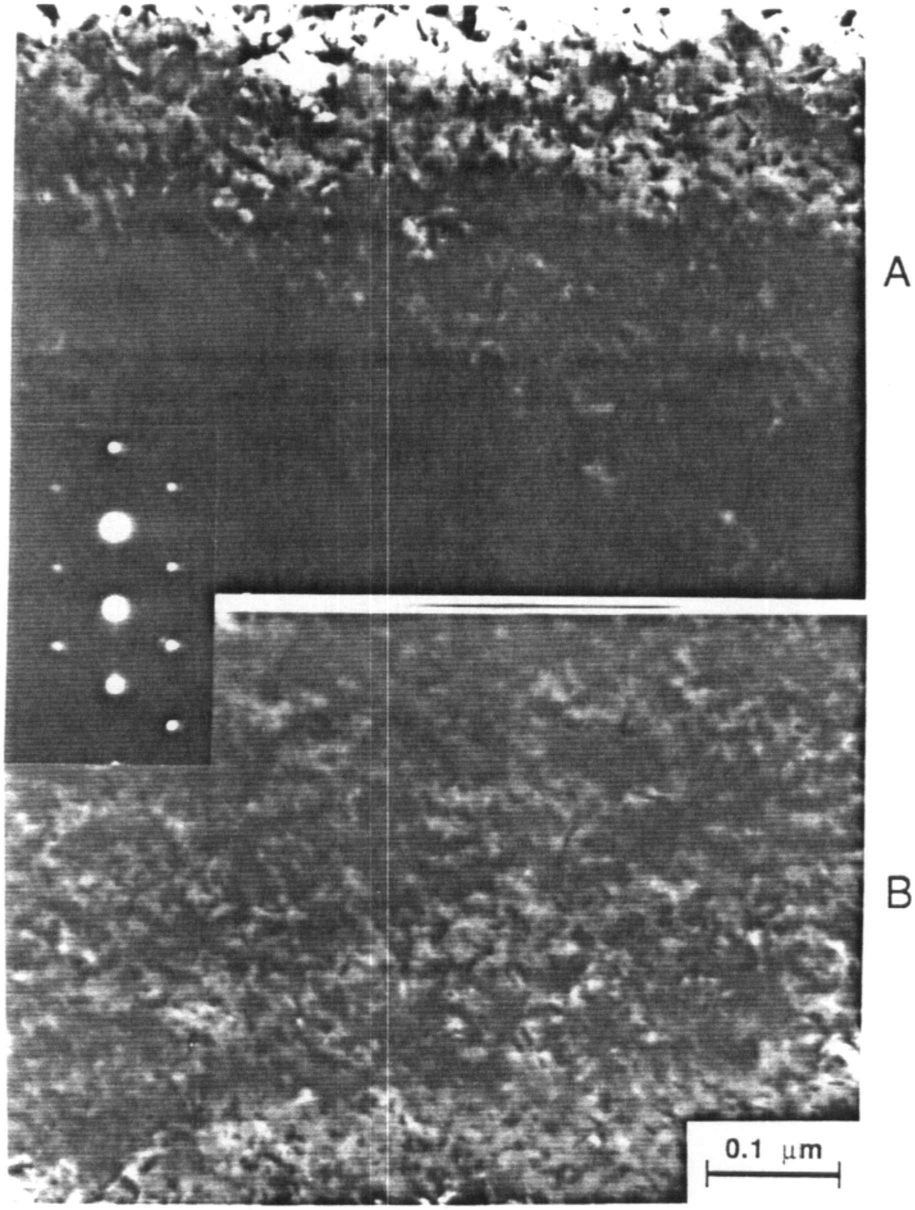

Fig. 6.12. SAD pattern and bright field TEM micrographs of coarsened precipitates in irradiated (a) and unirradiated (b) solution-annealed and aged Cu-Ni-Be following irradiation at 500°C.

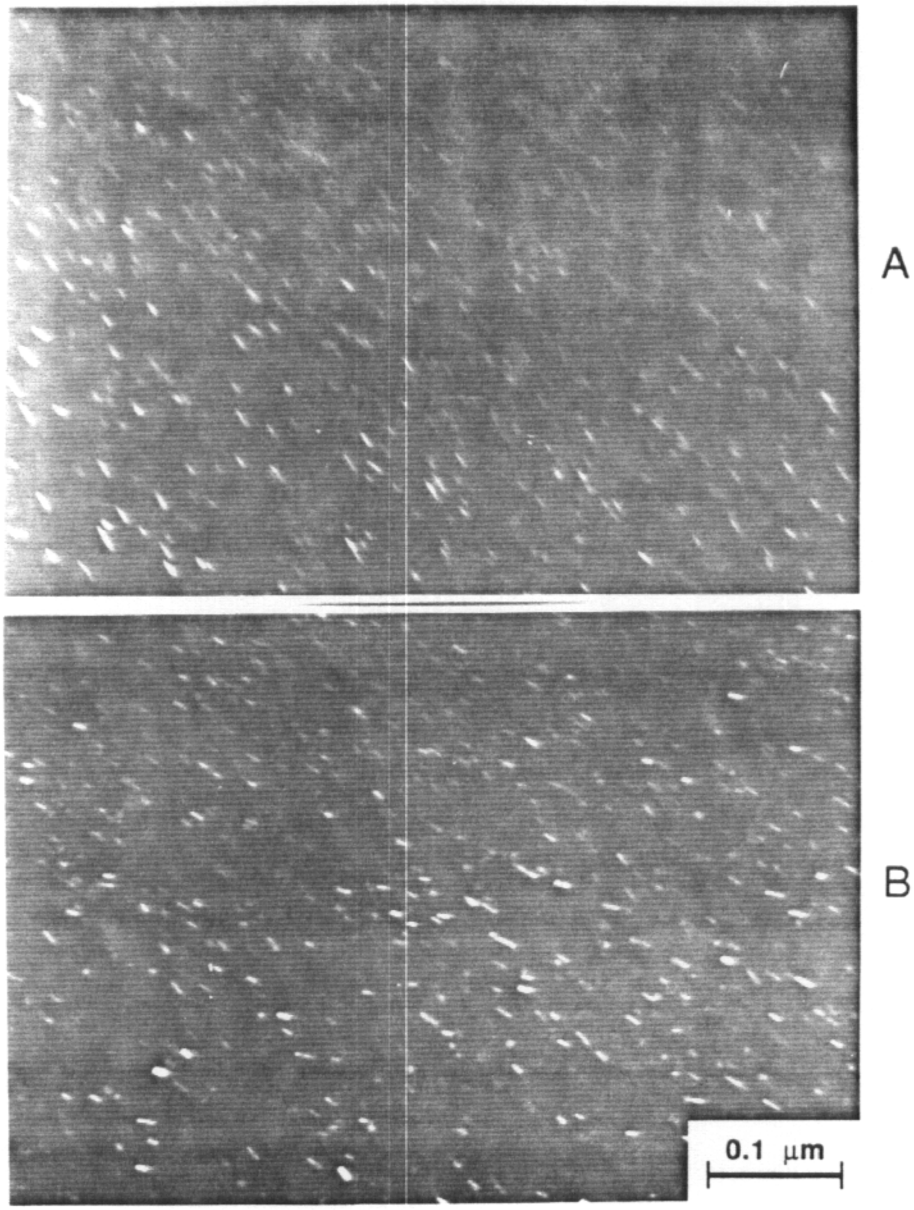

Fig. 6.13. Dark field TEM micrographs of the irradiated (a) and unirradiated (b) regions from Fig. 6.12.

Figure 6.14 a and b show bright field micrographs and diffraction patterns for irradiated (about 1 to 2 µm deep) and unirradiated regions, respectively, for the cold-worked and aged alloy irradiated at 400°C. Figures. 6.15 a and b are the respective dark field micrographs. A slight amount of bunching of the <002> streak can be seen in the unirradiated diffraction pattern, otherwise the microstructure looks essentially the same as the starting condition. A distinct diffraction spot at the 2/3 <002> position is starting to form in the irradiated diffraction pattern and distinct platelets can be seen in bright field. Bright field micrographs and diffraction patterns of an irradiated region and an unirradiated region for the cold-worked and aged alloy irradiated at 500°C are shown in Figs 6.16 a and b respectively and Fig 6.17 is the associated dark field micrographs. Distinct diffraction spots can be seen at 2/3 <002> in the diffraction pattern and platelets are visible in bright field in both the irradiated and unirradiated regions. Some precipitates with strain fields can still be seen in the unirradiated region, but they are completely absent in the irradiated region. From the dark field micrographs it is evident that the precipitates are much larger and less dense than any other thermal or irradiation condition.

Figure 6.18 shows an optical micrograph of the solution-annealed and aged (right) and cold-worked and aged alloys following irradiation at 500°C in cross-section (the plating is to the right for both samples). A line of indentations can be seen going across the interface in both samples. The cold-worked and aged sample shows a large number of micron size

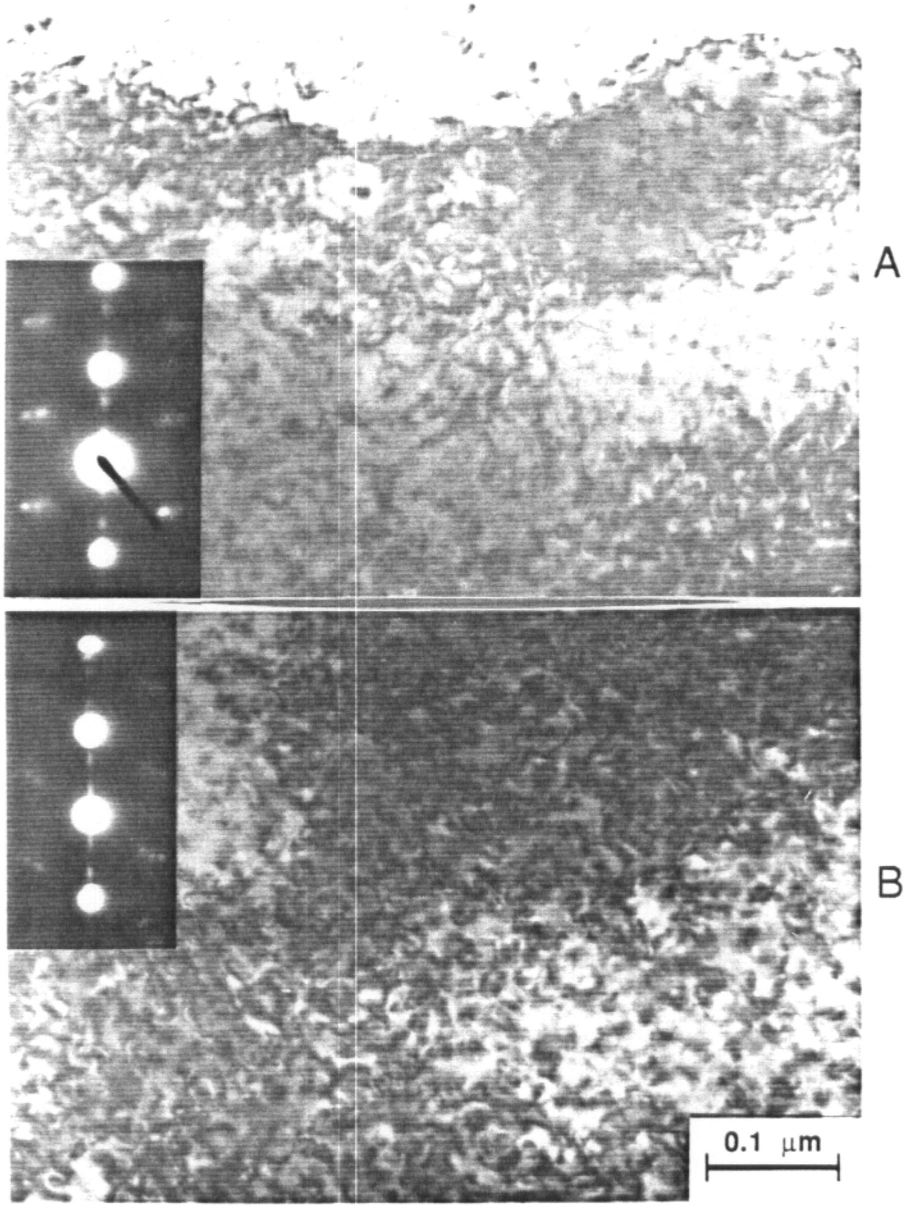

Fig. 6.14. SAD pattern and bright field TEM micrographs of coarsened precipitates and G.P zones in irradiated (a) and unirradiated (b) Cold-worked and aged Cu-Ni-Be following irradiation at 400°C.

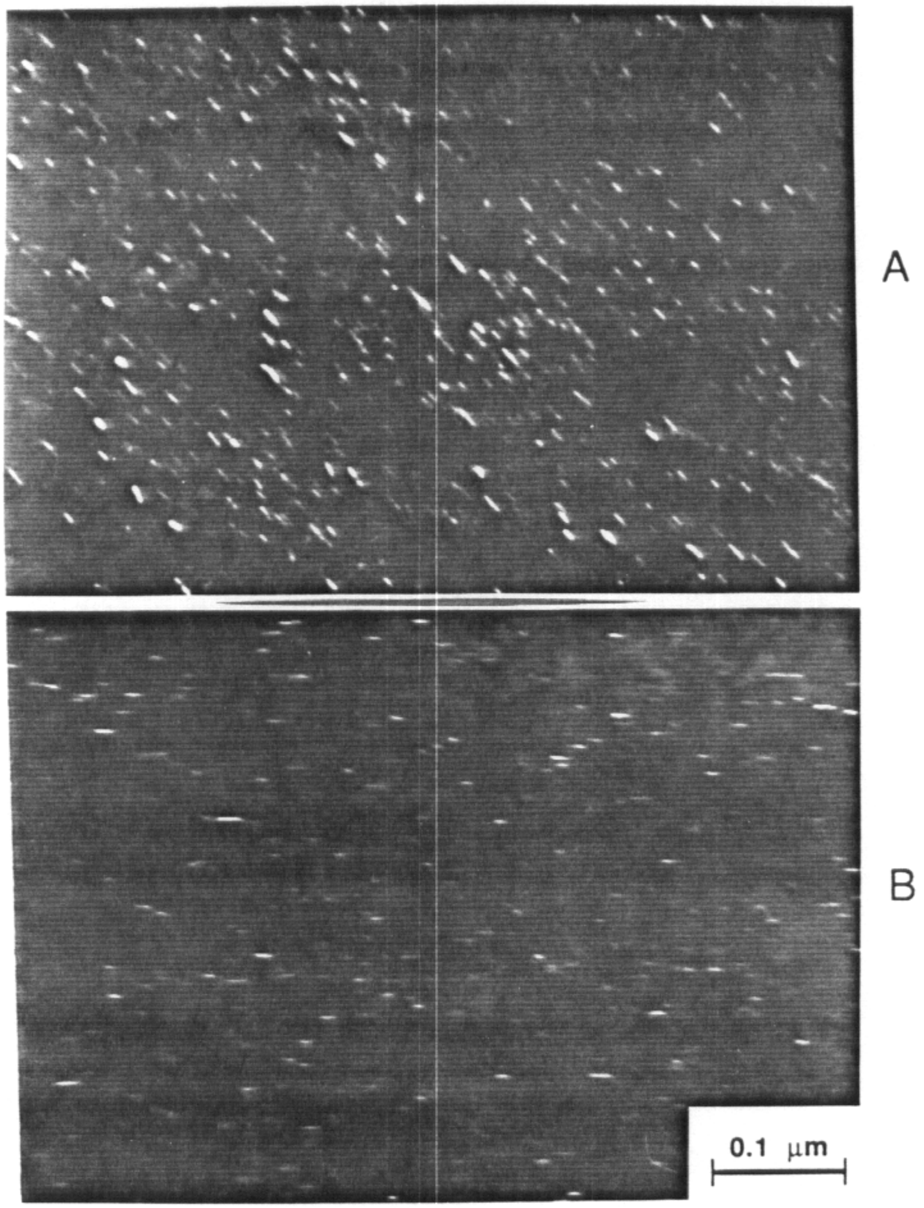

Fig. 6.15. Dark field TEM micrographs of the irradiated (a) and unirradiated (b) regions from Fig. 6.14.

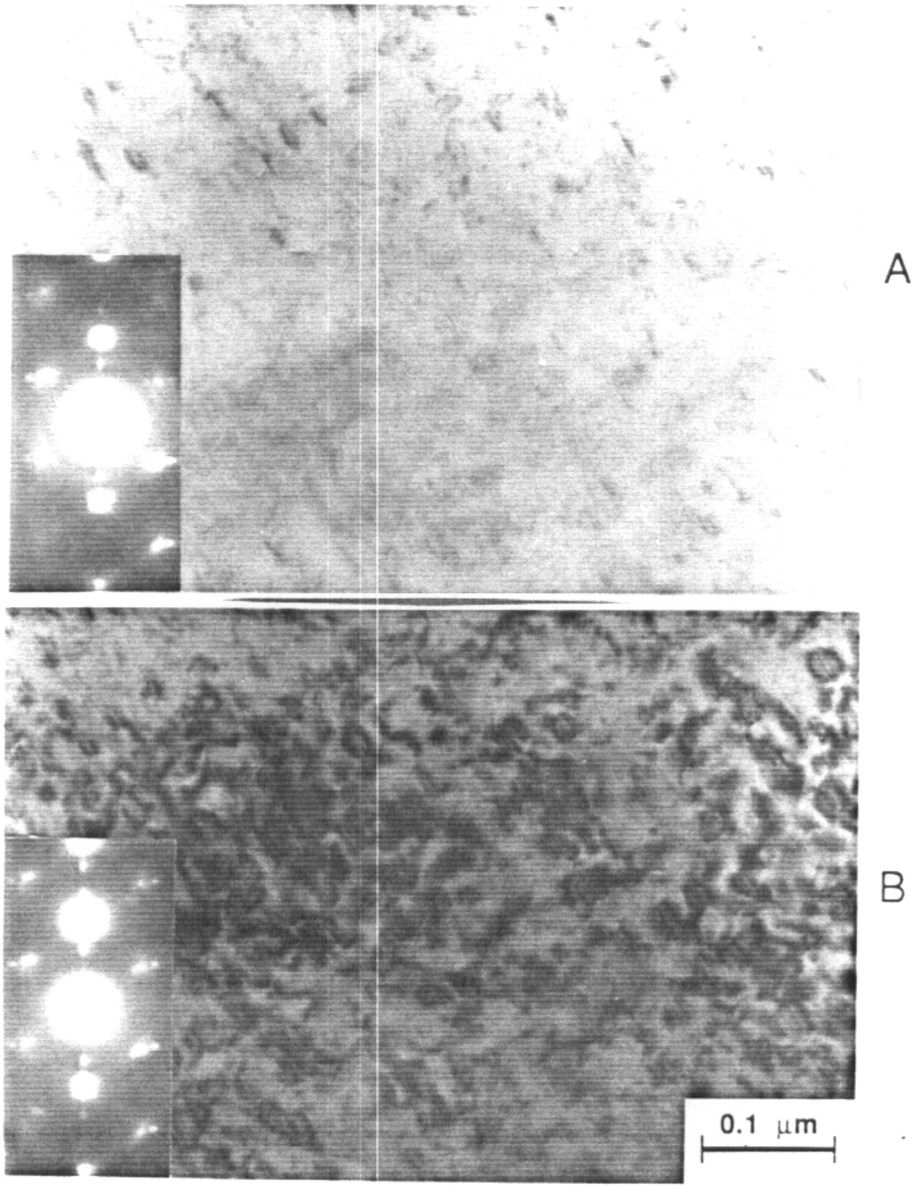

Fig. 6.16. SAD pattern and bright field TEM micrographs of coarsened precipitates in irradiated (a) and unirradiated (b) Cold-worked and aged Cu-Ni-Be following irradiation at 500°C.

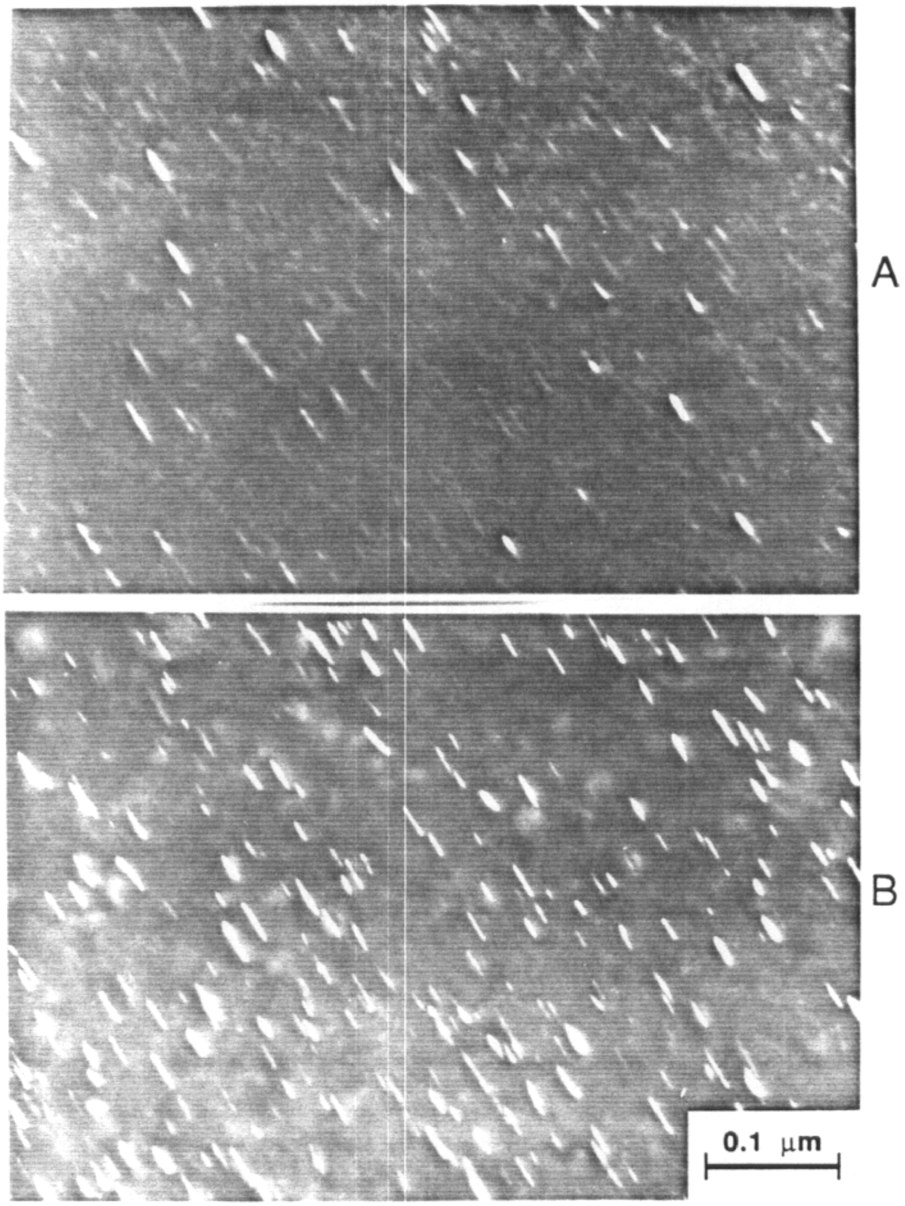

Fig. 6.17. Dark field TEM micrographs of the irradiated (a) and unirradiated (b) regions from Fig. 6.16.

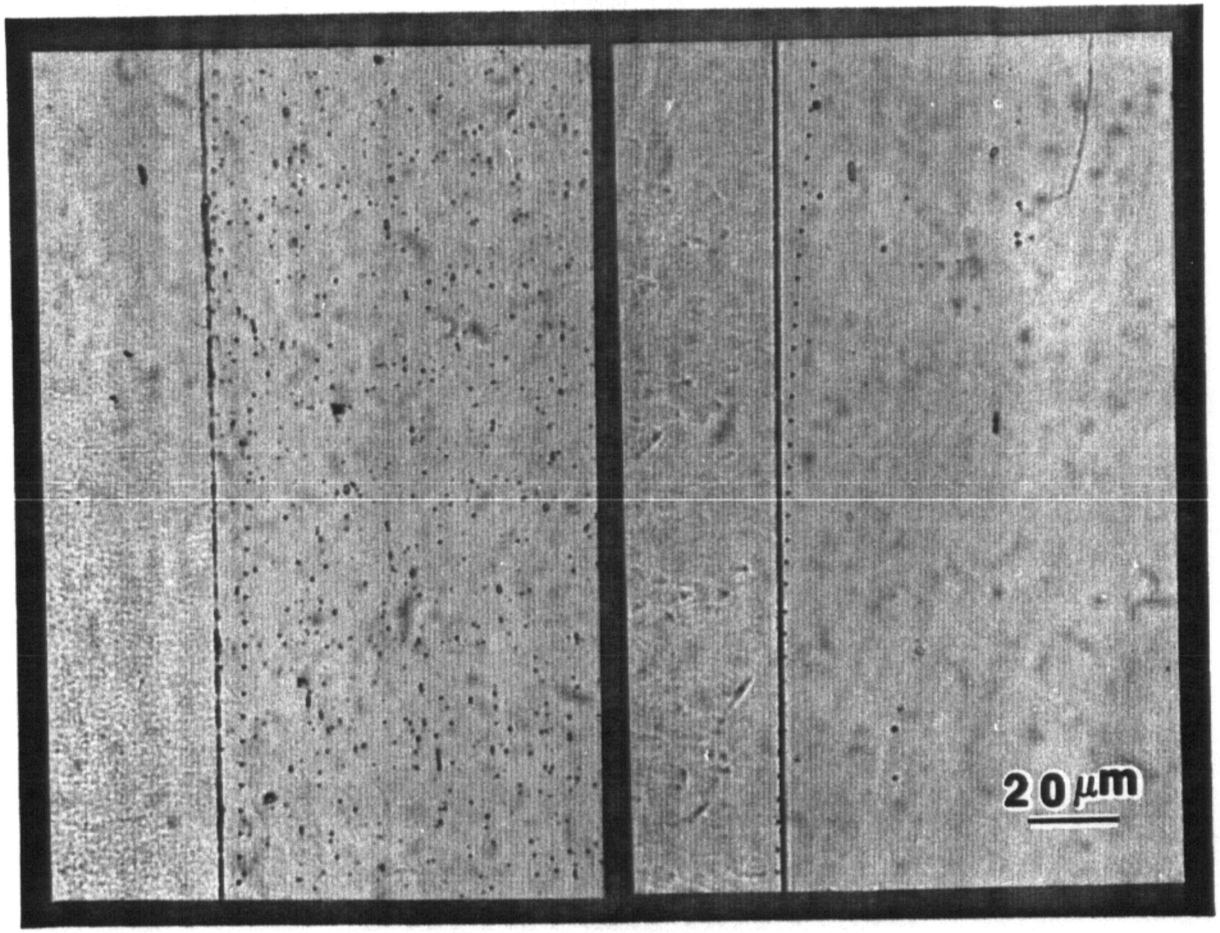

Fig. 6.18 Optical micrographs of indentations made in cross-sectioned samples of cold-worked and aged (left) and solution-annealed and aged (right) Cu-Ni-Be irradiated at 500°C. Copper Plating is to the right and Cu-Ni-Be to the left of the interface in each micrograph.

precipitates. No large precipitates are evident in the solution-annealed and aged sample.

Hardnesses from the irradiated and unirradiated regions of the samples, normalized to the pre-irradiation starting conditions, for indentations made normal to the irradiated surface are presented in Fig. 6.19. The Cu-Ni-Be alloy experiences softening in both thermo-mechanical treatments. The softening appears to begin at or above 300°C for the cold-worked and aged condition and is more pronounced in the irradiated region, with hardness losses of up to 25%. For the solution-annealed condition, only the 500°C sample experiences softening, with little difference between the irradiated and unirradiated regions. The normalized hardnesses from the indentation loading data, for all irradiated samples were relatively constant from a depth of 0.3 to 1.5 μm and were identical to those calculated at 0.5 and 1.5 μm from the unloading data. Both 500°C samples showed a dramatic drop in normalized hardnesses for depths less than 0.3 μm.

Ratios of irradiated to unirradiated bulk hardnesses made in cross-section are shown in Figs 6.20 and 6.21 for the solution annealed and aged and cold-worked and aged conditions, respectively. In the solution-annealed and aged condition, there is about a 5% drop in hardness in the irradiated region relative to the unirradiated region with about a 5% standard deviation in the data. The 400°C cold-worked and aged samples show almost no extra irradiation-induced softening, but the scatter of data is large, with standard deviations of about 10% for many points. At 500°C, the cold-

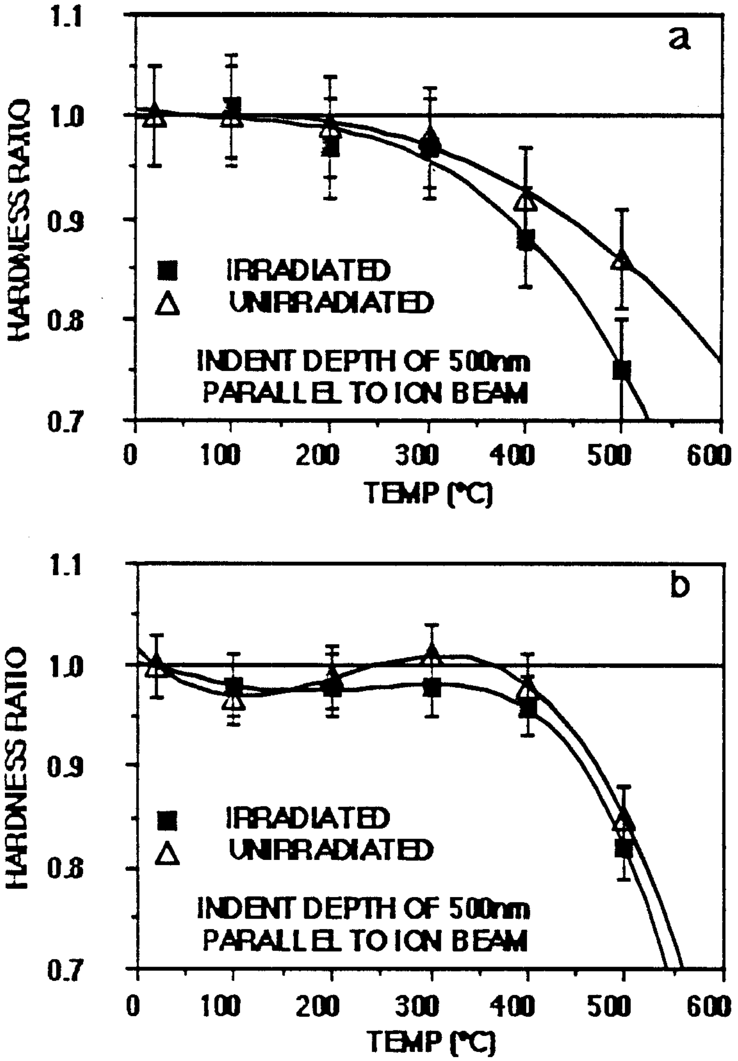

Fig. 6.19. Ratios of irradiated and unirradiated hardnesses to original hardness as a function of irradiation temperature for cold-worked and aged (a) and solution-annealed and aged (b) Cu-Ni-Be.

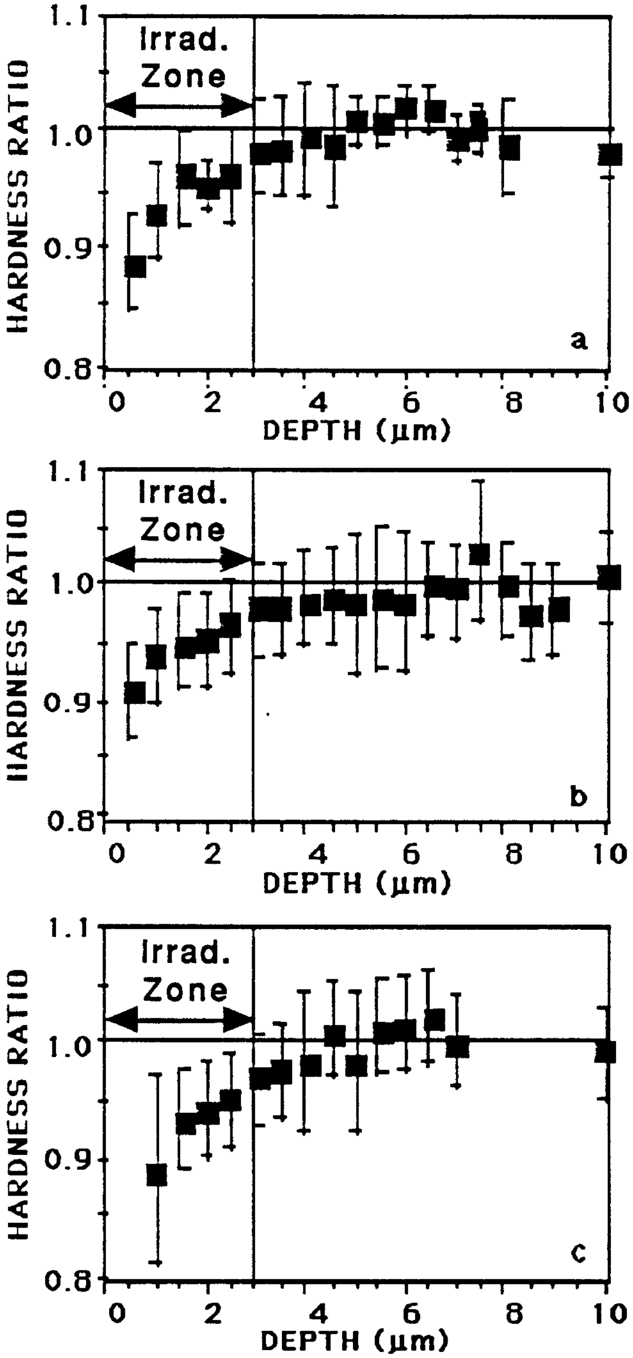

Fig. 6.20. Ratio of hardness to average unirradiated hardness versus depth from the irradiated interface for solution-annealed and aged Cu-Ni-Be at 300°C (a), 400°C (b) and 500°C (c).

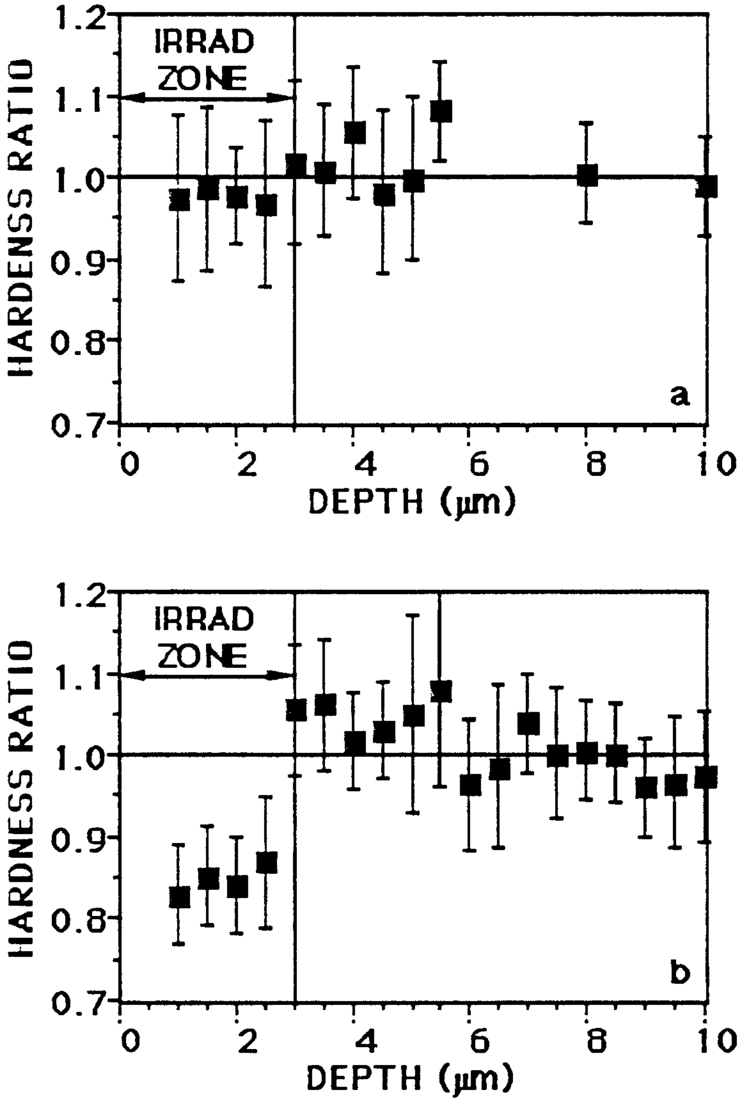

Fig. 6.21. Ratio of hardness to average unirradiated hardness versus depth from irradiated interface for cold-worked and aged Cu-Ni-Be irradiated at 400°C (a) and 500°C (b).

worked and aged sample shows a further 15% decrease in irradiated hardness and noticealbe scatter of the data.

Modulus measurements made in cross-sectioned samples did not show any change in irradiated modulus relative to unirradiated. However, the spread in data prevented any change less than 15-20% from being discernible. Small 5-10% drops in modulus were seen in the 400°C cold-worked and aged sample and the 500°C solution annealed and aged sample with indentations made normal to the surface. A modulus drop of about 10% was seen in the unirradiated region and a distinct 30% drop was seen in the irradiated region of the 500°C cold-worked and aged sample indented normal to the irradiated surface. Modulus measurements made from indentations normal to the irradiated surface had about a 10% standard deviation in the data.

VI. B. 2. Cu-Al20

Figure 6.22 shows the ratios of irradiated to unirradiated hardnesses for Cu-Al20. Samples irradiated to 20 dpa at 1μm in a temperature range of 200-500°C are presented in Figs. 6.22 a-d, respectively, and samples irradiated to 40 dpa (1 μm) at 300 and 400°C are presented in Figs 6.22 e and f, respectively. Even with peak damages over 150 dpa in some samples neither irradiation nor temperature have any noticeable effect on the hardness of this alloy. No change in modulus was detected either.

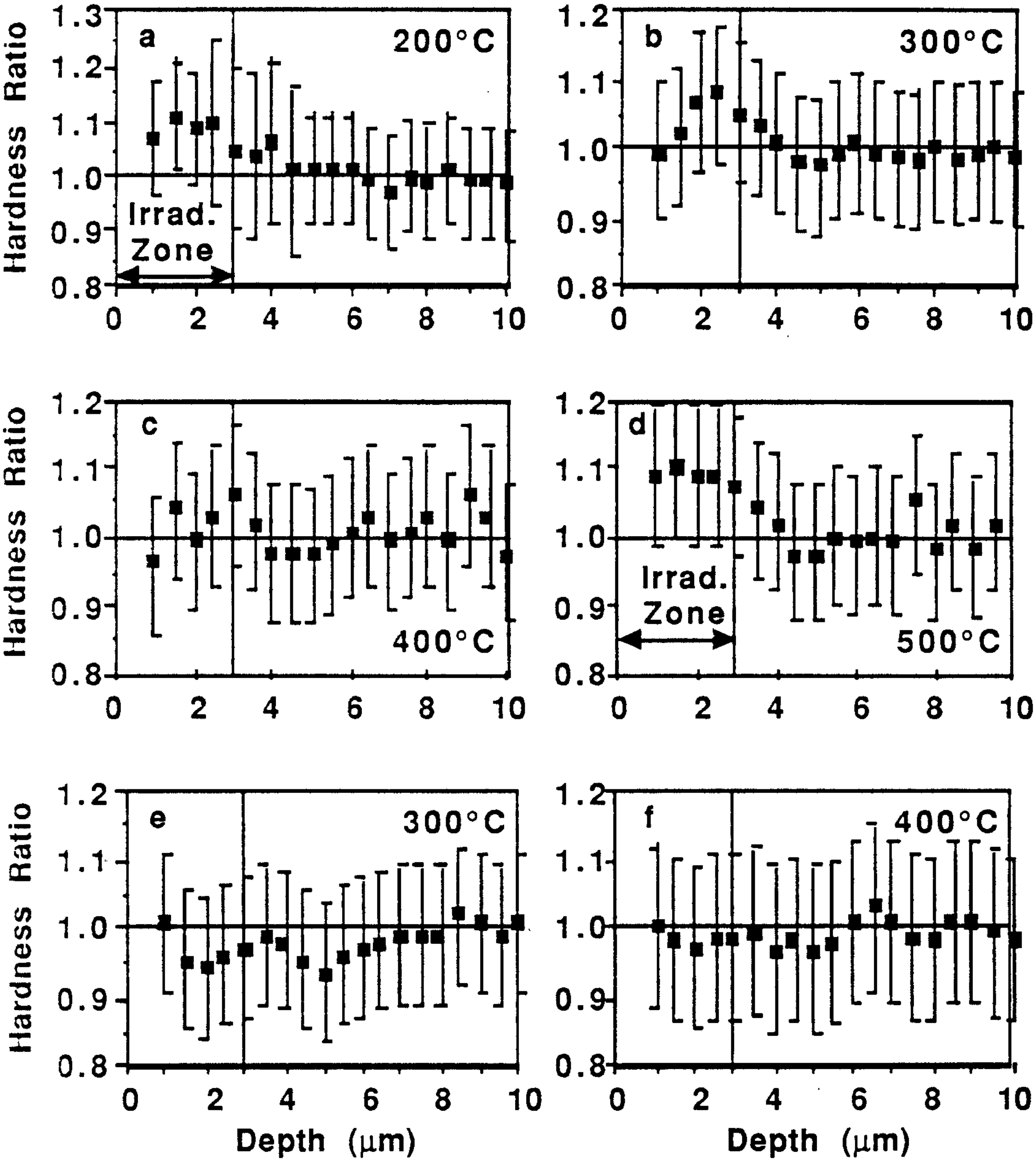

Fig. 6.22. Ratio of hardness to unirradiated hardness versus depth from the irradiated surface for Cu-Al20 irradiated to 20 dpa (a-d) and 40 dpa (e-f) at 1 μm for various temperatures.

CHAPTER VI

REFERENCES

1. L.-M Wang, Ph.D. Thesis, Materials Science Program, University of Wisconsin-Madison (1988).

2. Certification of Material Conformance, Brush Wellman Inc., Elmore, Ohio 43416, May 13, 1981 (received 1984).

3. A. Guha, in **High Conductivity Copper and Aluminum Alloys**, E. Ling and P.W. Taubenblat (Eds.), TMS-AIME (1984) 133.

CHAPTER VII

DISCUSSION

VII. A. Ni-Cu Alloys

Void suppression in Ni-Cu alloys has been attributed to clustering of like atoms, and this suppression leads to the nucleation of dislocation loops [1]. It is thought that clustering is on a finer scale in the Ni-50% Cu relative to the Ni-10% Cu, thus resulting in a higher density of smaller loops in Ni-50% Cu [1]. The loop characteristics change very little in Ni-50% Cu with increasing dose, and correspondingly, there is little change in hardness. At the highest dose , more large loops (d > 75 nm) are observed than for the lower doses in the Ni-10% Cu. Some of these larger loops are seen to extend beyond the end of the damage region. Slip of the larger loops to the surface and into the bulk may account for the lower hardness increase in the 25 dpa sample relative to the 5 and 10 dpa samples.

All hardness values (see Fig 6.4) were taken from an indentation depth of 150 nm. Hardness values calculated from the loading and unloading curves yielded identical ratios. For these values to have much meaning they should represent they should represent bulk values. At about this depth, hardness values start to rise with decreasing load; however if the ratio of irradiated to unirradiated hardness remains constant then it can be assumed that bulk trends are being observed. Figures 7.1 a and b show the ratio of irradiated versus unirradiated hardness for Ni-5 % Cu in the electro-

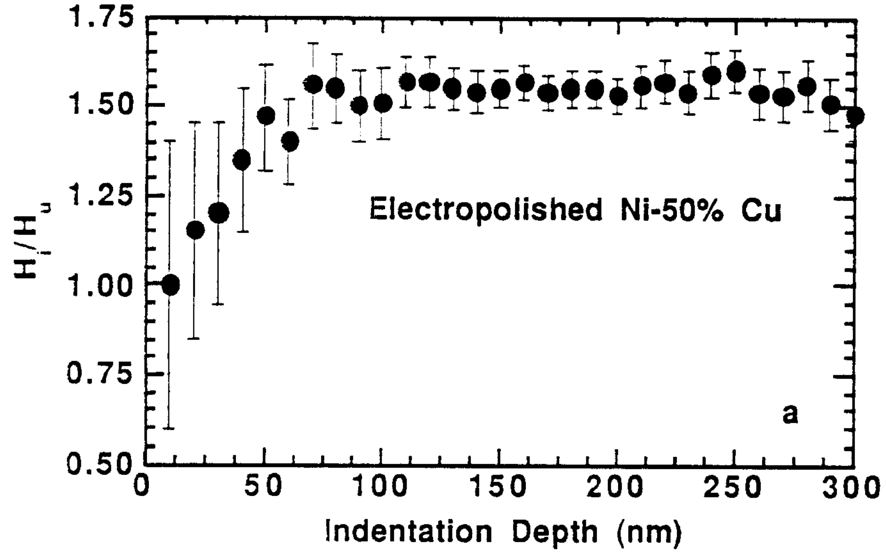

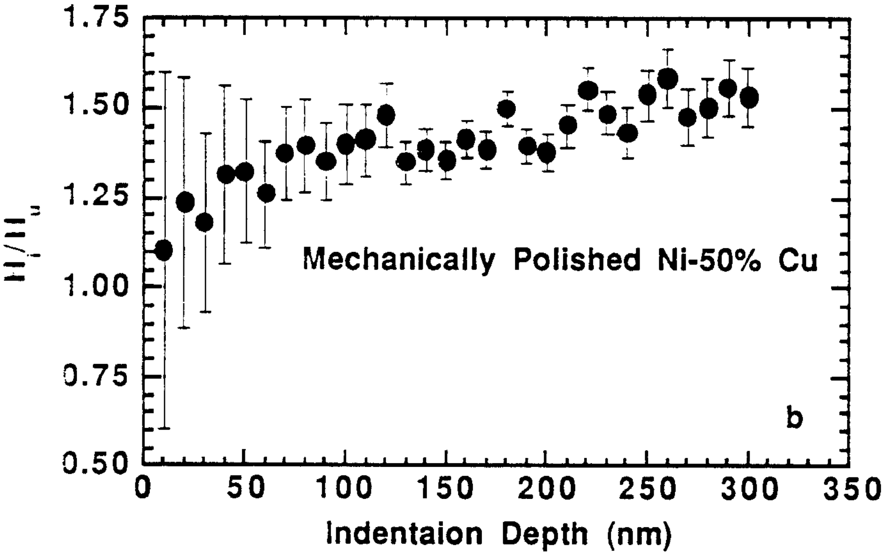

Fig. 7.1. Ratio of irradiated to unirradiated hardness for cross-sectioned Ni-50% Cu versus indentation depth for electopolished (a) and mechanically polished (b) surfaces.

polished and mechanically polished conditions, respectively. For depths greater than 70 nm the ratio is relatively constant and the standard deviation in the data reaches a reasonable value at a depth of 150 nm (this was also seen in the Cu-Ni-Be alloy). The drop in the hardness ratio below 70 nm may be the result of a hardness increase in the well annealed, nearly dislocation free unirradiated bulk as the indenter tries to nucleate dislocations in a perfect crystal (see Chapter III for further explanation of the hardness increase at ultra-low loads in well annealed metals). A similar result was seen by Zinkle in pure copper [2]. It should be noted that the scatter in data below 100 nm is quite large and could also account for the the drop in the hardness ratio. The mechanically polished sample shows a constant, but about 10% lower, hardness ratio for depths greater than 100 nm sa well as large scatter in data below 100 nm. The 10% lower hardness ratio is probably the result of work hardening of the dislocation free unirradiated zone. This type of result was also seen by Zinkle [2] and by the author in solution-annealed Monel K-500 (see appendix).

In all the samples tested, the hardness ratio is approximately the same across the irradiated zone despite the fact that the dpa varies with depth. This trend was observed by Zinkle [2] and in the copper alloys examined in this study. The constant hardness ratio across the irradiated zone can, in part, be accounted for by the fact that the actual size of the indentations (~7 x the depth across) are smaller than the volume which contributes to the hardness [3]. Thus, hardness is sampled over a wide range of dpa's, and any hardness change associated with the changing dpa level will be damped. It also appears from the TEM results (see Fig 6.1) that the dislocation loop sizes and densities are the same across the irradiated zone for both alloys. This, coupled with the hardness data, indicates that saturation of the radiation hardening has probably occurred. Neutron irradiations below the void swelling temperatures of Cu and Ni have shown saturation of radiation hardening at < 0.1 dpa.[4-7].

Theoretical hardening due to dislocation loops can be represented by [8]:

$$\Delta\sigma_y = \sqrt{3\,\Delta\tau} \approx 0.5\,G\,b\,(Nd)^{1/2} \qquad \text{small loops}$$

or

$$\approx 1.2\,G\,b\,d\,(N)^{2/3} \qquad \text{large loops}$$

where σ_y is the yield strength, τ the shear stress, G the shear modulus, b the Burgers vector, N the loop density and d the loop diameter. Small loops interact through short range forces, while large loops interact through long range forces [8]. The cutoff for small and large loops is relatively arbitrary but is often taken to be less than 10 nm [8]. Hardness can be be related to yield strength by $H = C\sigma_y$, where C is a constant (usually taken to be 3 for diamond pyramid hardness tests) [9-11 and see Chapter III]. Thus, the yield strength can be determined from:

$$\Delta\sigma_y/\sigma_y \approx \Delta H/H$$

or

$$\Delta\sigma_y \approx \sigma_y\,(H_i/H_{u\,-\,1)}$$

where H_i and H_u are the irradiated and unirradiated hardnesses, respectively. Because the this ratio is constant for indentation depth > 70 nm the absolute hardness values are not needed and the actual value for C does not need to be known. Table 7.1 shows the comparison of the change in yield strength calculated from theory and hardness changes. The calculations were made using an average loop diameter and an average Burgers vector assuming half the loops to be perfect and the other half faulted. The yield strength for the unirradiated samples was taken to be ~ 150 MPa [12]. For Ni-10% Cu, the results are remarkably close using either the small or large loop calculations; however, the large loop calculation is probably a more valid model for this composition. Fair agreement is achieved in Ni-50% Cu using the two models; however, even better agreement can be achieved if a combination of the two models is used ($\Delta\tau = \Delta\tau$ (small) + $\Delta\tau$ (large)) [8] and it is assumed that about 85% of the loops are small (~ 5 nm) and the rest are large (~ 15 nm). With such a high density of small loops, it is possible that many loops and other defects under

Table 7.1. Comparison of yield strength changes in irradiated Ni-Cu from hardness (MPM) measurements and theoretical calculations in MPa.

Composition	MPM Measurement	Small Loop Model	Large Loop Model	Large + Small Loop Models
Ni-10% Cu	38 ± 4	32	38	
Ni-50% Cu	83 ±8	52	51	73

5 nm were missed. Also, loop densities are probably known only to within a factor of 2 to 3 due to TEM sample thickness uncertainties.

VII. B. Copper Alloys

VII. B. 1. Cu-Ni-Be

The hardnesses shown in Table 6.2 indicate that the solution-annealed and aged condition is stronger than the cold-worked and aged condition for Cu-Ni-Be. This is due to the different solutionizing treatments that were employed for each condition. The cold-worked and aged samples were solution-annealed at 900°C prior to cold-working and aging [13]. The solution-annealed and aged samples were solution-annealed at 950°C prior to aging in order to insure complete solution of the solutes. Solution-annealing at temperatures near 950°C prior to cold-working and aging has been shown to significantly increase the strength of this alloy (σ_y ~ 900 MPa) [14]. Therefore, it is not surprising that using a much higher solution-annealing temperature yields a solution-annealed and aged hardness which is higher than a cold-worked and aged hardness using a conventional solution-annealing temperature.

Vickers and Knoop indentations were made in the solution-annealed and aged alloy using two standard microhardness testers, one set up for loads from 10 to 1000 grams and the other set up for loads from 0.5 to 50 grams. These hardness values were then compared to values obtained from the MPM. Figure 7.2 shows the comparison of hardness as a function of load (a) and of indentation depth (b). The high-load tester (tester 1) was not vibration isolated, and the apparent drop in hardness can be attributed to vibrations causing an increase in the measured diagonals by about 1 micron. The low-load tester (tester 2) was vibration isolated, but was kept in a room with a lot of machinery and activity, and the trend corresponds to microscope resolution of ± 0.5 μm and a 0.5 μm increase in diagonal due to vibrations. The MPM results shows that hardness is relatively flat in the range the other indenters can test and then the hardness rises about 20 % at 50 nm deep or ~ 0.05 grams.

Further aging of the two alloy conditions at 400°C for 10 to 1000 hours showed little change in microhardness. The diffraction pattern of the 1000 hour solution-annealed and aged alloy shows the same distinctive <002> streak that the untreated alloy has, indicating that the aging has not coarsened the G.P zones. However, some bunching (increase in intensity)

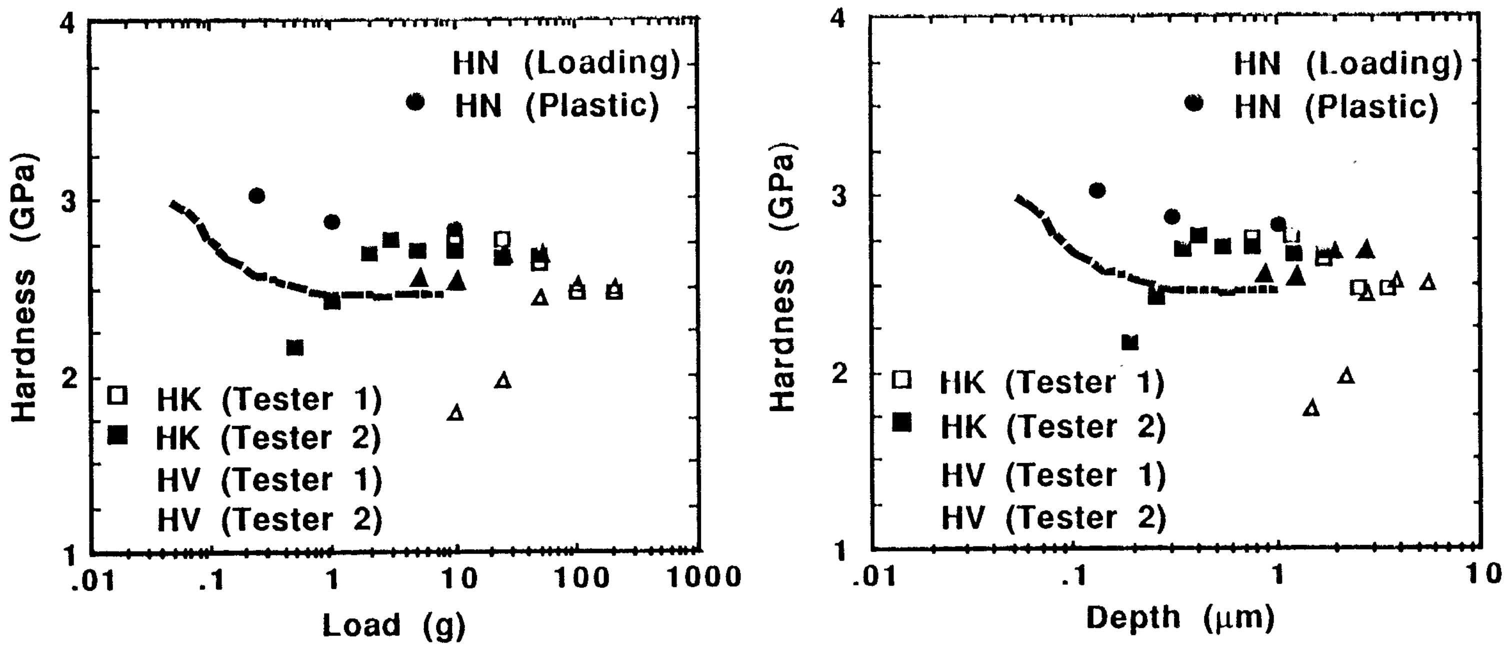

Fig. 7..7. Knoop (HK), Vickers (HV) and Nano (HN) Hardness versus load (right) and depth (left). Two different testers used for Knoop and Vickers tests.

of the <002> streak at the 2/3 <002> position and the increase in precipitate size in dark field indicates the formation of the coherent γ'' precipitate while retaining some G.P zones. In another study, tensile tests of this alloy in the solution-annealed and aged condition following further aging at 400°C for 1000 hours gave similar results; however for the cold-worked and aged condition this extra aging resulted in significant softening [15].

The fact that the alloy in both conditions exhibits softening at 500°C is reasonable, considering that this temperature is above the aging temperature (482°C) for this alloy. The formation of distinct diffraction spots at the 2/3 <002> position and the presence of distinct platelets indicates that the G.P. Zone have completely coarsened in to γ'' and the semi-coherent γ' (the platelets). There appear to be only γ' in the irradiated zone of the cold-worked and aged sample and the grains appear much larger and more equi-axed throughout the sample than any other cold-worked and aged sample. Large micron-size precipitates were observed on the electropolished surface of the cold-worked and aged sample, but were absent from the solution-annealed and aged sample. This indicates that the cold-worked and aged condition coarsens more then the solution-annealed and aged conditions and it also exhibits recovery and recrystallization. This is further evidenced by the hardness results which show that the cold-worked and aged alloy softened more than the solution-annealed and aged alloy, particularly in the irradiated zone. Thermally-induced and radiation-enhanced coarsening and recovery and recrystallization were observed in another ion irradiation study of the cold-worked and aged condition [16].

For temperature of 400°C and lower, irradiation has no observed affect on the solution-annealed and aged samples. The <002> streaks show no bunching even after irradiation at 400°C. Neutron irradiation to 16 dpa of this alloy in this condition at 450°C showed what appeared to be a radiation-induced drop in yield strength of 20%, and various levels of swelling with increasing dose [15,17-19].

The cold-worked and aged condition is obviously more sensitive to irradiation and/or temperature than the other thermo-mechanical treatment. It appears that the cold-worked and aged condition overages very easily at temperatures over 300°C. Bunching in the <002> streak in the unirradiated region of the 400°C sample indicates some coarsening of the G.P. zones. In the irradiated region the near complete loss of streaks and the strong intensity maximum at the 2/3 <002> position and the appearance of distinct platelets indicates the formation of γ' and γ with either some very large G.P zones or small γ'' and γ' precipitates with strong coherency strains. The hardness drops observed in the cold-worked and aged samples are similar to those found in recovered and recrystallized Cu-Ni-Be [20]. Ion irradiation of this alloy to similar dpa levels with helium co-implantation, showed distinct coarsening above 350°C and precipitate dissolution below 350°C; however single ion irradiation at 300°C showed little effect of irradiation on the precipitate morphology [16]. Neutron irradiation of this condition at 450 °C showed a large radiation-enhanced drop in strength, extensive recrystallization and voids in the recrystallized regions [17-19,21]. Microscopy of cold-worked and aged Amzirc and MZC, irradiated under conditions similar to this study, showed radiation-enhanced recovery and recrystallization and was attributed to radiation-enhanced diffusion (see Fig. 2.3), which accurately predicted the enhancement of recrystallization [22,23]. Radiation-enhanced diffusion has a negative effect on cold-worked alloys by accelerating recovery processes, which in turn accelerates coarsening processes. This results in the cold-worked and aged samples having inferior high temperature response than the solution-annealed and aged samples.

Using the same same relationship of change in hardness to change in yield strength that was used for the Ni-Cu alloys, changes in yield strength can be calculated for the Cu-Ni-Be samples. Using this relationship it was found that the solution-annealed and aged sample at 500°C had a drop in yield strength of 140 MPa in the irradiated and unirradiated areas. The 400°C cold-worked and aged sample showed a decrease of 80 MPa in both areas, while the 500°C sample lost 120 MPa in the unirradiated region and 200 MPa in the irradiated zone. The trends are similar to those found in the neutron study [15]. The yield strength dropped far more in the neutron study than in this study; however, time at temperature are vastly different (~ 1000 hours [15] versus ~ 10 hours, respectively).

Various factors affect the hardness values measured in this study. Hardness measurements include contribution from the sample from a volume with a radius ten times the depth of indentation [3]. However, the major fraction of the hardness comes from much smaller volumes(radius 3 to

4 times the indentation depth). Thus, indentations to a depth of 500 nm, made normal to the irradiated surface, should represent hardness contributions of the irradiated zone almost entirely. However, as in the case for the Ni-Cu alloys, both modes of indentations (normal and in cross-section) are sampling a wide range of dpa values at any given depth. Considering that dpa varies from less than 10 dpa to about 40 dpa in the irradiated zone, it is still surprising that the hardness ratio for normal indentations from 500 to 1500 nm deep and for cross-section indentations are constant in the irradiated zone. The Ni-Cu alloy study and a related study in Amzirc found similar results [2]. With the hardness ratios of both methods and the microstructure being constant through the irradiated zone, it indicate that the microstructural factors that contribute to hardness are independent of dpa level for a given ion fluence (~ 3 x 10^{20} ions/m^2).

Indentations were made normal to the irradiated surface and perpendicular to it in cross-section in order to compare the two methods. Table 7.2 shows that for hardness measurements, there is close agreement for the alloy with both treatments. The standard deviation for the cold-worked and aged condition is much larger than the solution-annealed and aged condition, particularly in cross-section. Problems were encountered indenting the former because of the micron size precipitates, which are about the same size as the cross-section indentations. This can be seen in Fig. 6.18. The hardness values and their associated standard deviations do not include indentations made directly on a precipitate, a number of which were made in the cold-worked and aged samples. If these indentations

Table 7.2 Ratios of Hardnesses in the Irradiated Zone to Hardness in the Unirradiated Zone.

Thermo-mech. Treatment	Temperature (°C)	Normal	Cross-section
Solution- annealed & Aged	300	0.97 ± 0.03	0.95 ± 0.04
	400	0.98 ± 0.03	0.95 ± 0.04
	500	0.97 ± 0.03	0.94 ± 0.04
Cold-worked & Aged	400	0.95 ± 0.05	0.98 ± 0.07
	500	0.87 ± 0.05	0.85 ± 0.10

were included, the ratios would be different and the standard deviations would be much larger. Normal Indentations of 500 nm or greater are not as severely affected by the coarsened precipitates.

For modulus measurements, the scatter in data for the cross-section indentations made any conclusive trends impossible to detect. For the normal indentations, a significant change in modulus was observed only in the irradiated zone of the cold-worked and aged specimen, where it was seen to drop ~ 30%. The irradiated modulus is, within the standard deviation of the data, about the same as pure copper. This was seen in another study using this technique, where recovery and recrystallization occurred during irradiation [2]. Modulus drops have been reported in irradiated stainless steel and have been attributed to swelling [24,25]. No voids were observed in any of the Cu-Ni-Be samples used in this study. The drop in modulus is probably the result of the loss of precipitates with strong coherency strain in the irradiated zone.

/II. B. 2. Cu-Al20

The hardness results indicated that, even with damage levels higher than 150 dpa, this alloy displays a remarkable resistance to degradation via irradiation. Microscopy is needed to confirm that these samples are as resistant to irradiation as the hardness results indicate. However, in the light of the results of other irradiations of this alloy and similar alloys to both ion [16] and neutron irradiation [15,17-19,21,26-33], these results are not unexpected. Dual ion irradiation of Cu-Al60 resulted in a few isolated voids in regions with only a few large alumina particles and some dissolution of the alumina particles is claimed [16]. Frost and Russell have postulated that these small insoluble particles would suffer from recoil re-solution, but would re-precipitate as even smaller insoluble particles [34]. This would result in an increase in the strength of these types of alloys. Even though the doses used in this study are more than five times higher, no change of hardness was observed. Neutron irradiations of these alloys have failed to observe any void formation or other changes in microstructure and have seen only small drops in yield strength following irradiations up to about half the dose used in this study [15,17-19,21,26-33].

CHAPTER VII

REFERENCES

1. L.-M Wang, Ph.D. Thesis, Materials Science Program, University of Wisconsin-Madison (1988).
2. S.J. Zinkle and W.C. Oliver, J. Nucl. Mater. 141-143 (1986) 548.
3. L.E. Samuels and T.O. Mulhearn, J. Mech. Phys. Solids 5 (1957) 125.
4. M.J. Makin, in **Radiation Effects**, W.F.Sheely (ed), Gorden and Breach, New York (1967) 627.
5. J. Diehl, in **Radiation Damage in Solids**, IAEA, Vienna (1962) 129.
6. I.A. El-Shanshoury and H. Mohammed. Soviet Atomic Energy 25 (1968) 265.
7. I.A El-Shanshoury, J. Nucl. Mater. 45 (1972) 245.
8. N.M. Ghoniem, J. Alhajji and F.A. Garner, in **Effects of Radiation on Materials**, ASTM STP 782, H.R. Brager and J.S. Perrin (eds.) ASTM, Philadelphia (1982) 1059.
9. D. Tabor, **The Hardness of Metals**, Clarendon Press, Oxford (1951).
10. J.R. Cahoon, W.H. Broughton and A.R. Kutzak, Met. Trans 2 (1971) 1971.
11. J.J. Gilman, in **The Science of Hardness Testing and Its Research Applications**, J.H. Westbrook and H. Conrad (Eds.) ASM (1973) 51.
12. **Metals Handbook**, 9th ed.,vol 3, ASM (1980) 660.
13. Certification of Material Conformance, Brush Wellman Inc., Elmore, Ohio 43416, May 13, 1981 (received 1984).

14. A. Guha, in **High Conductivity Copper and Aluminum Alloys,** E. Ling and P.W. Taubenblat (Eds.), TMS-AIME (1984) 133.

15. HR. Brager, H.L. Heinish and F.A. Garner, J. Nucl. Mater. 133/134 (1985) 676.

16. J.A. Spitznagel, et. al., Nucl. Instr.and Meth. B 16 (1986) 279.

17. H. R. Brager, J. Nucl Mater. 141-143 (1986) 79.

18. H. Brager and F.A. Garner, in ASTM STP 1046, in press.

19. F.A. Garner, H.R. Brager and K.R. Anderson, FRM Semiannual Progress Report, DOE/ER-0313/7 (1989) 223.

20. W. Weinlich, Metall. 34 (1980) 135.

21. H.R. Brager, J. Nucl. Mater., 141-143 (1986) 163.

22. S.J. Zinkle, Ph.D Thesis, Nuclear Engineering Department, University of Wisconsin-Madison (1985).

23. S.J. Zinkle, G.L. Kulcinski and L.K. Mansur, J Nucl. Mater. 141/143 (1986) 188.

24. J.L. Straalsund and C.K. Day, Nucl. Tech. 20 (1973) 27.

25. M. Marlowe and W.K. Appleby, Trans Am. Nucl. Soc. 16 (1973) 95.

26. K.R. Anderson, F.A. Garner, M.L. Hamilton and J.F. Stubbins, FRM Semiannual Progress Report, DOE/ER-0313/6 (1989) 357.

27. K.R. Anderson, F.A. Garner, M.L. Hamilton and J.F. Stubbins, FRM Semiannual Progress Report, DOE/ER-0313/7 (1989) 213.

28. R.J. Livak, T.G. Zucco and J.C. Kennedy, ADIP Semiannual Progress Report, DOE/ER-0045/14 (1985) 152.

29. R.J. Livak, H. M. Frost, T.G. Zucco, J.C. Kennedy and L.W. Hobbs, J. Nucl. Mater. 141-143 (1986) 160.

30. H. M. Frost and , J.C. Kennedy, J. Nucl. Mater. 141-143 (1986) 169.

31. R.J. Livak, T.G. Zucco and L.W. Hobbs, J. Nucl. Mater. 144 (1987) 121.

32. M. Ames, G. Kohse, T.-S. Lee, N.J. Grant and O.K. Harling, J. Nucl. Mater. 141-143 (1986) 169.

33. O.K. Harling, N.J. Grant, G. Kohse, M. Ames, T.-S. Lee and L.W. Hobbs, J. Mater. Res. 2 (1987) 568.

34. H.J. Frost and K.C. Russell, J. Nucl. Mater. 103/104 (1982) 1497.

CHAPTER VIII

SUMMARY AND CONCLUSIONS

Two Ni-Cu alloys (Ni-10% & 50% Cu) and two copper alloys (Cu-1.8% Ni-0.3% Be and Cu-0.2% Al as Al_2O_3) were irradiated with 14 MeV heavy-ions to various damage levels at a wide range of temperatures. The mechanical property changes following irradiation of these alloys were subsequently examined using the Nanoindenter, a mechanical properties microprobe (MPM) capable of extracting data from submicron structures. Transmission electron microscopy (TEM) was used to study the radiation induced/enhanced microstructural changes, which were compared to the mechanical property changes.

The Ni-Cu system's resistance to void formation results in the nucleation of a high density of dislocation loops under irradiation. The higher density of smaller loops in Ni-50% Cu causes a hardness change twice that of Ni-10% Cu. The analysis of the Ni-Cu data demonstrates that the measured changes in hardness by the MPM compare favorably with theoretical calculations made using TEM measurements of dislocation loop sizes and densities. Radiation hardening appears to saturate at or below 5 dpa for these compositions.

This study, coupled with the neutron results, indicates that the solution-annealed and aged condition of the Cu-Ni-Be alloy has a far better response to irradiation at elevated temperatures than its cold-worked and aged counterpart. A moderately high dislocation density (20% cold-work) appears to accelerate softening in Cu-Ni-Be when exposed to temperatures greater than 300°C. Overaging, recovery and recrystallization is further accelerated when irradiation is included for the cold-worked condition. When the alloy is only aged following solution-annealing, neither temperature nor irradiation affect the hardness or microstructure, unless the alloy is exposed to temperatures higher than the aging temperature of 482°C. For exposures over the aging temperature, irradiation has little effect beyond thermal overaging for the solution-annealed and aged treatment. In either case, even short-term exposure to temperature only slightly above the aging temperature results in rapid overaging and should be avoided.

The preliminary results of this study, coupled with the neutron results, indicate that Cu-Al20 is practically invulnerable to irradiation. Heavy-ion irradiation of this alloy produced no discernable change in its mechanical properties.

The MPM appears capable of making direct hardness and modulus measurements in the narrow irradiated region. For indentations depths greater than 70 nm in cross-sectioned samples, the relative change in hardness appears to represent bulk trends Indentations made normal to the irradiated surface yield results similar to indentations made parallel to the surface in cross-section. This is possible as long as the hardness does not vary with dpa through the irradiated zone for a given ion fluence, and that the irradiated zone is deeper the 2 to 4 times the normal indentation depth and 2 to 3 times the width of cross-section al indentations. However, consistent results for indentations become difficult when features about the same size as the indentation are present (i.e. large precipitates).

CHAPTER IX

FUTURE WORK AND RECOMMENDATIONS

The recommendations of this study for future work are the following:

1. Irradiations of the Ni-Cu system to lower dpa levels are needed to determine when the saturation of radiation hardening occurs and what the fluence/dpa dependence is.

1. Explore further the fluence/dpa effect on the microstructure and mechanical properties of Cu-Ni-Be and other complicated alloy systems in order to determine which has more influential on the properties of ion irradiated alloys.

2. Perform dual heavy-ion and helium irradiation of Cu-Ni-Be and Cu-Al20, in order to examine the combined effects of helium and radiation damage on the properties of these alloys.

Based on this thesis study the following can be recommended:

1. Solution-annealed and aged Cu-Ni-Be should be the copper alloy used for fusion reactor applications requiring moderate temperatures (T = 100 to 400°C), moderate conductivity (~ 50% IACS) and high strength (> 500 MPa)

2. For all high temperature (T > 400°C) or high conductivity (>80% IACS) or moderate strength (~ 500 MPa) copper needs Cu-Al20 should be used.

3. If the NRC class C restrictions are not a concern, Cu-alumina alloys should be considered for structural materials applications in fusion reactors (e.g. first walls) with operating temperatures over 500°C.

APPENDIX

RELATED RESEARCH

In addition to the work done specifically for this thesis, the author has been involved in other research projects. Two of these projects are indirectly related to this thesis and are briefly summarized in this chapter. The work on Amzirc and MZC was part of a study [1] that this thesis builds upon. The microindentation hardness study of nitrogen implanted Monel K-500 is included because of the alloy's similarity to the Ni-Cu alloys used in this thesis. Table A.1 lists the publications from these two studies

A Amzirc and MZC

The response of Amzirc (Cu-0.15% Zr) and MZC (Cu-0.8% Cr- 0.15% Zr-0.04% Mg) to heavy-ion irradiation was recently studied by Dr. S. J. Zinkle at the University of Wisconsin [1]. These alloys are high-strength, high-conductivity copper alloys that are being considered for applications in fusion reactors [2]. While no voids were found in any of the cold-worked and aged alloys (CWA), recovery and recrystallization were observed. In order to correlate the effect of recovery and recrystallization during irradiation on the physical properties of the alloy (e.g. strength and conductivity), a thermal annealing study was initiated by Zinkle with the assistance of the author. Microhardness, tensile strength and electrical conductivity were measured following thermal annealing and comparisons were made between the microstructures of the irradiated alloys and annealed alloys.

Table A.1 List of Publication From Related Work

1. S.J. Zinkle, D.H. Plantz, R.A. Dodd and G.L. Kulcinski, "Mechanical Properties and Microstructures of High-Strength Copper Alloys Following Thermal Annealing," DAFS Quarterly Progress Report DOE/ER-0046/17 (May 1984) 110.

2. S.J. Zinkle, D.H. Plantz, G.L. Kulcinski and R.A. Dodd, "Microstructures and Physical Properties of Cu-Zr and Cu-Cr-Zr-Mg Alloys," DAFS Quarterly Progress Report DOE/ER-0046/18 (Aug. 1984) 143.

3. S.J. Zinkle, D.H. Plantz, A.E. Bair, R.A. Dodd and G.L. Kulcinski, "Correlation of the Yield Strength and Microhardness of High-Strength, High-Conductivity Copper Alloys", J. Nucl. Mater. 133/134 (1985) 685.

4. S.J. Zinkle, D.H. Plantz, R.A. Dodd, G.L. Kulcinski and A.E. Bair, "Physical Properties of High-Strength, High-conductivity Copper Alloys," DAFS Quarterly Progress Report DOE/ER-0046/20 (Feb. 1985) 85.

5. M. Madapura, R.A. Dodd, J.R. Conrad, D.H. Plantz and F.J. Worzala, "Structure and Property Correlation of Plasma Source Ion Implanted Layers in Monel K-500 Alloy", presented at the 36th National Symposium and Topical Conference, American Vacuum Society, Aug. 19, 1989, and to be published in J. Vac. Sci.

The physical properties of Amzirc and MZC in the CWA state and the solution-annealed and aged state (SAA) are listed in Tables A.2 and A.3. Polished foils of the CWA alloys were annealed in a high-vacuum furnace for a variety of times (0.25, 1.0, 10 and 100 hours) and temperatures (300-600°C). Following annealing, Vickers microhardness measurements were made with an indenter load of 200 g. Resistivity wires were cut from the

Table 5.2 Measured Mechanical Properties at 20°C

Alloy	Heat Treatment	Microhardness	Yield Strength (0.2% Offset)	Tensile Strength	Elongation in 5.1 mm
AMZIRC	SA	50 HVN	110 MPa	150 MPa	21%
	SAA	51 HVN	140 MPa	200 MPa	27%
	CWA	150 HVN	440 MPa	500 MPa	9%
MZC	SA	46 HVN	92 MPa	120 MPa	14%
	SAA	78 HVN	220 MPa	260 MPa	23%
	CWA	170 HVN	490MPa	540 MPa	9%

SA: Solution annealed (water quenched)

SAA: Solution annealed and aged 1 hour at 450°C for AMZIRC and 500°C for MZC

CWA: 90% cold-worked and aged 0.5 hours at 375°C for AMZIRC and 400°C for MZC

Table A.3. Measured Electrical Properties

Alloy	Heat Treatment	Resistivity (nΩ-m) 296 K	77 K	4.2 K	RRR =ρ 296/ρ 4.2	Conductivity (20°C)
AMZIRC	SAA	23.4 ± 0.2	8.3 ± 0.2	5.9 ± 0.1	4.0	27%
	CWA	22.9 ± 0.8	6.8 ± 0.6	4.0 ± 0.3	5.7	9%
MZC	SAA	33.0 ± 0.6	18.7 ± 0.9	18.3 ± 0.9	1.8	23%
	CWA	29.4 ± 0.6	14.4 ± 0.8	13.5 ± 0.8	2.2	9%

SAA: Solution annealed and aged 1 hour at 450°C for AMZIRC and 500°C for MZC

CWA: 90% cold-worked and aged 0.5 hours at 375°C for AMZIRC and 400°C for MZC

IACS: International Annealed Copper Standard, 100% IACS = 17.241 nΩ-m annealed foils and electrical resistivity measurements were made using standard 4 point probe techniques. Tensile data was obtained using miniature tensile specimens punched from the foils and measured at HEDL. TEM samples were prepared and examined by Zinkle using a JEOL 200-CX TEMSCAM microscope. TEM data from these samples will not be presented here, but may be found in the papers listed in Table A.1 and Reference 1.

Fig. A.1 shows a comparison of the response of the two alloys to a 1 hour anneal from 300°C to 600°C. MZC has a higher strength and lower electrical conductivity than Amzirc for all temperatures. Both alloys exhibit a recrystallization temperature of about 475°C. The conductivity is independent of recovery and recrystallization, but depends on the amount of solute leaving solution ($T<550°C$) or entering solution ($T>550°C$). The microhardness, yield strength, and conductivity measurements for all the annealing conditions are displayed in Fig. A.2. Stress-strain curves for the CWA and SAA alloys are presented in Fig. A.3. The relationship between Vickers microhardness and yield strength is plotted in Fig. A.4. Yield strength was found to be directly proportional to microhardness, σ_y (MPa) ~ 3 VHN, for both alloys. Both alloys gain the majority of their strength from cold working (i.e. dislocations). Amzirc gains very little strength from aging alone, while MZC gains some strength from aging. The SAA alloys display greater toughness (area under the stress-strain curve) than the CWA alloys. Because of the dependence of strength on cold-working (>90% cold-worked), recrystallization has a disastrous effect on these alloys. Using the Arrhenius approach to of recrystallization, long term recrystallization times

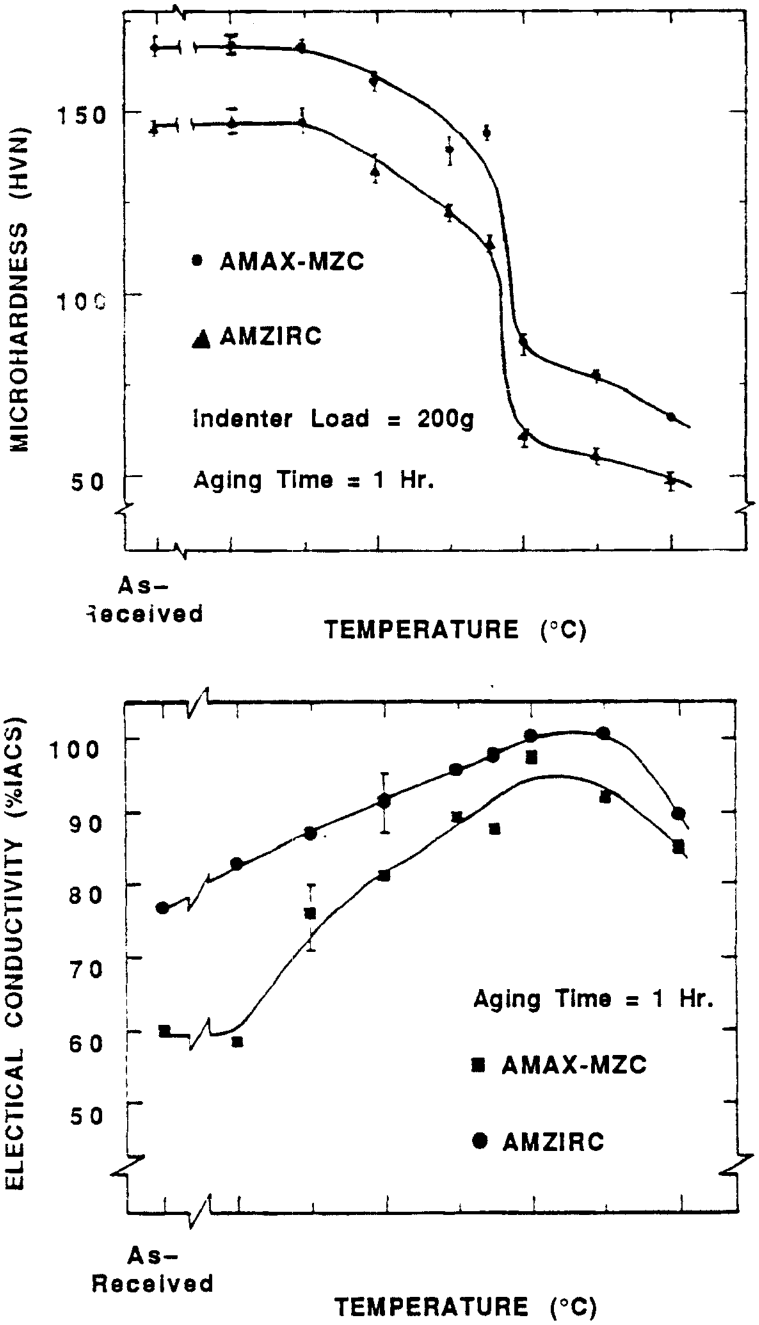

Fig. A.1. Vickers microhardness and electrical conductivity at 20 °C of the cold-worked and aged copper alloys versus anneal temperature.

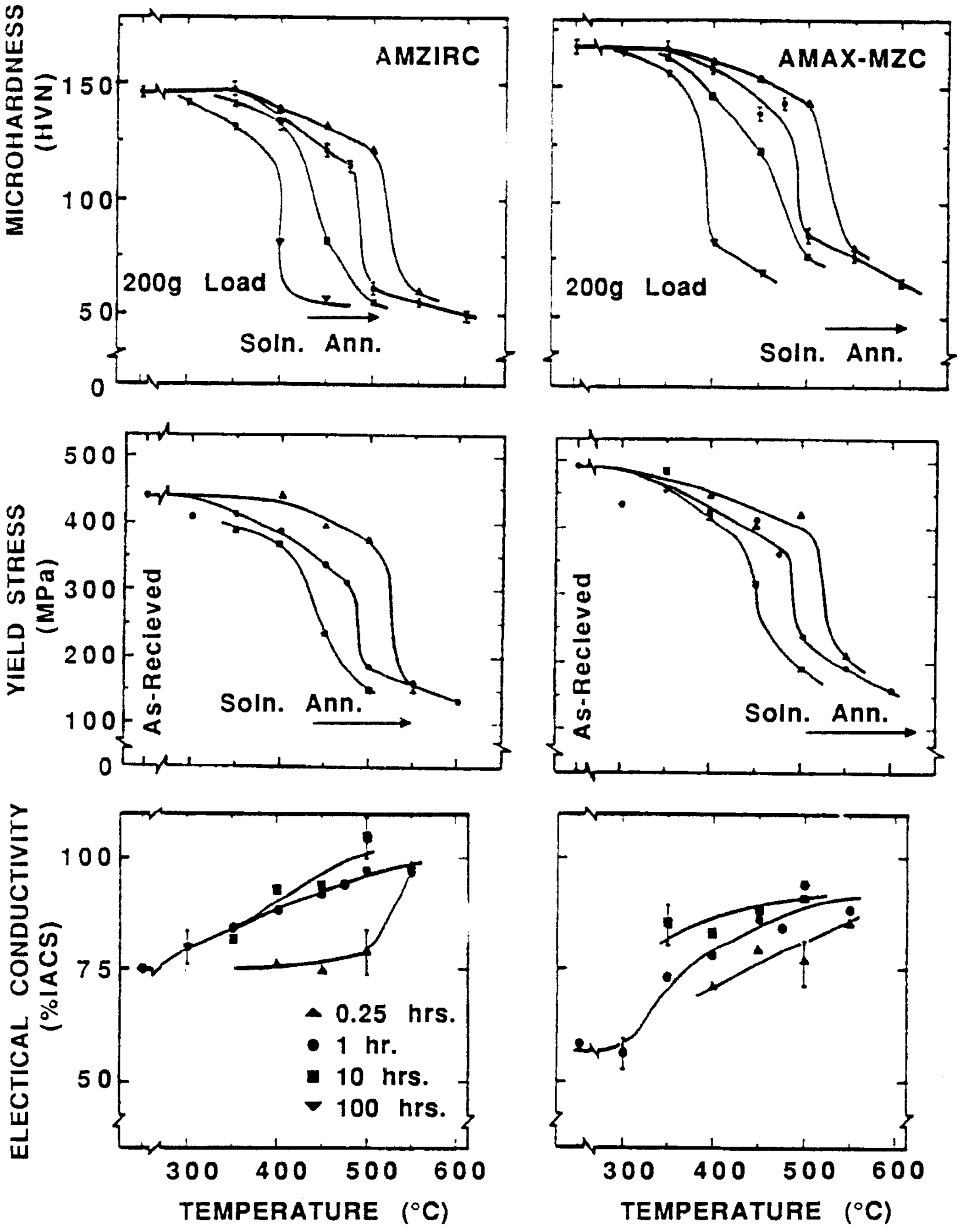

Fig. A.2. Physical properties of the cold-worked and aged copper alloy versus anneal conditions.

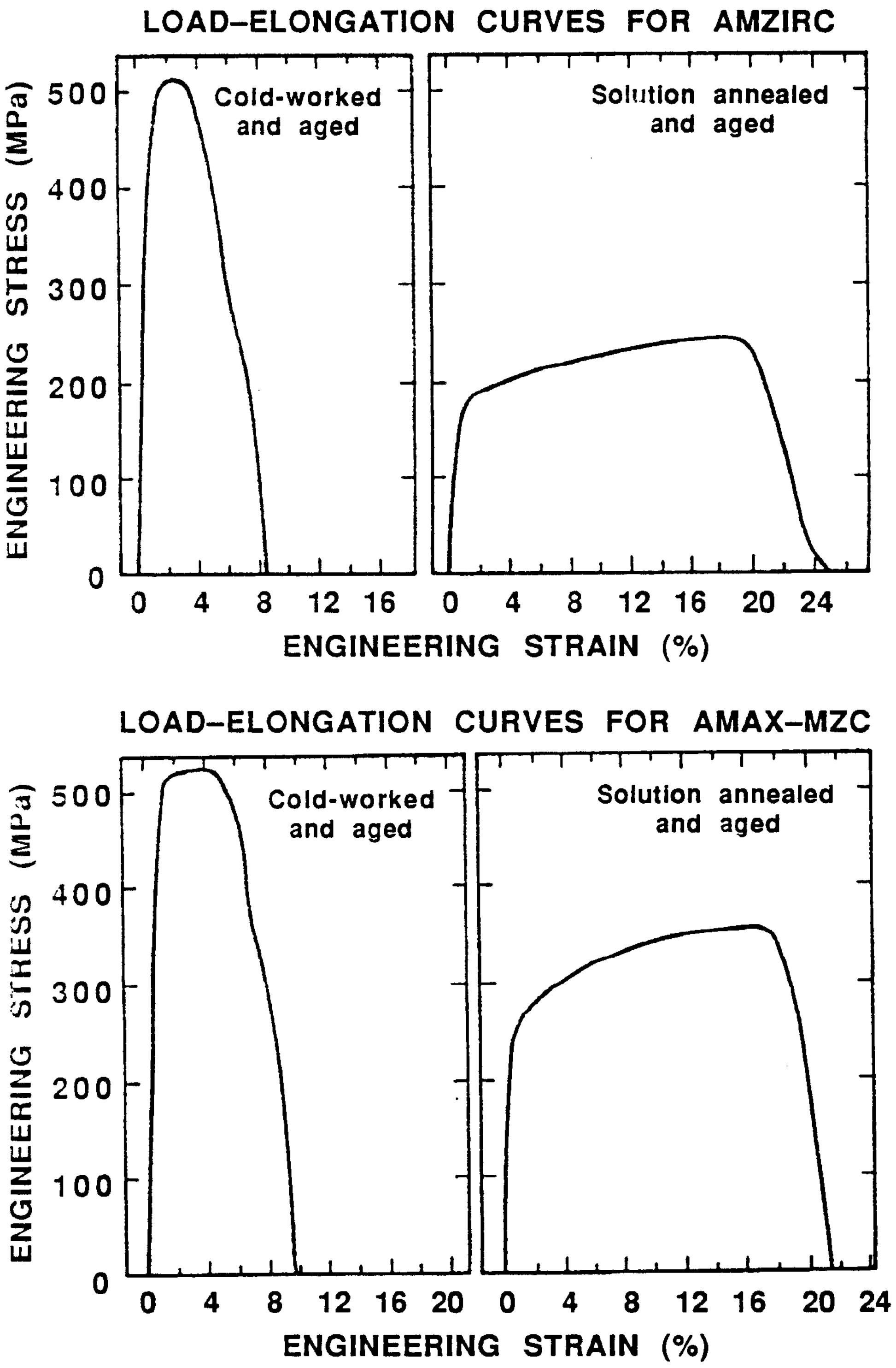

Fig. A.3. Load-elongation curves for the copper alloys.

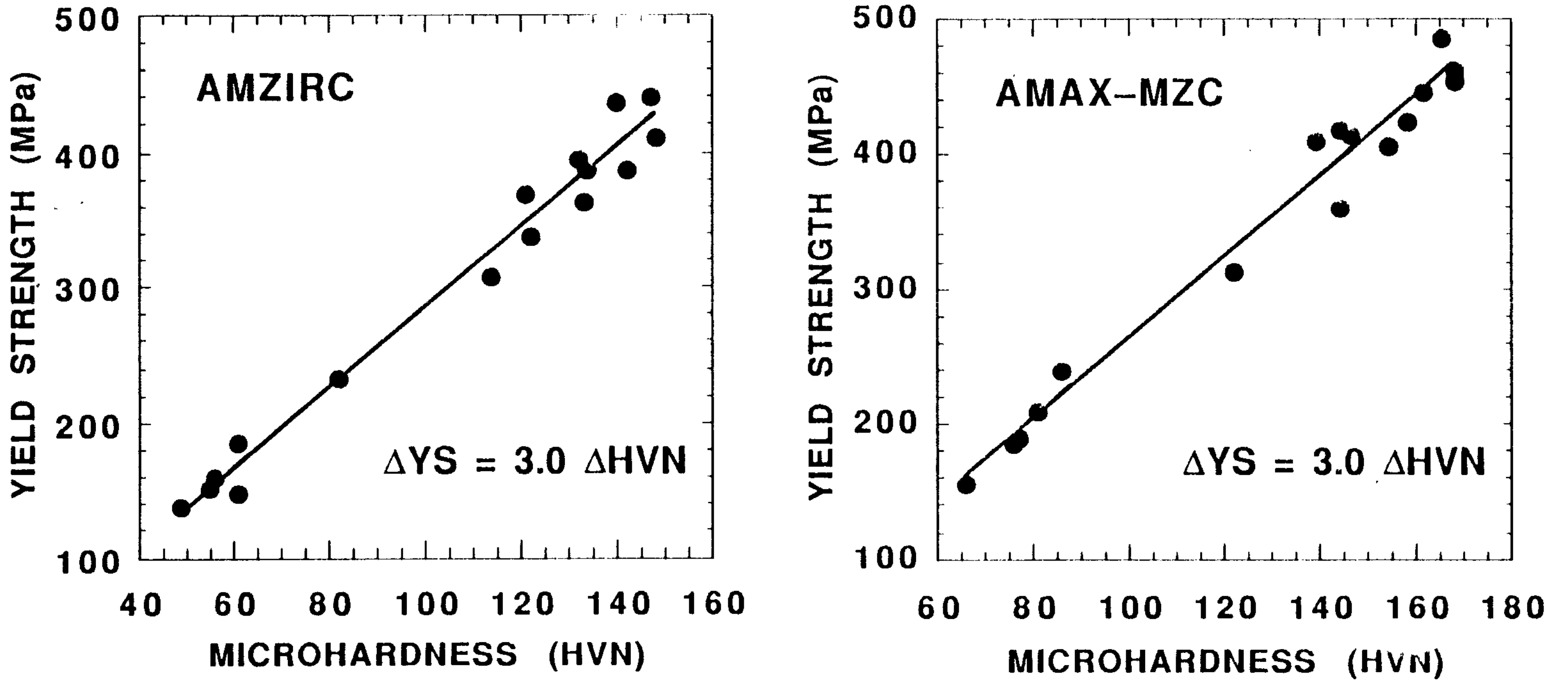

Fig. A.4. Correlation of the yield strength and Vicker's microhardness for the cold-worked and aged Amzirc and MZC.

Table A.4. Predicted Recyrstalliztion Temperature (T_R) of Amzirc and MZC

Anneal Time	1 Month	1 Year	10 Years
T_R	380°C	350°C	330°C

(for a given temperature) or temperatures (for a given time) can be extrapolated from short term annealing data. A single curve of all the data can be plotted using a Larson-Miller parameter, as is shown in Fig. A.5. Recrystallization occurs when the Larson-Miller parameter is ~15, and some extrapolated recrystallization temperatures for various times are shown in Table 5.4. Thus, from thermal annealing, the long term high-strength operating temperature is limited to ~300°C

B Monel K-500

Monel K-500 is an age hardenable Ni-Cu alloy with small amounts of aluminum and titanium added (Ni-30% Cu-2.7% Al-0.6% Ti). It is presently being considered for bearings in magnetic refrigerators because the alloy is non-magnetic[3]. However, the wear resistance of this alloy is not as good as other bearing materials (e.g. 5000 and 400 series steels) [3]. The presence of Al and Ti makes this alloy a prime candidate for nitrogen implantation.

Two thermal treatments of Monel K-500 were examined (solution-annealed and aged (SAA), and solution-annealed (SA)). Aging results in

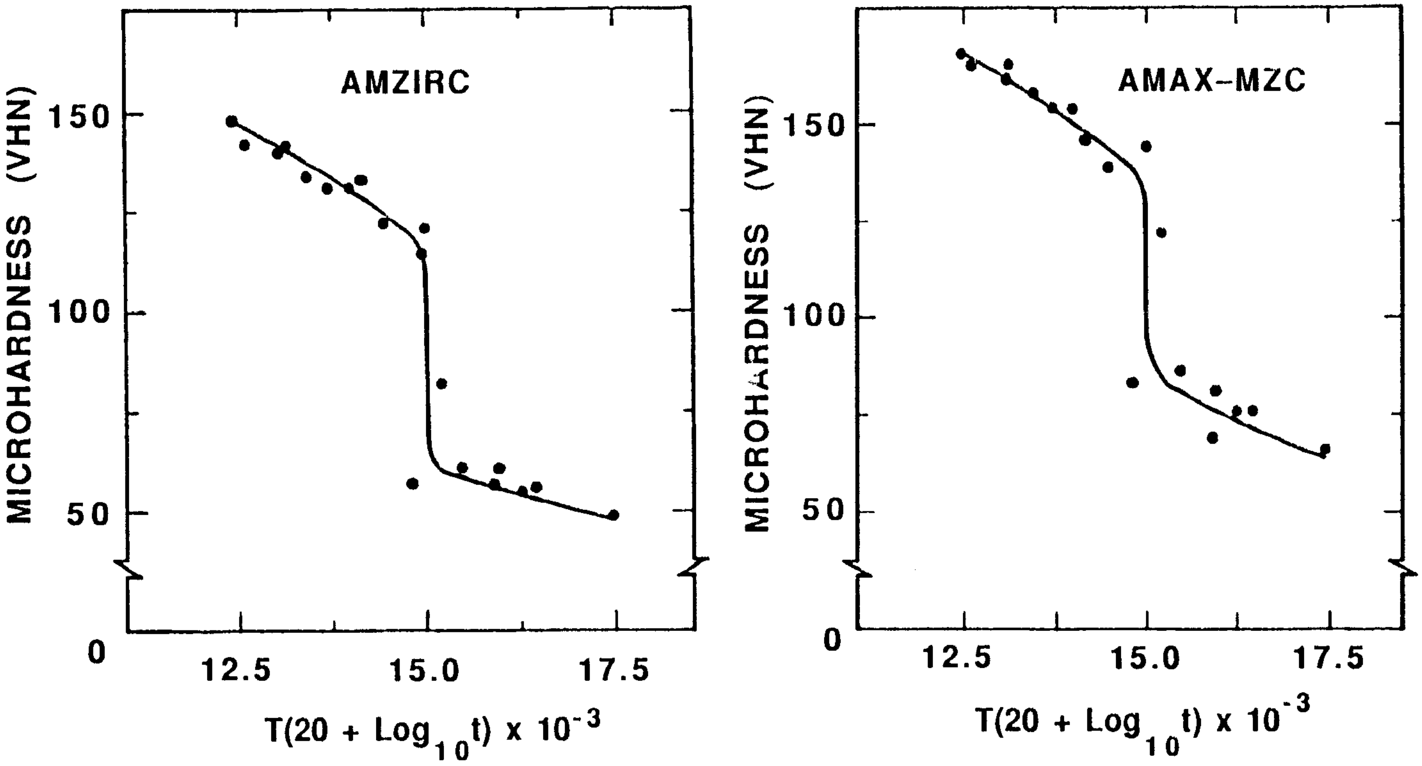

Fig. A.5. Vickers microhardness vsrsus Larson-Miller parameter for cold-worked and aged copper alloys following annealing for various times and temperatures.

the precipitation of gamma prime (a $Ni_3(Al,Ti)$ precipitate). Samples were mechanically polished to a 0.05 μm finish and then half of each sample was electropolished to remove the cold-worked layer. Half of each sample was masked off perpendicular to the electro/mechanical polish interface. Thus, each thermal treatment had four conditions to examine The samples were implanted using plasma source ion implantation (PSII) [3]. The samples were implanted with 50 keV N_2^+ ions to a fluence of 3×10^{17} atoms/cm^2. Sample temperature was assumed to be less than 100°C; however, questions as to the validity of that assumption have recently been raised [4].

Following implantation, Knoop and MPM microindentation tests, wear tests and TEM were done. Wear tests showedimprovement in the SAA Monel K-500's wear properties; however, no increase in Knoop hardness was seen [3]. TEM of the SAA alloy indicates dissolution of the gamma prime precipitates and the formation of strips or fringes characteristic of nitride formation. No stripes of fringes were seen in the SA alloy. Some decomposition of the Ni-Cu solid solution is suspected in both heat treatments following implantation [4]. More details of the Knoop and wear tests and TEM can be found elsewhere [3] (also see ref. 5 in Table 5.1).

Ultra-low load microindentations were made in the alloy, perpendicular to the implanted surface and in all four conditions. The indentations were made at 2-5 nm/s. Unloading data was taken 25, 50 and 400 nm. All hardnesses were normalized to the unimplanted, electropolished SAA alloy.

Hardness measurements on the SAA alloy indicated there was no difference between the electropolished and mechanically polished surfaces. Implantation resulted in a substantial increase in hardness in the implanted zone as is shown in Fig. A.6. Bulk hardness values for the SA alloy were lower than the SAA alloy, and the mechanically polished SA alloy was slightly harder than the electropolished SA alloy. Implantation of the SA alloy resulted in no hardness change over the unimplanted state. The SA alloy had a distinct rise in hardness near the surface to levels seen in the implanted SAA alloy. Figure A.7 shows the hardness of the SA alloy relative to the unimplanted, electropolished SAA alloy. The plastic hardness results from the unloading curves are shown in Table A.5. Modulus measurements show no differences between the various samples.

The SAA alloy's major strengthening mechanism is the gamma prime precipitates. Cold-working via mechanical polishing has a minor effect on further hardening of the alloy. The lack of precipitates in the SA alloy makes work hardening by mechanical polishing an important factor. Without precipitate Monel K-500 work hardens quite substantially. In this system the precipitates reduce the amount of work hardening the alloy can undergo. The near surface rise in the electropolished SA alloy could be the result of inadequate electropolishing. Alternatively, a dislocation free surface could produce a surface zone where the strength approaches the theoretical lattice strength, thus resulting in a near surface hardness increase [5].

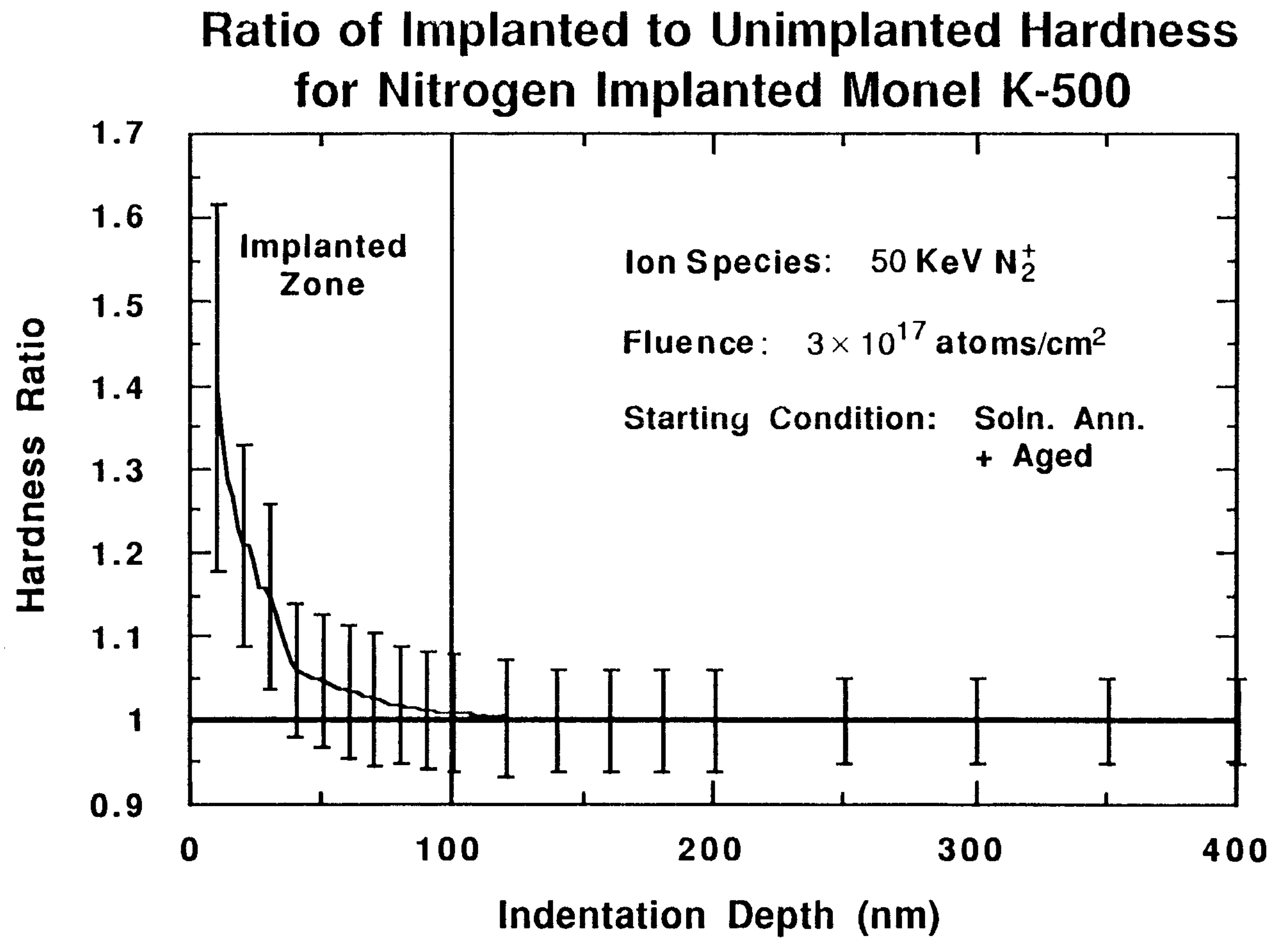

Ratio of Implanted to Unimplanted Hardness for Nitrogen Implanted Monel K-500

Fig. A.6. Ratio of Implanted to Unimplanted Hardness for As-Recieved Nitrogen implanted Monel K-500.

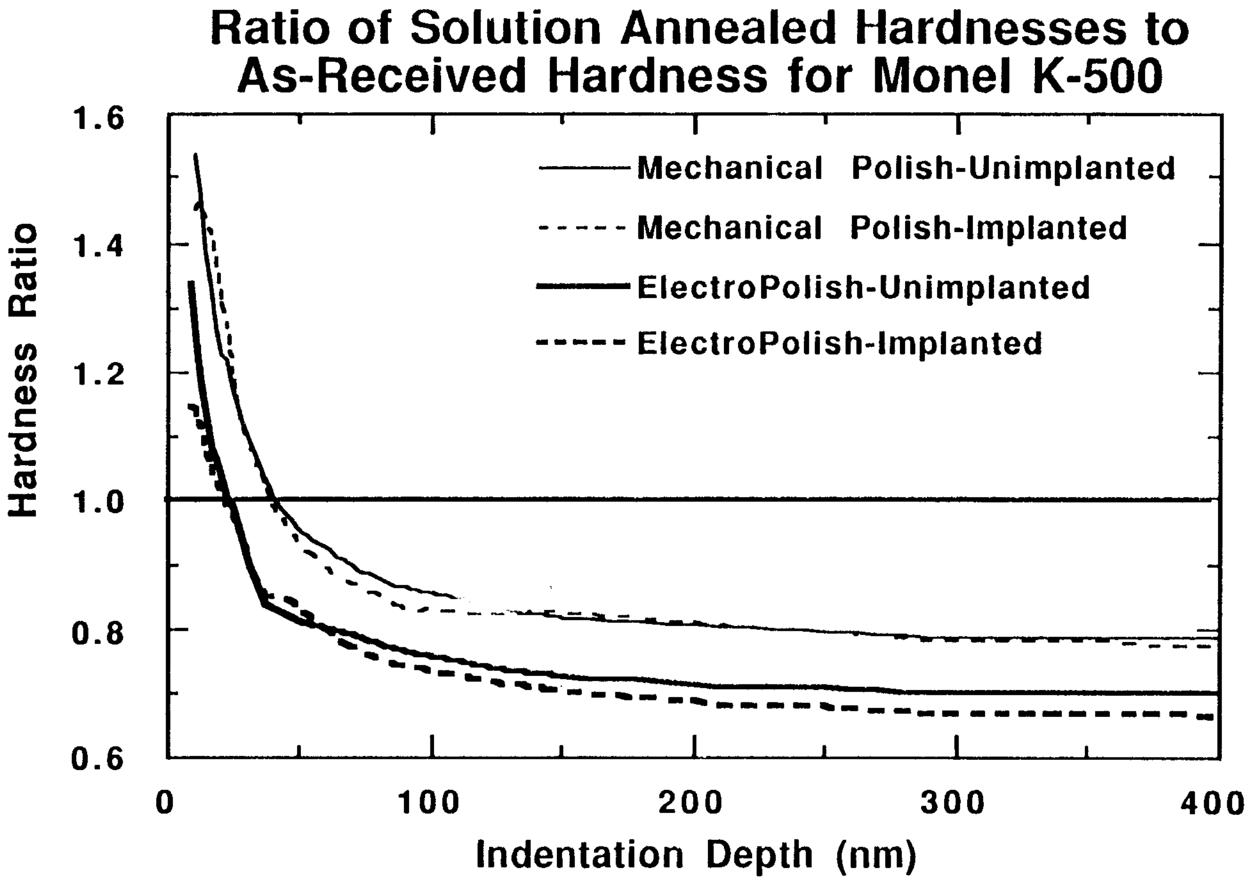

Fig. A.7. Ratio of Solution-Annealed Hardnesses to Solution-Annealed and Aged Hardness for Monel K-500.

Table A.5. Plastic Hardnesses Normalized to Solution-Annealed and Aged Monel K-500.

Alloy Condition	Indentation Depth (nm)		
	25	50	400
Solution-Annealed And Aged + Implanted	1.42±0.21	1.20±0.16	1.06±0.10
Solution-Annealed + Mechanical Polish	1.07±0.25	0.89±.11	0.74±0.05
Solution-Annealed + Mechanical Polish + Implanted	1.16±0.25	0.92±0.15	0.73±0.08
Solution-Annealed + Electro-Polish	0.85±0.20	0.75±.10	0.65±0.05
Solution-Annealed +Electro-Polish	0.80±0.19	0.72±0.12	0.63±0.06

The rise in implanted hardness of the SAA alloy is the result of the dissolution of the gamma prime and the formation of nitrides. For the SA alloy the lack of any hardness increase could be attributed to Al and Ti being sparsely scattered in solution (unlike the dense concentration around the dissolved gamma prime in the SAA alloy) and inability to diffuse enough to form nitrides. Unlike the Ni-Cu alloys used in this thesis, there does not appear to be any hardness increase resulting from the decomposition of the Ni-Cu solid solution. Inert gas implantation and/or higher temperature implants may be needed to separate nitriding effects from radiation-enhanced thermodynamics.

APPENDIX

REFERENCES

1. S.J. Zinkle, Ph.D. Thesis, Nuclear Engineering Department, University of Wisconsin-Madison (1985).
2. **Copper and Copper Alloys for Fusion Reactor Applications**, F.W. Wiffen and R.E. Gold (Eds.), DOE-OFE Workshop Proc., ORNL-830466 (1984).
3. M. Madapura, et.al., Surf. Coat. Tech. 39/40 (1989) 587.
4. R.A. Dodd, private communication (1990).
5. J. B. Pethica and W.C. Oliver, **MRS Symposium Proceedings**, Vol. 130, (1989) 13.